DEPARTMENT OF PHYSICS AND ASTRONOMY “E.MAJORANA”

UNIVERSITY OF CATANIA

Doctoral in Material Science and Nanotecnologies

(XXXIV Cycle)

Metalization on SiC surfaces:

Ohmic contacts of Ni on 4H-SiC by laser treatment

SILVIA CASTORINA

Ph.D Course Director

Prof. G.Compagnini

Tutors

Prof.ssa M.Grimaldi

Prof.ssa L.Calcagno

Acknowledgments

I express my deep gratitude to my tutors M.G. Grimaldi and L. Calcagno for their invaluable teaching, support and guidance, essential to complete my doctoral studies. I also thank Dr. G. Franco and Dr. M. Boscaglia for giving me the opportunity to spend almost six months, unfortunately interrupted by Covid-19, working with their group at 000STMicroelectronics in Catania. This experience has enriched me professionally and personally.

A heartfelt thanks to Anna Bassi and Paolo Badalà, with whom I shared this experience from the beginning.

I am particularly grateful to Dr. La Magna for his advices and availability during my work.

Special thanks also go to Prof. G. Compagnini, Prof. P. Musumeci, Prof. S. Mirabella and all the people of the CNR-IMM group.

The last, biggest thanks go to my parents and my husband, who most deserve it.

Contents

Acknowledgments……**III**
Introduction……..……....**VI**
Thesis Contents……...……**X**
References…….…….……..…**XI**

Chapter 1. Silicon Carbide: A New Material for Power Electronics.....1
1.1 Crystal structure and SiC polytypes.....2
1.2 Band structure and intrinsic carrier concentration.....6
1.3 Critical electric field.....10
1.4 Carrier mobility and thermal conductivity.....12
1.5 Doping of SiC.....14
1.6 SiC based devices and applications applications.....15
References.....18

Chapter 2. Metal-semiconductor contact.....22
2.1 Introduction.....22
2.2 Schottky and ohmic contacts.....23
2.3 Specific Contact Resistance.....28
2.4 Ohmic contact on n-type 4H-SiC by thermal annealing.....33
References.....38

Chapter 3. Ohmic contact on SiC by laser process.....42
3.1 Introduction.....42
3.2 Laser annealing and SiC: a brief review 42
3.3 Laser annealing and SiC: simulations.....52
References.....55

Chapter 4. Silicidation with pulsed-laser annealing method.....58
4.1 Experimental methods.....69
4.2 Results.....60
4.2.1 Compositional and structural characterization.....60
4.2.2 Electrical characterization: sheet resistance measurements.....92
4.2.3 Discussion.....94
References.....99

Conclusions.....100

Introduction

The recent developments of the entire field of solid state physics and the success of silicon-based electronics are the basis of many revolutionary changes in modern society. Integrated circuits, solar cells and sensors are some of the most common silicon-based technologies. Indeed, Si-based devices dominated power semiconductor industry for several decades, thanks to many years of development and well-established studies leading to high manufacturing capability with extremely low cost.

However, they have almost approached their performance limits and for some specific applications, i.e. high-frequency electronics, high-temperature operating system and flexible electronics, Si-devices show poor efficiency due to intrinsic material limitations. Therefore, a different strategy is needed to overcome this issue and the use of wide band gap semiconductors has been proposed to enhance the power devices performances.

Silicon carbide (SiC), in particular, is an emerging material with many promising aspects for power electronics applications. It is an indirect band semiconductor with high saturation drift velocity, capable of sustaining high electric fields, wide range doping for both p- and n-species and, moreover, it has silicon oxide SiO_2 as native oxide. Table 1 shows the relevant material properties of SiC, discussed in next chapter, compared with some other semiconductor materials such as Si and GaN and diamond.

Semiconductor	Si	SiC			GaN	Diamond
		3C	4H	6H		
Band gap [eV]	1.12	2.2	3.26	2.86	3.39	5.47
Thermal conductivity [W/cmK]	1.51	4.9	4.9	4.9	1.3	20.9
Mobility [cm^2/Vs] electron	1500	800	1000	460	900	1800
hole	450	70	120	10	400	1600
Breakdown electric field [MV/cm]	0.3	3.0	3.0	3.0	2.6	5.6
Relative permittivity	11.7	9.6	10	9.7	8.9	5.7
Saturation drift velocity [cm/s]	1×10^7	2.7×10^7	2.7×10^7	2.0×10^7	2.7×10^7	2.7×10^7

Table 1: Comparison of important semiconductor properties [1].

The potential of SiC-based devices for power electronics was first suggested in 1989 by Baliga [2] immediately followed by a large number of reports.

First applications were made in the fabrications of SiC diodes. Then SiC-based metal-oxides semiconductor field effect transistor (MOSFET) were developed and different SiC polytypes were studied for performance increase.

Ten years later, in 2000, SiC technology became available in the market. However, much work is still required to obtain further improvements in SiC devices large-scale production, both in terms of performance and cost reduction.

One of the most important issues in SiC technology is the fabrication of reliable low-resistance Ohmic contacts to SiC devices. Typically, rapid thermal annealing (RTA) exceeding 900 °C are used to achieve an Ohmic behavior.

However, nowdays the conventional thermal annealing is gradually substituted by laser annealing (LA) processes, carried out on the back-side of thinned wafers at the end of the fabrication flow, including the grinding process, see Fig.1

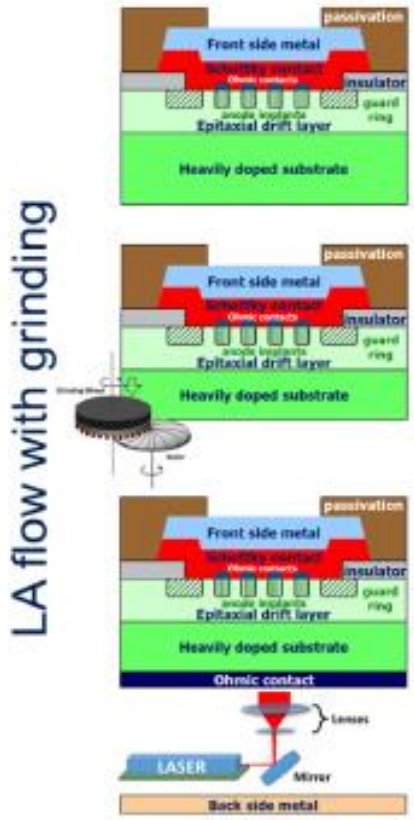

Fig.1 Schematic flow chart for the fabrication of JBS diode

To further clarify this aspect let us recall that the relevant parameter of the device, the total specific ON-resistance (R_{ON}), can be defined by:

$$R_{TOTAL}^{ON} = R_{Drift} + R_{Bulk} + R_{Ohmic}$$

where R_{Drift} is the drift specific resistance, R_{bulk} is the bulk specific resistance and R_{Ohmic} is the Ohmic contact specific resistance of the device (contact resistance per unit area, measured in Ωcm^2). Figure 1.4 shows the schematic structure of the Schottky Barrier Diode.

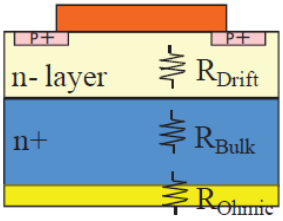

Fig.2: Schematic structure of the Schottky Barrier Diode

For example, in a 650 V SiC Schottky diode fabricated onto a 350 µm thick substrate, about 70% of the total RON is represented by the SiC substrate contribution, R_{Bulk} [3]. On the other hand, thinning the substrate to 110 µm allows reducing this resistive contribution down to 44% of the total R_{ON} (Fig. 3) [4]. This explains why for medium voltage applications (600–1200V), the wafer grinding step has become crucial in SiC technology to reduce the substrate thickness and minimize R_{ON}.

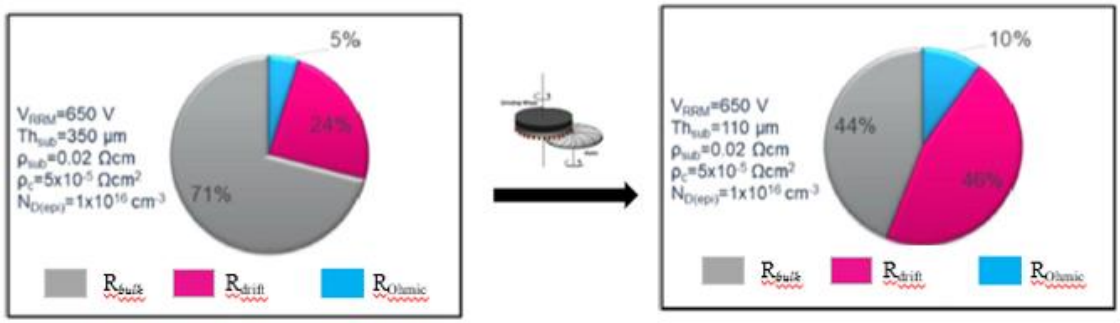

Fig.3: Resistive contributions (in terms of contact resistance, R_{Ohmic}, epitaxial-layer resistance, R_{drift}, and substrate resistance, R_{bulk}) of the total R_{ON} in a 650 V 4HSiC Schottky diode for two different substrate thickness of 350 µm (left) and 110 µm (right).
For this calculation, substrate resistivity of 0.02 Ωcm, specific contact resistance of backside contact of 5×10^{-5} Ωcm^2, epilayer doping of 1×10^{16} cm^{-3} have been used.

Therefore, thermal annealing is not realiable, due to the presence of defined devices on the front of the wafer and the material is fragile, then LA technique is mandatory to obtain the Ohminc contact formation on back-side of SiC, although a clear correlation with the morphological and structural modifications of the whole metal stack and of the metal/SiC interface is still under investigation.

The aim of this thesis is the analysis of different aspects concerning the Ohmic contact formation on SiC through laser treatment.

For this purpose, different analyses with various laser conditions (shot numbers, energy density) have been carried out to obtain and characterize the Ohmic contact structures after LA.

The present work contributes to clarify some of the previous phenomenological aspects, combining the Rutherford Backscattering Spectroscopy (RBS) with other well known techniques as X-ray diffraction, cross-sectional TEM, Energy-dispersive X-ray spectroscopy (EDX) and Sheet Resistance measurements.

Moreover, the experimental results are discussed by simulation codes [5] to understand the stoichiometry and the cristal phases of formed silicides due to LA process.

The whole work is the result of an extremely intense collaboration between the University of Catania, St-Microelectronics and CNR-IMM HQ.

Thesis Contents

The thesis illustrates, after a theoretical background, the experimental results and computer simulations performed to investigate ohmic contacts on 4H-SiC (n-type semiconductor) through laser treatments. It contains several chapters with the following outline:

Chapter 1 Briefly recalls the main physical properties of Silicon Carbide mostly suitable for the realization of power devices. After a short historical evolution of SiC devices, the crystal structures, the energy band gap, the intrinsic carrier concentration, the critical electric field, the thermal conductivity and the electron mobility are discussed. Furthermore, applications of SiC and some SiC based devices are shown.

Chapter 2 The basic concepts related to the Schottky barrier formation, the physics of Ohmic contacts and the contact resistance measurement techniques are reported. Then, some aspects concerning the formation of low Ohmic contacts resistance (10^{-5}-10^{-6} Ωcm^{-2}) on n-type SiC are discussed, focusing on Ni-based contacts and first considering thermal annealing.

Chapter 3 Is devoted to formation of ohmic contact through "non conventional annealing" as laser process, to the interaction between laser and Ni on SiC surface and theoretical methods, with numerical simulations, to evaluate silicides phase formation after laser irradiation.

Chapter 4 Contains the Experimental results for Ohmic contact formation in Ni on SiC surface samples obtained under different LA conditions and the relative characterization by RBS, X-ray diffraction, cross-sectional TEM, EDX and numerical simulations.

References

[1] Wijemuni Milantha De Silva, Low Resistance Ohmic Contact Formation. (2016)

[2] B.J. Baliga. Power semiconductor device figure of merit for high frequency applications. Electron. Device Lett., 10, 455, 1989.

[3] S. Rascunà, P. Badalà, C. Tringali, C. Bongiorno, E. Smecca, A. Alberti, S. Di Franco, F. Giannazzo, G. Greco, F. Roccaforte, M. Saggio. "Morphological and electrical properties of Nickel based Ohmic contacts formed by laser annealing process on n-type 4H-SiC"

[4] F. Roccaforte, G. Brezeanu, P.M. Gammon, F. Giannazzo, S. Rascunà, M. Saggio. Schottky contacts to silicon carbide: physics, technology and applications, in Advancing Silicon Carbide Electronics Technology vol I, Mater. Res. Found. 37 (2018) 127–190.

[5] S. F Lombardo, G. Fisicaro, L. Deretzis, A. La Magna, B. Curver, B. Laspinasse, K. Huet.Theoretical study of the laser annealing process in FinFET structure.App. Surf. Sci 467-468 (2019)666-672.

Chapter 1

Silicon Carbide: A New Material for Power Electronics

SiC is a wide band gap semiconductor material that has experienced rapid development in recent years and it is slowly replacing Silicon devices in many power electronic applications. Research on Silicon Carbide started already before 1960s, even though difficulties in fabricating high-quality crystals and the increasing success of Silicon technology put SiC studies apart [1]. Subsequent technology improvements and new fabrication techniques [2-3], which allowed the fabrication of higher quality SiC wafers, renewed the interest in this material, especially its applicability in the power electronics area.

First SiC high voltage devices were Schottky barrier diodes [4-6] or PiN diodes [7-8], vertical JFETs [9-11] and high voltage MOSFETs [12-16]. The main problem associated with power MOSFETs in Silicon Carbide was the very poor quality of the oxide/semiconductor interface, which turned in low channel mobility and device reliability issues [17-18]. Initially, the diffusion and the development of those devices were hindered by the quality of the material and the size of defect-free areas on SiC wafers [19].

In fact, following the market evolution of past years (Figure 1.1), almost a decade passed between the first commercial SiC power device in 2001, which was a Schottky diode, and the first affordable mass produced Power MOSFET in Silicon Carbide in 2011 [20].

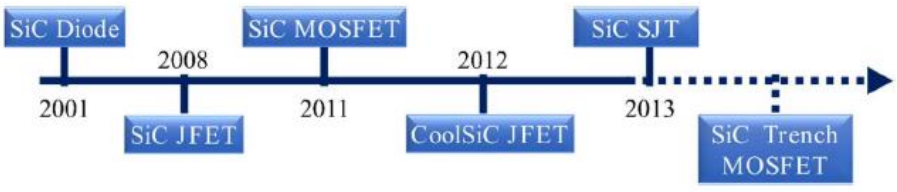

Figure 1.1: Milestones of commercialization of SiC power devices

In the next paragraphs the most relevant advantages arising from the use of SiC semiconductor due to its inherent physical properties, such as wide band gap, high critical electric field, high thermal conductivity, electron mobility, doping and SiC based devices will be analyzed.

1.1 Crystal structure and SiC polytypes

The SiC crystal appears as a semi-transparent, yellow-green crystal. Silicon Carbide is a IV−IV compound semiconductor, meaning that both its constituents Si and C have four valence electrons. They bond into a tetrahedral structure in which each Si ion is surrounded by four C ions, and viceversa. The nature of the bond is nearly purely covalent (88% covalent and 12% ionic according to Pauling's definition) and the strong chemical bonding between Si and C atoms, with a bond energy of 4.6 eV, gives to the material unique properties such as very high hardness, chemical inertness and high thermal conductivity. The geometry and high binding energy of the crystal give it many properties: SiC has an excellent high hardness of 9 points on the Mohs scale, between topaz and diamond, wear resistance and good thermal stability up to the extremely high melting point of 3100 K. [21].

Silicon Carbide crystals are protected against oxidation by a thin (few Å) surface SiO_2 layer. Thermal oxidation was conducted in dry oxygen ambient at temperature above 1000 °C. Though the Si-C bond is covalent, the different electronegativity of the ions causes the valence electrons to be slightly nearer to C ions than to Si ions.

From a crystallographic point of view, the variation in the silicon and carbon occupied sites along the c-axis in a hexagonal close-packed system brings about different crystal structures, called polytypes and for Silicon carbide, over 200 stable polytypes are known [22].

From a crystallographic point of view, the variation in the silicon and carbon occupied sites along the c-axis in a hexagonal close-packed system brings about different crystal

structures, called polytypes and for Silicon carbide, over 200 stable polytypes are known [22].

Though every polytype consists of exactly the same layers along the $\boldsymbol{a_1}, \boldsymbol{a_3}, \boldsymbol{a_3}$ axes, each is different along the **c** axis. Indeed, the elementary SiC tetrahedra, as shown in Fig. 1.2 (a), are adjoined into a hexagonal network. The three base Si atoms (denoted as empty circles) and the central C atom (denoted as full circles) form the first SiC plane, as shown in Fig. 1.2(b), while the fourth Si atom (empty squares) follows on top of the C atom, forming the second hexagonal Si network. However, the positioning of the second C layer (full squares) can follow two routes, as shown in 1.2(c) and 1.2(d): respectively, they can either be placed on top of the first Si network, or they can be shifted to the centre of the triangles formed by the second C network. Then the third Si layer (empty triangles) is stacked directly on top of the C atoms, and so on. It may be noticed that a Hexagonal Closed Packed (HCP) lattice is formed if every second Si layer is placed on top of the previous one, while a face centered cubic (FCC) lattice is formed if it is shifted [22].

As shown in Fig.1.2 (e), a notation can be introduced for the stacking sequence known as the ABC notation, as originally suggested by Page [23]. In the AB notation we start by denoting a first layer by the letter A, and the two following stacking dispositions are then denoted B and C. The cubic disposition is referred to as (...ABCABC...) while the hexagonal disposition as (...ABAB...). However, the two stacking dispositions can be intermixed to form more complex and longer periods. This is easier to notice along the {1120} plane, as in Fig.1.3, where we see the most common SiC polytypes with their stacking sequences.

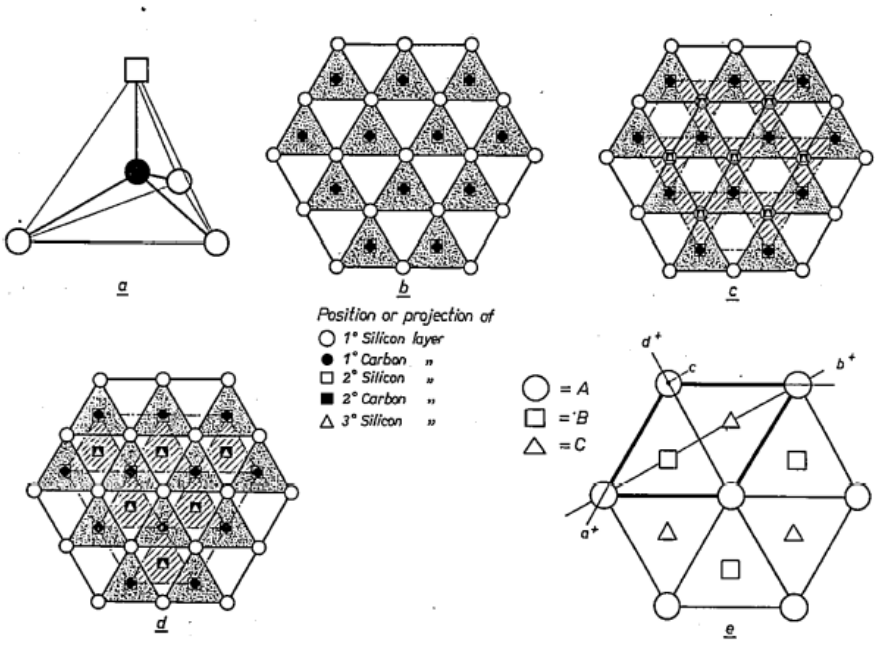

Figure 1.2: Positions of Si and C atoms in SiC: (a) Elementary SiC tetrahedron; (b) Projection of the first tetrahedral layer; (c) Projection of the first and second layer, in cubic disposition; (d) Projection of the first and second layer, in hexagonal disposition; (e) Projection of the first and second layer in the alternative dispositions A, B and C [31].

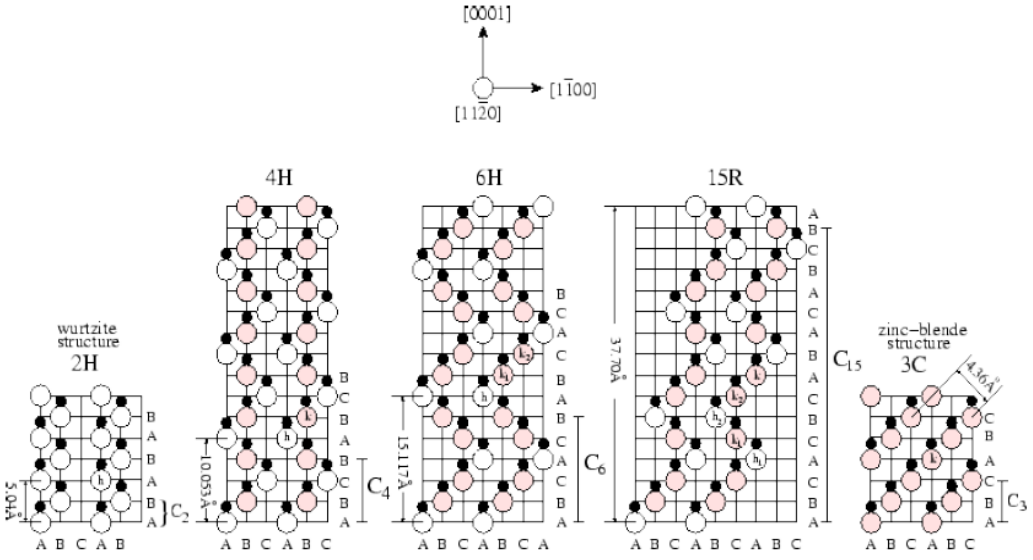

Figure 1.3: Stacking sequences of 2H, 4H, 6H, 15R and 3C-SiC, respectively, in Ramsdell's notation

Other nomenclatures were introduced by Jagodzinski [24], in which the stacking sequences are defined by the local layer cubic (k) or hexagonal (h) environments, by Ramsdell [25], that consists of the number of layers forming the period and the kind of resulting lattice (C cubic, H hexagonal or R rombohedral), and finally by Zhdanov [26], which specifies the number of consecutive cubic layers. Table 1.1 shows how these notations can be used to represent the most common SiC polytypes. Stability of the various polytypes is strongly affected by temperature. As an example, 3C-SiC spontaneously rearranges as 4H-SiC or 6H-SiC at temperatures higher than 1900 °C [27]. 2H-SiC also results instable at high temperatures, so that the 4H and 6H polytypes are mostly studied for applications. SiC polytypes also show remarkably different lattice structure and constants.

As an example, though the Si-C bond length and SiC bilayer height remain fixed at 1.89 Å and 2.52 Å, the lattice constants vary: a = 4.3596, 3.0798, 3.0805 for 2H, 4H and 6H respectively, while c is 10.0820 for 4H and 15.1151 for 6H.

Page	*Jagodzinski*	*Ramsdell*	*Zhdanov*
AB	h	2H	11
ABC	k	3C	∞
ABCB	hk	4H	22
ABCACB	hkk	6H	33
ABCACBCABACABCB	hkkhk	15R	$(32)_3$

Table 1.1: Stacking sequence notations for the principal SiC polytypes

1.2 Band structure and intrinsic carrier concentration

The band structure of a crystalline solid is the relationship between electron momentums **k** and the associated energies **E**. It is a fundamental concept to understand how the electrons interact with photons and phonos, and with each other; group velocity, effective masses and other important properties also depend on the concept of band structure [28]. The band structure is usually obtained by solving the steady-state Schrodinger equation for a one-electron wave function ψ(r,k) in the periodic potential V (r) of the Bravais lattice:

$$\left(-\frac{\hbar^2}{2m}\Delta^2 + V(\boldsymbol{r})\right)\psi(\boldsymbol{r},\boldsymbol{k}) = E(\boldsymbol{k})\,\psi(\boldsymbol{r},\boldsymbol{k}) \qquad (1.1)$$

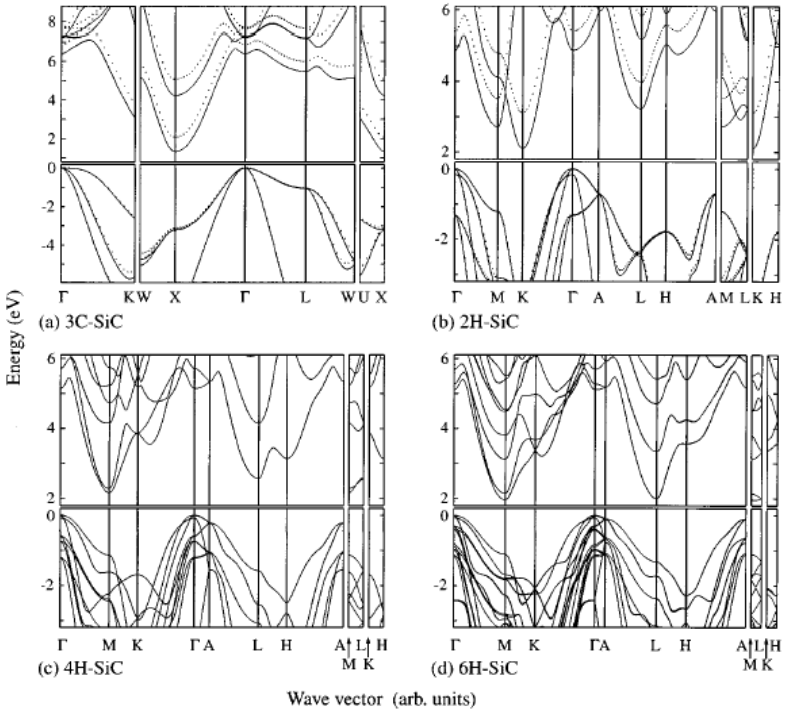

Figure 1.4: Band structures of 3C, 2H, 4H and 6H SiC, obtained by means of relativistic density function theory (DFT) [29].

A number of approximations and numeric calculation methods are then employed -e.g. to account for the presence of other electrons, both free and bonded, such as the tight binding method [30], the density functional theory (DFT) [31], and the **k·p** method [32].

As it can be demonstrated by means of the Bloch theorem [33], the resulting band structure E(k) is periodic in the reciprocal lattice. As such, it can be fully described by its values in the primitive cell of the reciprocal lattice, the first Brillouin zone. For semiconductors and insulators, the band structure leads to the concept of energy gap, which is a range of energy values that electrons cannot access, whatever their momentum; the upper band is named conduction band, while the lower valence band.

Quantitatively, we define energy gap -or band gap- the difference between the conduction band absolute minimum and the valence band absolute maximum, $E_g = E_c - E_v$.

It should be noted that there is no guarantee that the E_C and E_V values occur for the same **k**.

When this happens, electrons are free to pass from the two bands by only means of energy exchange E_g, and the band gap is called direct; if not, the corresponding Δk must be exchanged as ell in order for the electron to move from band to band, and the gap is called indirect. Then, we recall the fundamental concept of effective mass, defined as the inertial mass value of the electron moving inside the periodic potential. Since the potential changes according to the dispersion relation along the reciprocal lattice directions, the effective mass is both a tensor and a function of the momentum, defined as:

$$\frac{1}{m_{ij}^*} = \frac{1}{\hbar^2}\frac{\partial^2 E(k)}{\partial k_i \partial k_j} \tag{1.2}$$

The band structures of various SiC polytypes are different from each other, as a consequence of the stacking sequence and primitive cell, as shown in Fig. 1.5 [28]. It should be noted that though the band slopes are experimentally confirmed, band gap values obtained by DFT calculations are interested by a sistematic error of about 40% to 60%. Precise values of the bandgap are reported in Table.1.2. The electron effective masses also differs, as shown in 1.2, while no significant variation is found for hole effective masses, which are $m\perp = 0.66$ and $m\parallel = 1.75$ for 4H-SiC.

Polytype	*Electron effective mass*	*Bandgap*
2H-SiC		3.30
$m_{\perp}$	0.23	
$m_{\parallel}$	0.68	
3C-SiC		2.36
$m_{\perp}$	0.43	
$m_{\parallel}$	0.26	
4H-SiC		3.26
m_{ML}	0.31	
$m_{M\Gamma}$	0.57	
m_{MK}	0.28	
6H-SiC		3.02
m_{ML}	1.83	
$m_{M\Gamma}$	0.75	
m_{MK}	0.24	

Table 1.2: Electron effective masses for 3C, 2H, 4H and 6H SiC, obtained by DFT [28], and the corresponding band gaps.

Finally, the intrinsic carrier concentration can be calculated in function of temperature T and energy band gap E_g as:

$$n_i = \sqrt{NcNv}\, e^{\frac{-Eg}{2KT}} \tag{1.3}$$

with $N_{c,v}$ conduction and valence bands density of states and k Boltzmann's constant. The (1.3) can be written for Silicon and SiC as:

$$n_{i\_Si} = 3.87 \cdot 10^{16} T^{3/2} e^{-7.02 \cdot 10^3 / T}$$

$$n_{i\_SiC} = 1.7 \cdot 10^{16} T^{3/2} e^{-2.08 \cdot 10^4 / T}$$

At room temperature T_0=300 K the intrinsic carrier concentrations for Si and 4H-SiC are respectively $1.4 \cdot 10^{10} cm^{-3}$ and $6.7 \cdot 10^{-11} cm^{-3}$.

The intrinsic carrier concentration as a function of temperature for Si and SiC is plotted in Figure 1.5.

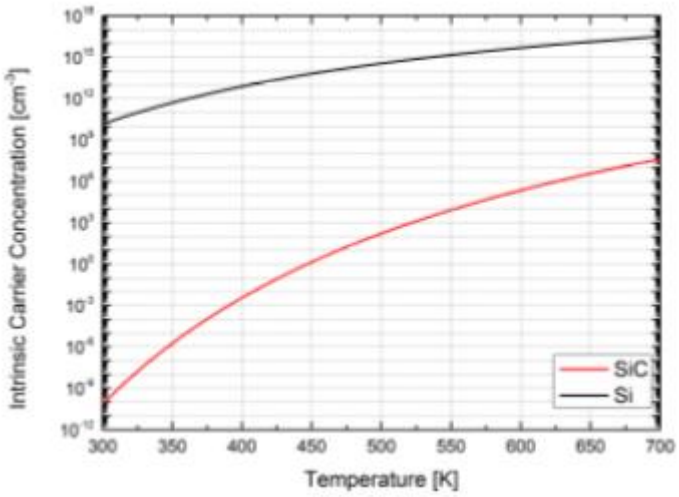

Fig. 1.5: Intrinsic carrier concentration as a function of temperature for Si and SiC

The leakage current of a device is dependent from the intrinsic concentration, and obviously it should be minimized for reliable and efficient devices operation. Silicon operating temperature is usually limited at about 150 °C before intrinsic concentration becomes comparable to typical doping concentration of 10^{14} cm^{-3}, while SiC devices do not suffer this issue for temperature even above 500 °C. Obviously, in this case, device operating temperature is limited by other factor such as packaging, contact/bond wires metal, etc.

1.3 Critical electric field

One of the most celebrated feature of Silicon Carbide is its elevated critical electric field E_{cr}. It corresponds to the electric field for which impact ionization takes place. This property is due to higher impact ionization coefficient compared to other materials, direct consequence of the wide band gap energy. If Silicon has a critical electric field of about $3 \cdot 10^5$ V/cm, in Silicon Carbide it is approximately one order of magnitude higher, 2-3$\cdot 10^6$ V/cm. E_{cr} is a function of the semiconductor doping concentration, and different analytical formulas were proposed to model its behaviour. A simple power law was suggested in [34]:

$$E_{cr} = 3.3 \cdot 10^4 N_D^{1/8} \tag{1.4}$$

According to [35] it could be also expressed as:

$$E_{cr} = \frac{2.49 \cdot 10^6}{1 - 0.25 log_{10}\,(N_D / 10^{16})} \tag{1.5}$$

The critical electric field for SiC can be compared in Figure 1.6 with that of Silicon (calculated according to [36]). As it is clearly visible in the case of Silicon Carbide E_{cr} is much larger. This feature results in a thinner and higher doped drift layer compared to that of Silicon devices for the same breakdown voltage. In fact, the relations between E_{cr}, V_{BR} and W_D are:

$$V_{BR} = \frac{1}{2} \frac{E_{cr}^2 \varepsilon_S}{q N_D} \tag{1.6}$$

$$W_D = \frac{2V_{BR}}{E_{cr}} \tag{1.7}$$

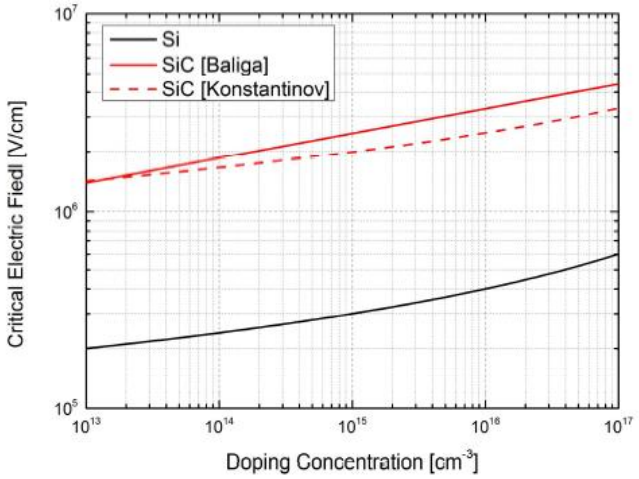

Figure 1.6: Critical electric field as a function of doping concentration.

Thus, given a desired V_{BR}, the doping concentration N_D can be increased and the thickness W_D can be reduced respect to equivalent Si device. The major upside of having a thin, high-doped layer is to reduce the specific ON-resistance $R_{ON,sp}$ of drift region. The same result can be inferred relating directly $R_{ON,sp}$ to the critical electric field:

$$R_{ON,sp} = \frac{4V_{BR}^2}{\varepsilon_s \mu_n E_{cr}^3} \tag{1.8}$$

Since this parameter defines how much resistive loss a device generates while operating in conduction, it can easily be understood the great advantage in using wide band gap semiconductors.

1.4 Carrier mobility and thermal conductivity

An important parameter in semiconductor materials is the carrier mobility depending on carrier concentration and temperature.

Electron mobility for SiC is usually lower than Silicon, and it strongly depends on material characteristics such as doping and direction of epitaxially grown crystals [37]. Moreover, for metal-oxide-semiconductor structure mobility is extremely dependent on interface quality, being affected by defects and traps density [38].

Specifically, the carrier mobility depends on carrier concentration and temperature (see Fig 1.7 that shows a) the electron and b) hole mobility as a function of donor density and acceptor density, respectively, at room temperature in 4H and 6H- SiC. The electron mobility of 4H-SiC is almost double that of 6H-SiC at a given dopant density, and 4H-SiC exhibits a slightly higher hole mobility than 6H-SiC. In particular, the maximum electron and hole mobility in 4H- SiC are about 1200 $cm^2V^{-1}s^{-1}$ and 120 $cm^2V^{-1}s^{-1}$, respectively. The higher 4H-SiC carrier mobility makes this polytype the most attractive for electronic power devices application [23].

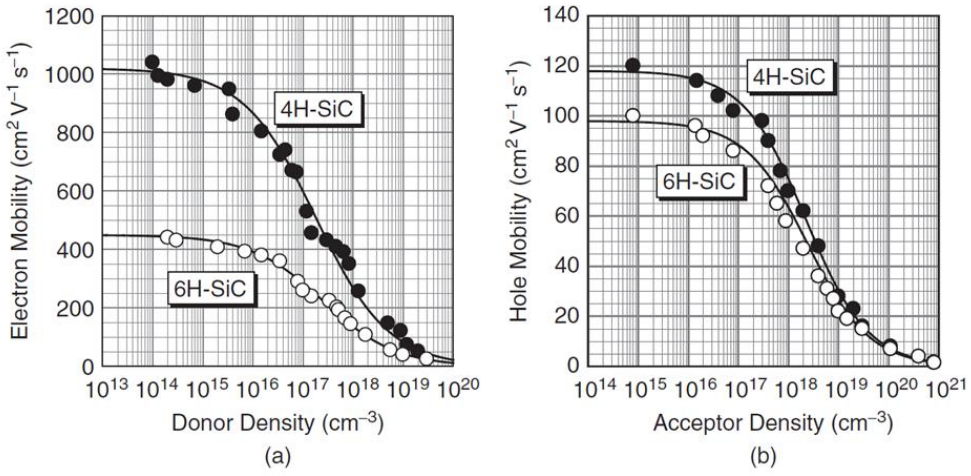

Fig.1.7: (a) electron and (b) hole mobility as a function of donor density and acceptor density, respectively, for 4H-SiC and 6H-SiC at room temperature [23].

However, at low doping concentration, the 4H-SiC electron mobility μ_n and hole mobility μ_p are smaller than the carrier mobility in silicon (see Fig.1.8). In both cases, the carrier mobility decreases with increasing doping concentration due to enhanced Coulomb scattering of free electron and hole by the ionized donors and acceptors [34].

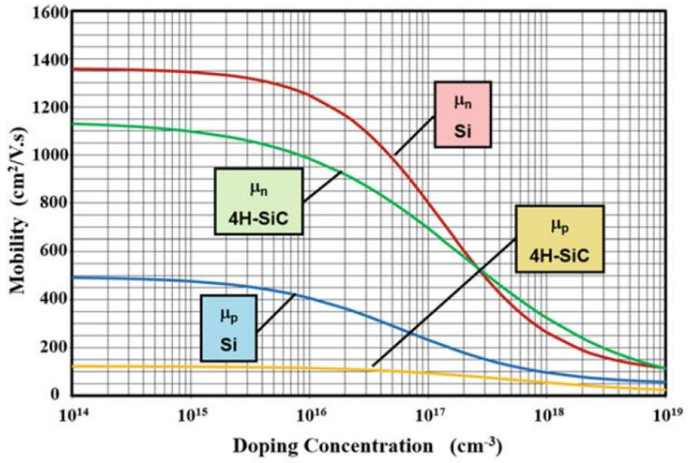

Fig.1.8: Comparison between electron and hole mobility for SiC and Si.

Silicon Carbide features a thermal conductivity λ about three times higher compared to Silicon, with its value approximately equal to 3.7 W/cmK. The high thermal conductivity allows a better diffusion of heat generated inside the material. Consequently, it could be possible to increase the device operating power level or to simplify cooling strategies (heatsink, fans, etc.) reducing system cost and volume.

SiC also exhibits a saturation velocity v_{sat} almost twice as high as Silicon, approximately of $2 \cdot 10^7$ cm/s. Some values of the main SiC properties are listed in Table 1.3.

Properties	Si	4H-SiC
$E_G\ [eV]$	1.12	3.26
ε_r	11.7	9.7
$\lambda\ [W/cmK]$	1.5	3-5
$E_{cr}\ [V/cm]$	$3 \cdot 10^5$	$2\text{-}3 \cdot 10^6$
$v_{sat}\ [cm/s]$	10^7	$2 \cdot 10^7$

Table 1.3: Main values of Si and 4H-SiC material properties.

1.5 Doping of SiC

Silicon carbide selective doping is performed by ion implantation and diffusion. Due to good control over doping concentration and low temperature needed during process, ion implantation is widely used instead of diffusion which requires very high temperatures due to the low value of diffusion coefficient of many dopants. Selective doping of SiC can be done through ion implantation by masking areas over the wafer surface which need not be doped. The masking can be done by deposition of high mass metals such as gold or an oxide layer. The mask thickness must be carefully chosen, keeping in mind the range of ions to be implanted so that they should not reach the underlying areas. For implantation the ions are accelerated at energies ranging from 1 KeV to 1 MeV for achieving implant depths from 50 nm to 1 μm. Implanted ions occupy interstitial lattice positions in SiC together with Si and C atoms which are displaced from their respective lattice position due to ion implantation. Ion implantation does not change
the electrical properties of SiC though; crystal structure may change depending on the doping level. For re-crystallization of material and activation of implanted ions the annealing is required [39,40], indeed the atoms become active after occupying lattice sites. The annealing temperature can be as high as 2000 °C at atmospheric pressure in the presence of inert argon gas.

The SiC electrical activation as a function of the annealing temperature at fixed implantation dose shows same features that can be described by general growth laws, applied in many different scientific sectors [41].

High temperature used for post-implantation annealing can be harmful for the mask therefore; sometimes it’s useful to perform ion implantation in hot environment with temperature ranging from 500 °C to 1000 °C. Hot implantation induces a dynamic annealing of ion irradiation defects resulting in a low amount of residual defects. Generally, both techniques, hot implantation followed by high temperature annealing, are combined to achieve crystal recovery and damage reduction togheter witn activation of implanted dopant [39, 40, 41].

1.6 SiC Based Devices and applications

Electronic devices based on SiC are suitable for high power and high frequency operations and due to better performance in power conversion and high switching speeds find applications in military, avionics, modern hybrid automobile power systems, uninterruptible power supplies, microwave and so on. Moreover some properties of SiC as the wide band gap and its radiation hardness make this material attractive for alternative application fields, such as UV photo-sensors, and charged particle and X-ray detectors. Some of the main applications are discussed below.

SiC Devices As Gas Sensors

Schottky barrier diodes (SBD) and FETs based on SiC can detect some important gases such as oxygen, hydrogen, carbon monoxide and hydrocarbons. When thin metal film of SiC Schottky contact is exposed to gases e.g. hydrogen the current-voltage characteristics of the SBD are affected within a few milliseconds of the exposure. This occurs due to the fact that the Schottky barrier height of the SBD changes when the device comes in contact with some of the gases to which the SiC SBDs are sensitive. SiC gas sensors find applications in automobiles and aircrafts for detecting the fuel leakage and for detecting fires [42].

SiC detectors

Silicon carbide (SiC) is already considered as a possible alternative to silicon for photons and particles detection. Silicon carbide Schottky barrier diodes (SBD) are able to detect ultra-violet radiation (UV) in a better way than Si based UV detectors because of SiCs wide bandgap. Because of wide bandgap SiC based SBDs are insensitive to radiation with frequencies below UV and can detect exclusively ultraviolet light even in the presence of visible and infrared light [43].

Silicon based sensors however, are sensitive to visible and infrared light too and show poor performance in their presence unless additional radiation filtering is provided.

Over the last years, considerable effort has been concentrated on better understanding the performance of SiC- based radiation detectors to be used in high temperatures and high radiation conditions under which conventional semiconductors detectors cannot be adequately used. SiC detectors were used with good results for neutrons [44], for x-rays [45] and for charged particles emitted by alpha sources [46]. The possibility to use X-ray SiC detectors operating at room or high temperature is of large interest as an alternative to conventional detectors that must operate at cryogenic temperatures [45]. Moreover, SiC detectors have been used to monitor the ionizing radiation emitted from high intensity laser- generated plasma [47, 48], permitting prompt measurements of X-rays and ions emitted during the short life of pulsed plasma. In particular, Torrisi et al. [49,50] has proved that SiC detectors, with an interdigit Ni_2Si front electrode, were able to detect ultraviolet radiation, soft X-rays, and low energy ions generated by a low intensity laser. In such applications these detectors showed high efficiency and very short rise time, due to their particular design that leaves a fraction of the active region directly exposed to the impinging radiation [51].

Power Conversion

Major applications of SiC based electronic devices can be found in power conversion from DC-DC or from DC-AC. For switched mode DC-DC conversion, Schottky diodes are combined with inductors capacitors in a circuit to either step up the input power or to step it down. Inductor transfers its stored energy through Schottky diodes during power conversion. DC-DC conversion finds widespread applications in industrial and consumer electronics. DC-AC conversion, on the other hand, uses multiple diodes coupled with inductors which transfer their stored energy through these diodes. DC-AC power conversion finds applications mostly in uninterruptible power supplies and motor speed control [52].

Microwave Applications

Superior material properties of silicon carbide are also exploited for microwave applications. Due to better RF and dc performance SiC based electronic devices are

preferred over devices based on conventional semiconductors such as silicon or gallium-arsenide. Devices based on SiC exhibit much better microwave power at room temperature than their Si and GaAs counterparts [53]. Use of 4H-SiC in microwave technology can result in low cost, high power and smaller sized devices with greater bandwidth control. For these reasons SiC MESFETs are being designed for continuous wave applications through X band and SiC static induction transistors (SIT), for high power pulsed transmitter technology, through L band operation.

References

[1] Matsunami H., “Current SiC technology for power electronic devices beyond Si”, Microelectronics Engineering, vol. 83, issue 1, p. 2-4, 2006

[2] Tayrov Yu.M., Tsvetkov V.F., “Investigation of growth processes of Ingots of silicon carbide single crystals”, Journal of Crystal Growth, vol.43, issue 2, p. 209-212, 1978

[3] Kuroda N., Shibahara K., Yoo W.S., Nishino S., Matsunami H. “Step controlled VPE growth of SiC single crystals at low temperatures” Extended Abstracts, 19th Conference on Solid State Devices and Materials, p. 227,1987.

[4] Bhatnagar M., McLarty P.K., Baliga B.J., "Silicon-carbide highvoltage (400 V) Schottky barrier diodes", in IEEE Electron Device Letters, vol.13, no.10, p. 501- 503, 1992.

[5] Kimoto T., Urushidani T., Kobayashi S., Matsunami H., "Highvoltage (>1 kV) SiC Schottky barrier diodes with low On resistances", in IEEE Electron Device Letters, vol. 14, no. 12, pp. 548-550, 1993.

[6] McGlothlin H.M., Morisette D.T., Cooper J.A., Melloch M.R., "4 kV Silicon carbide Schottky diodes for high-frequency switching applications", Device Research Conference Digest, 1999 57th Annual, p. 42-43, 1999.

[7] Neudeck P.G., Larkin D.J., Powell J.A., Matus L.G., "High voltage 6H-SiC rectifiers: prospects and progress", Device Research Conference, 1993. 51st Annual, p. 116-117, 1993.

[8] Sugawara Y., Asano K., Singh R., Palmour J.W., "6.2KV 4H-SiC pin Diode with Low Forward Voltage Drop", Materials Science Forum, vols. 338-342, pp. 1371-1374, 2000.

[9] Friedrichs P., Mitlehner H., Kaltschmidt, R., Weinert U., Bartsch W., Hecht C., Dohnke K.O., Weis B., Stephani D., "Static and Dynamic Characteristics of 4H-SiC JFETs Designed for Different Blocking Categories", Materials Science Forum, vols. 338-342, p. 1243-1246, 2000.

[10] Rueschenschmidt K., Treu M., Rupp R., Friedrichs P., Elpelt R., Peters D., Blaschitz P.,"SiC JFET: Currently the Best Solution for a Unipolar SiC High Power Switch", Materials Science Forum, vols. 600-603, p. 901- 906, 2009.

[11] Konstantinov A.O., Ivanov P.A., Nordell N., Karlsson S., Harris C.I.,"High-voltage operation of field-effect transistors in silicon carbide", in IEEE Electron Device Letters, vol. 18, no. 11, p. 521-522, 1997.

[12] Cooper J.A., Melloch M.R., Singh R., Agarwal A., Palmour J.W.,"Statusand prospects for SiC power MOSFETs", in IEEE Transactions on Electron Devices, vol. 49, no. 4, p. 658-664, 2002.

[13] Harada S., Kato M., Suzuki K., Okamoto M., Yatsuo T., Fukuda K. AraiK., "1.8 $m\Omega cm^2$, 10 A Power MOSFET in 4HSiC", Electro Devices Meeting, 2006. IEDM'06. International, San Francisco, p. 1-4, 2006.

[14] Tan J., Cooper J.A., Melloch M.R., "High-voltage accumulation layer UMOSFET's in 4H-SiC", in IEEE Electron Device Letters, vol. 19, no. 12, pp. 487-489, 1998.

[15] Agarwal A.K., Casady J.B., Rowland L.B., Valek W.F., Brandt C.D.,"1400V 4H-SiC Power MOSFETs", Materials Science Forum, vols.264-268, p. 989-992, 1998.

[16] Hull B.A., Jonas C., Ryu S.H., Das M.K., O'Loughlin M.J., Husna F., Callanan R., Richmond J., Agarwal A.K., Palmour J.W., Scozzie C.,"Performance of 60 A, 1200V 4H-SiC DMOSFETs", Materials Science Forum, vols. 615-617, pp. 749-752, 2009.

[17] Matsunami H., "Silicon Carbide Technology in New Era", Materials Science Forum, vols. 389-393, pp. 3-8, 2002.

[18] Bassler M., Afanas'ev V.V., Pensl G., "Interface State Density at Implanted 6H-SiC/SiO_2 MOS Structures", Materials Science Forum, vols. 264-268, p. 861-864,1998.

[19] Carter C.H., Tsvetkov V.F., Glass R.C., Henshall D., Brandy M., Muller St.G., Kordina O., Irvine K., Edmond J.A., Kong H.S., Singh R., Allen S.T., Palmour J.A., “Progress in SiC: from material growth to commercial device development”, Material Science and Engineering, vols. 61-62, p. 1- 8, 1999.

[20] Infineon Technologies AG, “Infineon releases revolutionary CoolSiC™ 1200V SiC JFET Family with direct driver technology: efficiency levels for solar inverters scale new dimensions.

[21] Growth fenomena in silicon carbide. Philips Research Reports 18(3):161–274,1963

[22] T. Kimoto. Fundalmentals of Silicon Carbide Technology. second edition, 2014

[23] T. F. Page. The Physics and Chemistry of Carbides, Nitrides and Borides. 1990.

[24] H. Jagodzinski. Eindimensionale Fehlordnung in Kristallen und ihr Einfluss auf die Röntgeninterferenzen. I. Berechnung des Fehlordnungsgrades aus den Röntgenintensitäten. Acta Crystallographica, 2(4):201–207, 1949.

[25] Lewis S Ramsdell. Studies on silicon carbide. American Mineralogist: Journal of Earth and Planetary Materials, 32(1-2):64–82, 1947.

[26] G. R. Zhdanov. Compte rende acad. Sci. URSS, 48:39–42, 1945.

[27] Woo Sik Yoo and Hiroyuki Matsunami. Solid-state phase transformation in cubic silicon carbide. Japanese Journal of Applied Physics, 30(3R):545, 1991.

[28] C. Persson and U. Lindefelt. Relativistic band structure calculation of cubic and hexagonal sic polytypes. Journal of Applied Physics, 82(11):5496–5508, 1997.

[29] S.M. Sze and K.K. Ng. Physics of Semiconductor Devices. Wiley, 2006

[30] G-F-Koster J.C. Slater. Simplified lcao method for the periodic potential problem. Physical Review 94, 1498-1524, 1954.

[31] P. Hohenberg and W. Kohn. Inhomogeneous Electron Gas. Physical Review,136:864–871, November 1964.

[32] R. A. Smith. Cerenkov Radiation and Its Applications. Pergamon Press, London.

[33] F. Bloch. Uber die Quantenmechanik der Elektronen in Kristallgittern. Zeitschrift fur Physik, 52:555–600, July 1929.

[34] Baliga B.J, Silicon carbide power devices, Singapore: World Scientific,2005.

[35] Properties of silicon carbide, Harris G.L. (Ed.), ISBN 0-85296- 870-1, Institution of Electrical Engineers, London, 1995

[36] Konstantinov A.O., Wahab Q., Nordell N., Lindefelt U., "Ionization rates and critical fields in 4H silicon carbide", Applied Physics, 71(1), pp. 90-92, 1997.

[37] Schaffer W.J., Negley G.H., Irvine K.G., Palmour J.W., "Conductivity anisotropy in epitaxial 6H and 4H SiC", MRS Proceedings, vol. 339, 1994.

[38] Hyoshi T., Masuda T., Wada K., Harada S., Tsuno T., Namikawa Y., "SiC High Channel Mobility MOSFET", SEI Technical Review,77, 2013.

[39] R.Nipoti, R Scaburri,A. Hallén and A.Parisini "Conventional thermal annealing for a more efficient p-type doping of Al+ implanted 4H-SiC" Journal of Materials Research ,28 ,2013, 17-22

[40] E. M. Handy, M. V. Rao, O. W. Holland, K. A. Jones, N. Papanicolanou, "Variable dose (1017-1020 cm-3) phosphorus ion implantayion into 4H-SiC – J. Appl. Phys, 88 (2000) 5630

[41] P. Castorina, S. Castorina, D. Lanteri “Unified description of thermal behaviors by macroscopy growth laws” Journal of Physics Communication, Vol 3, June 2019.

[42] Jian H. Zhao, Kuang Sheng, and Ramon C. Lebron-Velilla. Silicon carbide Schottky barrier diode. In Michael Shur, Sergey Rumyantsev, and Michael Levinshtein, editors, SiC Materials and Devices, volume 1, pages 117–162. World Scientific, 2006

[43] A. Sciuto,1 M. Mazzillo,2 S. Di Franco,1 F. Roccaforte,1 and G. D'Arrigo “Visible Blind 4H-SiC Pþ-N UV Photodiode Obtained by Al Implantation” EEE Photonics Journal, 7 (2015) 1–6.

[44] F.H. Ruddy et al., The fast neutron response of 4H silicon carbide semiconductor radiation detector, IEEE Trans. Nucl. Sci., 53, 1666, 2006

[45] G. Bertuccio et al., SiC x-ray detectors for spectroscopy and imaging over a wide temperature range, Mater. Sci. Forum, 433, 941, 2003

[46] L. Torrisi et al., SiC Detectors for Sub-MeV Alpha Spectrometry, Journal of Electronic Materials, 46, 7, 2017

[47] M. Cutroneo et al., High performance SiC detectors for MeV ion beams generated by intense pulsed laser plasmas, Journal of Materials Research, 28, 1, 2013

[48] L. Torrisi et al., Single crystal silicon carbide detector of emitted ions and soft x rays from power laser-generated plasmas, J. Appl. Phys., 105, 123,304,2009

[49] L. Torrisi et al., Laser-plasma X-ray detection by using fast 4H-SiC interdigit and ion collector detectors, J. Instrum. 10, 1748, 2015

[50] L. Torrisi et al., Laser-plasma X-ray detection by using fast 4H-SiC interdigit and ion collector detectors, J. Instrum. 10, 1748, 2015

[51] A. Sciuto et al., SiC interdigit detectors for post- accelerated ions generated by laser plasma, Vacuum 131, 170, 2016

[52] Olle Kordina and Stephen E. Saddow. Silicon carbide overview. In Stephen E. Saddow and Anant Agarwal, editors, Advances in silicon carbide processing and applications, volume 1, pages 1–28. Artec House Inc., 2004.

[53] R. J. Trew. SiC for microwave power applications: present status and future trends. Gallium Arsenide Applications Symposium Amsterdam, the Netherlands, 1998.

Chapter 2

Metal –semiconductor contacts

2.1 Introduction

Schottky contacts are the key component of Schottky barrier diodes (SBDs) and metal-semiconductor field effect transistors (MESFETs). The basic theory and knowledge of Schottky contacts [1] are also important in understanding ohmic contacts. Ohmic contacts play a very important role in the signal transfer to and from the semiconductor and the external circuitry. In particular, as discussed in the introduction, the resistance of the contact must be negligible with respect to that of the bulk device (the device ON-resistance), since a voltage drop at the contact adds an undesired contribution to the dissipated power, thus decreasing the efficiency of the system.

More specifically, although a variety of high-power and high-frequency SiC devices (Schottky diodes, MESFETs, VJFETs, SITs, etc.) have been demonstrated in the last years [2-5], one of the key technology issues which may limit the performances of SiC electronic devices is to obtain ohmic contacts with contact resistance, ρ_c (defined in par.2.3), in the range 10^{-5}- 10^{-6} Ω/cm^2 [6-7].

As discuss in the next sections, in order to form a good ohmic contact to a semiconductor, a metal resulting into a low Schottky barrier with the semiconductor material must be selected. In that respect, the wide band gap of SiC, about 3 times higher than that of silicon, makes almost all metals on 6H- and 4H-SiC to have a Schottky barrier height larger than ~1 eV, which presents a serious challenge to obtain a good ohmic contact on SiC with a low specific contact resistance.

Hence, in order to overcome this problem, beyond using heavily doped material for creating tunnel ohmic contacts, the most common method is the deposition of a metal layer followed by an annealing process.

In fact, the post-deposition annealing may result into a reaction of the metal with the SiC (i.e. with the formation of silicides, carbides, or ternary phases), with a consequent reduction of the barrier height or thickness.

In addition to the low resistance, the thermal stability of ohmic contacts is required for SiC devices like sensors operating at high temperatures and in harsh environments [8-10], for the aerospace applications, satellites, nuclear power instruments, etc.

In this chapter, the basic principles of Schottky contact and Ohmic contact technology and the Ohmic contact on n-type SiC are initially recalled.

Then, evaluation methods of Ohmic contact resistance and the current status of the formation of Ohmic contact on n-type SiC by conventional thermal annealing are reported.

2.2 Schottky and ohmic contacts

Metal-semiconductor contacts fall into two basic categories, the ohmic and the rectifying (or Schottky) contacts. An ohmic contact has a linear and symmetric current-voltage characteristic for positive and negative applied

voltages and a negligible resistance compared with that of the bulk of the device. Conversely, a rectifying Schottky contact is characterized by the current flow for only one voltage sign.

Fig. 2.1 shows the energy band diagram of a metal and an n-type semiconductor before they are brought into contact. The metal work function $q\varphi_m$ and the semiconductor work function $q\ \varphi_s$ are the energies required to bring an electron from the Fermi level of the material to the vacuum. The energy difference between the vacuum level and the bottom of the semiconductor conduction band E_c is defined as semiconductor electron affinity qX_s.

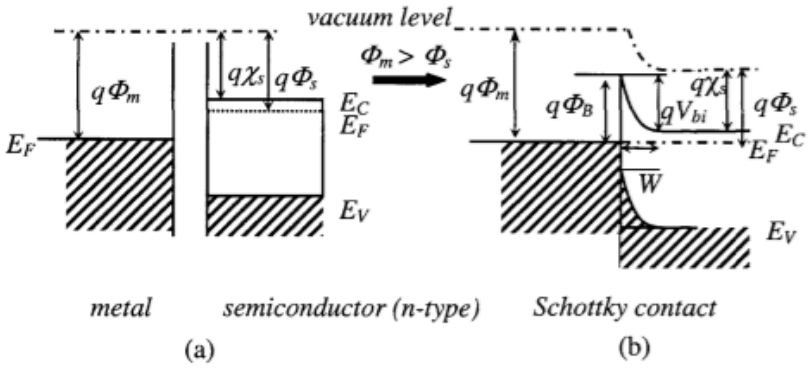

Figure 2.1: Energy band diagram for a metal-semiconductor (n-type) contact, in the case $\varphi_m > \varphi_s$ before (a) and after (b) they are brought into contact, showing the formation of a rectifying contact with a Schottky barrier height $q\varphi_B$.

When the metal and the semiconductor are brought into contact, provided the semiconductor work function $q\varphi_s$ is lower than the metal work function $q\varphi_m$, electrons will flow from the n-type semiconductor to the metal, leaving behind a positively charged donors region over the depletion width W. This charge flow continues until the thermodynamic equilibrium is reached and the two Fermi levels line up. In this way the energy level of the electrons in the semiconductor will be raised near the contact by an amount qV_{bi}, as shown in Fig. 2.1 b.

From Fig 2.1 b one finds that, for n-type semiconductor, the Schottky barrier height $q\varphi_B$ is obtained from the difference between the metal work function $q\varphi_m$ and the semiconductor electron affinity $q\chi_s$:

$$q\varphi_B = q(\varphi_m - \chi_s) \qquad (1)$$

Thus, according to the Schottky theory, the barries height of a metal/SiC strongly depends on the electron work function φ_m of the metal.

The Schottky barrier height is the most important parameter in a metal-semiconductor contact and it determines the electrical behavior of both an ohmic or a Schottky contact. The Schottky barrier can be seen as the energy necessary for electrons in the metal to penetrate into the semiconductor. On the other hand, the build-in potential V_{bi} is the barrier for electrons on the semiconductor side. It is worth noting that the Schottky barrier height $q\varphi_B$ is almost independent of the semiconductor doping concentration N_D.

Actually, there exists a weak dependence of qφ_B on $N_D$through the image force lowering of the barrier q$\Delta\varphi_B$ ($\Delta\varphi_B \propto N_D^{1/4} V^{1/4}$) [11].

On the other hand, the barrier width W depends on the doping level, being $W \propto N_D^{-1/2}$.

As is well known, a rectifying (Schottky) metal contact to n-type semiconductor is formed when the electron work function of the metal exceeds the electron affinity of the semiconductor ($\varphi_m > \chi_s$).

If the condition $\varphi_m < \varphi_s$ is satisfied, the formation of an ohmic contact can occur by band alignment, as shown in the energy band diagram reported in Fig. 2.2 (a) and 2.2 (b). Here, the transfer of electrons from the metal to the semiconductor lowers the energy levels at the interface. In this case, when

a voltage V is applied, the electrons will flow in either direction without overcome any barrier.

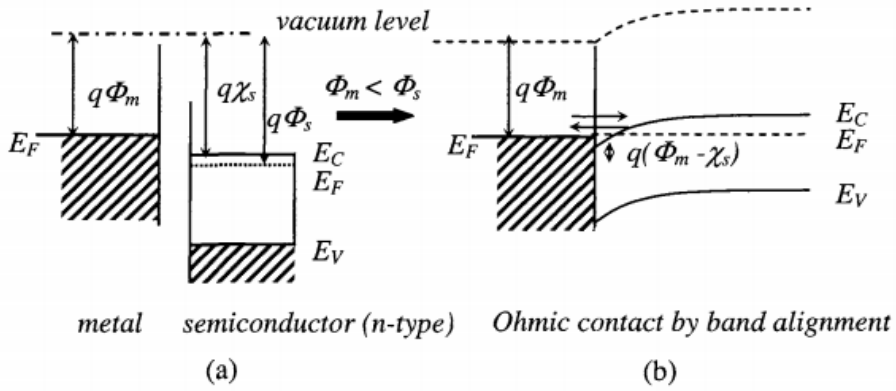

Fig. 2.2: Energy band diagram for a metal-semiconductor (n-type) contact, in the case $\varphi_m < \varphi_s$before (a) and after (b) they are brought into contact. In this case ohmic contact formation occurs by band alignment.

Since φ_m for most metals exceeds the electron affinity χ_s of 4H-SiC (see Figure 2.3), the formation of ohmic contacts to 4H-n-SiC is typically done by the deposition of the same metals as for the Schottky barriers however with subsequent annealing treatment.

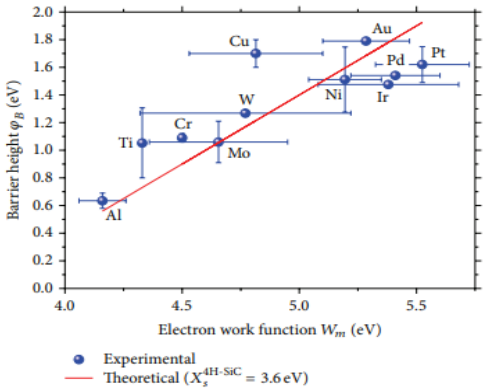

Fig. 2.3: Experimental dependence of the barrier height φ_B of metal/4H-n-SiC on the electron work function φ_m of the metals [7–10]. Red curve-theoretical dependence according to the Schottky theory (the electron affinity of 4H-SiC, Xs = 3.6 eV [11]).

Therefore, it is difficult to find metals with a low work function, satisfying the condition $\varphi_m < \varphi_s$, particularly for wide band gap semiconductors like SiC or GaN.

As recalled, the common method to form ohmic contact in wide band gap semiconductors like SiC is using a heavily doped material in such a way that when a metal is deposited onto a semiconductor layer (heavily doped N>$1{\cdot}10^{19} cm^{-3}$), the Schottky barrier will have the same height as in a low doped material but a lower thickness W, thus allowing the electrons to tunnel through the thin barrier, as schematically illustrated in Fig. 2.4.

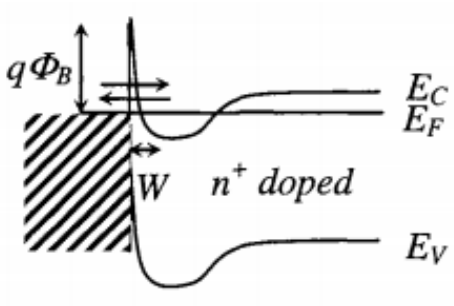

Fig.2.4. Energy band diagram for a metal-semiconductor (n-type) contact, in the case of heavy doping.

In this condition, the electrons can tunnel through the thin barrier, with the consequent formation of a tunnel ohmic contact: the carriers transport is ruled by the *field emission mechanism.*

Another mechanism of the current transport through the barrier is the *thermoionic field emission*, which is generally dominant for intermediate semiconductor doping levels N, in the range 10^{17}-10^{19} cm^{-3}. This conduction mechanism involves the carriers without enough thermal energy to surmount the barrier, as in the case of the classic thermoionic emission, but still sufficient to tunnel at an energy higher than the Fermi level, i.e. where the barrier is thinner.

For lightly doped semiconductors (N<1·$10^{17}cm^{-3}$) the main conduction mechanism is the *thermoionic emission*, i.e carriers having sufficient thermal energy to surmount the Schottky barrier can pass from a material to the other. In this case, the application of a Voltage V across a metal-semiconductor junction according to the thermoionic emission theory [11] leads to a current density J through the contact given by:

$$J = A^{**}T^2 e^{-\frac{q\Phi_B}{kT}}\left(e^{\frac{qV}{nkT}} - 1\right) \qquad (2)$$

The parameter which determines the dominant conduction mechanism turns out to be:

$$E_{00} = \frac{h}{4\pi}\left(\frac{N}{m\varepsilon}\right)^{1/2} \qquad (3)$$

where h is the Plank's constant, m the effective mass and ε the dielectric constant. E_{00} gives the relation between the temperature T and the semiconductor doping N, because kT/qE_{00} represents the ratio between the thermoionic emission current and the two other conduction mechanisms. More precisely, for lightly doped semiconductors (N<1·$10^{17}cm^{-3}$), kT/qE_{00}» l and the thermoionic emission is dominant, whereas for heavily doped semiconductors (N>1·$10^{19}cm^{-3}$), kT/qE_{00}«l and the tunneling dominates. For intermediate doping levels (1·10^{17}<N>1·$10^{19}cm^{-3}$), i.e KT/qE_{00}~1, the thermoionic field emission process is dominant.

2.3 Specific Contact Resistance: measurement methods

The contact resistance R_c, measured in Ω, is the physical parameter which characterizes the resistance of a metal-semiconductor interface which obviously depends on the area and on the geometry of the contact.

For this reason, the most useful quantity used to define the performance of an ohmic contact is the specific contact resistance ρ_c (the unit is Ωcm^2), which describes, independently on geometrical aspects, the metal-semiconductor interface specific properties, related to the barrier height of the metal, the surface preparation method, the interface roughness, etc. Indeed, all these factors, in principle independent of the contact geometry, strongly influence the value of the contact resistance.

However, in a "real" contact, like a syntered metallic contact, it may be not true that the entire contact interface takes part to the conduction.

Hence, the general, more rigorous, definition of the specific contact resistance ρ_c expressed as a function of the current density *J* is given by [12]:

$$\rho_c = \left(\frac{\partial J}{\partial V} \right)^{-1}_{V=0} \qquad (4)$$

Since different mechanisms will rule the carrier transport mechanism through the barrier, the specific contact resistance ρ_c will have a specific dependence on the barrier height $q\varphi_B$. As an example, for lightly doped semiconductors ($N<1\cdot10^{17} cm^{-3}$), where the thermoionic emission dominates the current transport, an expression for the specific contact resistance can be derived by applying Eq. (4) to the thermoionic current density J (Eq. (2)):

$$\rho_c = \frac{k}{qA^{**}T}\exp\left(\frac{q\Phi_B}{kT}\right) \qquad (5)$$

Then, in this condition ρ_c depends on the Schottky barrier $q\varphi_b$ but is independent of the semiconductor doping level N. On the other hand, for heavily doped semiconductors ($N>1\cdot10^{19}cm^{-3}$), i.e. where the tunnelling mechanism is dominant, it can be shown [13,14], that the specific contact resistance ρ_c is proportional to an exponential of φ_b divided the square root of the doping:

$$\rho_c \propto \exp\left(\frac{\Phi_B}{\sqrt{N}}\right) \qquad (6)$$

Hence, the specific resistance of tunnel ohmic contacts is strongly dependent both on the Schottky barrier $q\varphi_b$ and on the semiconductor doping N.

In the intermediate doping concentration range ($1\cdot10^{17}<N>1\cdot10^{19}cm^{-3}$) where the thermoionic field emission transport mechanism is dominant, the specific contact resistance ρ_c has a dependence of the type [12,13]:

$$\rho_c \propto \exp\frac{\Phi_B}{E_{00}\coth\left(\frac{E_{00}}{kT}\right)} \qquad (7)$$

In general, due to the inhomogeneous distribution of the current density and of the voltage below a real contact, the specific contact resistance ρ_c cannot be directly measured or simply determined using Eqs. (5-7) and indirect measurement techniques have to be used. The method of choice for the determination of the specific contact resistance in SiC, as well as in many semiconductors, is the Transmission Line Model (TLM) [14,15,16].

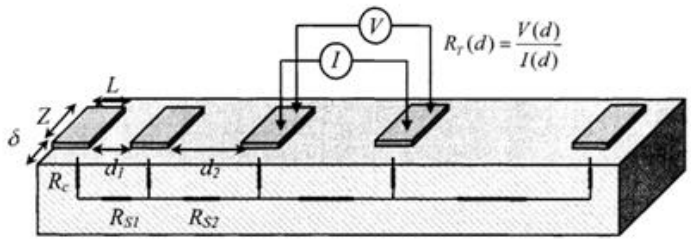

Fig 2.5: Scheme of a tipical TLM structure, the total resistance between two adjacent pads can be be determined by a current voltage (I-V) measurement.

The test structures for the TLM measurements consist of an array of identical rectangular metallic pads of length L and width Z, formed on an semiconductor mesa of width Z+28, at different spacing d, as schematically illustrated in Fig. 2.5 Assuming that δ«Z, the total resistance R_T between two adjacent pads placed at a distance d depends on both the contact resistance R_c and on the semiconductor sheet resistance R_{SH} and is given by:

$$R_T = 2R_C + \left(\frac{R_{SH}}{Z}\right)d \qquad (8)$$

Therefore, by current-voltage (I-V) measurements between the pads, the total contact resistance R_T at various pad spacing d can be determined. By reporting R_T as a function of d, a linear plot is obtained, as that shown in Fig. 2.6, in which the intercept with the y-axis is $2R_c$ while that with the x-axis is $2L_T$.The parameter $L_T$is the so called transfer length defined as the distance from the contact edge at which the current density drops to 1/e of its original value.

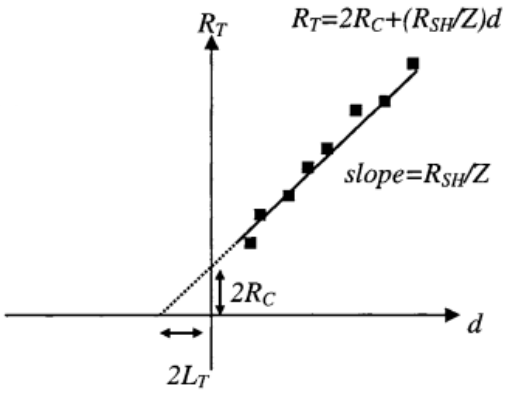

Fig 2.6. Plot of the total resistance RT as a function of the distance between the pads d, from which the contact resistance R_c, the sheet resistance R_{SH} and the transfer length L_T can be determined.

The effective contact area, i.e. the fraction of the geometric area which takes part to the current conduction, is given by $A_C = ZL_T$. The semiconductor sheet resistance R_{SH} can be extracted by the slope of the linear plot. OnceL_T has been determined, by the R_T vs d plot, the specific contact resistance can be obtained using the general expression:

$$\rho_c = R_c Z L_T tgh\left(\frac{L}{L_T}\right) \qquad (9)$$

In some special cases, the specific contact resistanceρ_c can be approximated with a simple form. For example, for electrically long contacts (L»L_T), the specific contact resistance ρ_c can be determined by the product of the contact resistance times the effective contact area as:

$$\rho_c = R_c Z L_T \qquad (10)$$

On the other hand, in the short contact limit (L« L_T), the effective contact area is coincident with the geometric area, and ρ_c is simply given by:

$$\rho_c = R_c ZL \tag{11}$$

In the general case of alloyed contacts, in which the semiconductor sheet resistance immediately below the contact can be different from to its bulk value R_{SH}, the correct value of the transfer length L_T is not simply given by the x-axis intercept of the R_T vs d/plot but it must be obtained by an additional measurement of end-contact resistance, as described in Refs. [12,16]. The previously described procedure is based on the assumption of identical contact pad and diffusion layer widths. However, in the practical cases the contact width Z is smaller than the mesa width, thus giving rise to lateral current crowding effects that reduce the accuracy of the analysis. In fact, when the diffusion layer width is wider than the contact width Z, at given R_{SH} and ρ_c, lateral current crowding produces a decrease in the measured total resistance R_T, caused by the outer conductive paths, acting like a parallel conductance. Hence, applying the simple one dimensional TLM analysis leads to a lower slope (i.e. a lower extracted R_{SH}) in the plot in Fig. 2.6, thus resulting into a higher intercept and an overestimation of the value of ρ_c. To take into account these parasitic effects, corrective factors can be evaluated using complicated two-dimensional models [17]. Practically, lateral current crowding effects can be avoided using the Circular Transmission Line Model (c-TLM), an implementation of the TLM in which circular structures of different radius are used for the determination of the specific contact resistance. The fabrication of this kind of test structures is easier than the linear TLM structure. In fact, in the c-TLM structures only one lithography masking level is required and no dry etching processes is necessary to define the diffusion layer, as instead occurs for the rectangular TLM patterns. However, in the c-TLM an extremely low metal sheet resistance is required to obtain a good accuracy of the measurement. A detailed description of this technique can be found in Refs. [18,19].

Another method for measuring the specific contact resistance is the four terminal Kelvin method [20]. In a diffused or implanted test structure, a current / is forced between two pads (1 and 2) while the voltage is measured between two other pads (3 and 4) (for a schematic of a typical Kelvin test structure see Ref. [12]). If a high impedance voltmeter is used, a very small current flows between the pads 3 and 4. Then, the potential at the pad 4 is the same as that in the semiconductor contact under the contact 3 and the specific

contact resistance ρ_c can be determined by the voltage drop between the pads 3 and 4 (V_{34}) and the contact area Ac simply using the relation

$\rho_c = V_{34} I^{-1} A_c$. This technique is suitable for very low values of specific contact resistance ($10^{-7}\Omega c m^2$) and has found a wide diffusion in the case of ohmic contacts for Si. However, since the formation of a diffused or implanted layer may be a difficult process for SiC, and the typical values of ρ_c are higher than those obtained for contact on Si, the TLM is preferred to the Kelvin method for characterizing ohmic contacts to SiC.

2.4 Ohmic contact on n-type 4H-SiC by thermal Annealing

As well known, the formation of ohmic contacts to SiC is typically done by the deposition of metals, as for the Schottky barriers, but with subsequent high-temperature annealing. Such rapid thermal annealing (RTA) produces

- the creation of a tunnel contact, which consists of a thin barrier, obtained by heavy doping of the semiconductor, through which carriers can readily tunnel;
- the formation of new compounds which reduces the barrier height and the width of the depletion region at the metal-semiconductor interface.

Usually, the metals are deposited on SiC material with a wide range of the doping concentration (obtained by epitaxial doping or by ion-implantation) and the common processes in the reaction of metals with n-type SiC, can be identified as follows:

SiC + metals (Ni or Ti, etc) → silicides (NixSiy, TiSix, etc) + carbides (TiC) + ternary phases (TiCSix) + C (carbide layer precipitate in the case of Ni)

The fabrication of ohmic contacts to SiC may be achieved using various metallization schemes and for the *n*-type SiC, typically, Ni has been the most widely used metal for Ohmic contact to n-type SiC. For p-type SiC Ti is the most used material, however in this thesis work we focused on contact on n-type SiC.

The Schottky barrier height for Ni/SiC contacts strongly depends on the surface preparation prior to metal deposition [21]. Values of $q\varphi_B$ in the range of 1.25-1.29 eV on 6H-SiC [22] and of 1.40-1.59 eV on 4H-SiC [23] are reported for unannealed Ni. These high values of $q\varphi_B$ lead to the formation of Ni/SiC rectifying contacts after deposition. Hence, post- deposition annealing processes are required to form ohmic contacts, generally at temperatures in the range 900-1000°C.

After annealing at 600 °C the I-V characteristics, see Fig. 2.7, show a rectifying behavior, whereas only after annealing at 950°C an ohmic contact is obtained. The contact resistance after annealing at 950°C, determined by the TLM method, was 3.9×10^{-5} Ωcm^2 for a doping level of $N_D = 7.4 \times 10^{18}$ cm^{-3} [24].

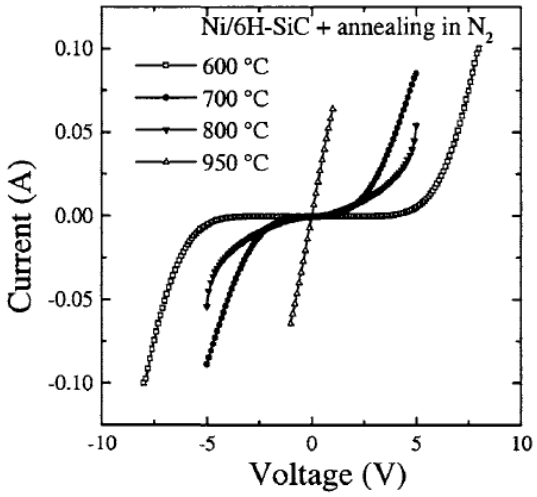

Fig,2.7: Current-Voltage (I-V) characteristics of Ni/6H-SiC contacts, annealed at different temperatures between 600 and 950°C. Ohmic behaviour is observed after rapid thermal annealing at 950°C in N_2.

As in the case of Ni contacts on silicon, where silicides form upon annealing already at low temperatures (250-400°C) [25]., the interaction between the metal and SiC determines the electrical properties of the contact. Therefore, the understanding of the structural changes of the Ni/SiC system upon annealing is central to the development of reliable contacts.

Pai et al. [26] reported the first structural investigation of annealed Ni films on SiC, carried out by combining RBS and XRD measurements. After annealing up to 400°C no detectable reaction was observed, while complete reaction of the metal film occurred at 500°C, with the formation of silicides phases. By chemical analysis one shows that nickel becomes mobile above 400°C and then can react with SiC by forming silicides [27] but ohmic behavior is observed only at higher temperatures. Therefore, a structural characterization of the reacted layer was carried out by acquiring X-ray diffraction spectra of the contacts annealed at 600°C (Schottky contact) and 950°C (ohmic contact). The XRD spectra, reported in Fig. 2.8, show the presence of the two silicide phases ($Ni_{31}Si_{12}$ and Ni_2Si) at 600°C. On the other hand, after annealing at 950°C Ni_2Si is the only observed phase. Ohdomari et al. [28] investigated the Ni/SiC interfacial reaction, with particular attention to the role of carbon during silicide formation. Auger spectroscopy indicate that elementary carbon, i.e.graphitic carbon, was present in the film and no carbides were formed. Moreover, from XRD analysis, the formation of polycrystalline Ni_2Si after annealing at 600°C was confirmed, even though the nickel rich phase ($Ni_{31}Si_{12}$) was not detected.

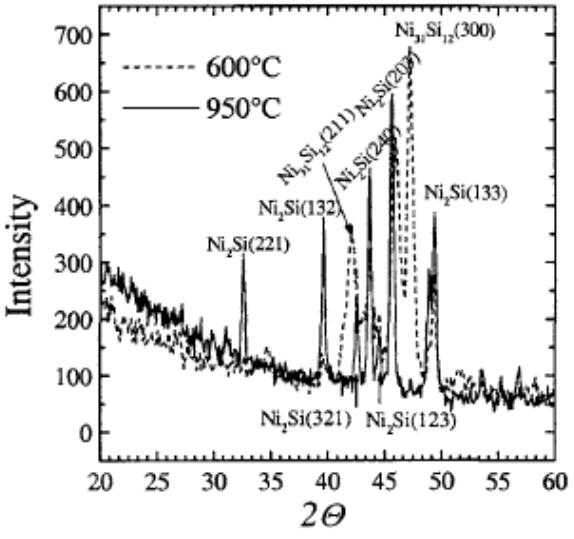

Fig. 2.8: XRD spectra of Ni/6H-SiC contacts after annealing at 600°C and at 950°C. At 600°C the coexhistence of two silicides phases ($Ni_{31}Si_{12}$ and Ni_2Si) occurs, at 950°C only the Ni_2Si phase is present.

Ni/SiC interfaces were also studied by Hochst et al.,[29] who observed the initial formation of NiSi after deposition at room temperature of a thin Ni overlayer on SiC (100). The system maintained the stability up to 600°C, and the formation of Ni_2Si was detected above this temperature. By thermodynamic considerations, i.e. from an

estimation of the free energy changes at the reaction temperature, the authors concluded that Ni-carbide (Ni_3C) is unlikely to form because it requires an input of heat, since the reaction enthalpy is positive (25 kcal/mol). Indeed, in the interaction Ni/SiC, the silicide phase $Ni_{31}Si_{12}$ is the first to be formed because the reaction is characterized by the largest negative enthalpy change [30], while thereafter the formation of Ni_2Si becomes thermodynamically favourable.

The reaction of thin Ni films was observed at lower temperatures, already at around 300°C, by Slijkerman et al.,[31] who also observed that all the carbon released during reaction accumulated on the sample surface as a continuos graphite layer. Other works on the structural characterization of the interfacial reaction of Ni with amorphous SiC also reported the first signs of reaction at around 300°C. [32-33]

As can be deduced from the aforementioned literature data, there is no good agreement on the onset temperature for reaction between Ni and SiC, on the sequence of phase formation and on the redistribution of carbon in the reacted layer.

The first quantitative electrical data on the specific contact resistance of nickel silicide ohmic contacts to n-type SiC were reported by Crofton et al. [34] who measured values of ρ_c<5xl0^{-6} Ωcm^2, in Ni_2Si contacts formed by rapid annealing in vacuum at 950°C.

The mechanism of ohmic contact formation in the nickel silicide/SiC system represents one of the most interesting topics concerning the physics of ohmic contacts to n-type SiC and was widely discussed [31-34].

Many models were proposed to explain the Schottky to ohmic transition and there are different explanations in the literature concerning the mechanisms of ohmic contact formation.

A possible reason of the formation of ohmic contacts could be a reduction of the silicide's Schottky barrier height during annealing. Indeed, Han and Lee [35] found that the effective Schottky barrier height of nickel silicides contacts on lightly doped 4H-SiC increased from 1.55 to 1.81 eV after annealing at 600°C, but again decreased to 1.25 eV after annealing at 800°C. They pointed out that the atomic composition of Si in nickel silicides at the interface increased with increasing annealing temperature and then that the silicidation process occurs through the outdiffusion of Si, with an increase of the Schottky barrier height. However, the temperature of 900°C for ohmic contact formation is higher than the onset temperature for silicide formation (about 600°C).

Hence, an excess of C atoms outdiffuse towards the surface of contact layer even after silicidation is complete, thus leaving C vacancies (Vc) below the contact. These Vc act as donors for electrons, determining an increase in net electron concentration and leading to the formation of the ohmic contact through the reduction of depletion layer width. [35] Conversely, Calcagno et al. [36] reported the distributions of the Schottky barrier heights for a set of several Ni/6H-SiC diodes, after deposition and after annealing between 600°C and 950°C. From these data an increase of

$q\varphi_B$ from 1.25 eV to 1.40 eV was observed, that cannot explain the Schottky to ohmic transition in the nickel silicide/SiC system.

Accordingly, Roccaforte et al. [38] also reported a value of barrier height of 1.42 eV for Ni_2Si/6H-SiC Schottky diodes formed under similar annealing conditions at 950°C.

Moreover, from capacitance voltage (C-V) measurements no change in the uncompensated donor concentration of the substrate was observed.[36]

Furthermore, the presence of carbon vacancies in the SiC substrate suggested by Han and Lee [35] which should introduce a level at 0.5 eV below the conduction band edge, was not experimentally revealed by deep level transient spectroscopy.[36]

More recently, La Via et al. [37] observed that a deviation from the ideal behavior in the forward I-V characteristics of Ni_2Si/SiC contacts occurs in the diodes annealed at 950°C. This behavior, which is also accompanied by a strong increase of the leakage current under reverse bias, is characteristic of the presence of interface state defects, i.e. of the formation of an inhomogenous Schottky barrier [38]. The formation an inhomogeneous Schottky barrier, characterized by the presence of low barrier regions

embedded in a uniform Ni_2Si background, may explain the ohmic behavior. In fact, in the presence of inhomogeneities through the nickel silicide/SiC interface, the current will preferentially flow throughout the low barrier regions [39], thus determining the ohmic properties of the contact. The presence of inhomogeneites of the barrier can be attributed to the complicated silicidation process and/or to the presence of fabrication-induced defects or residual oxide in the contact area.

References

[1] S. M. Sze, Physics of Semiconductor Devices, 2nd Ed., John Wiley & Sons, New York, 1981.

[2] C.E. Weitzel, J.W. Palmour, C.H. Carter, K. Moore, K.J. Nordquist, S. Allen, C. There, Silicon carbide high-power devices, IEEE Trans. Electron Devices 43, 1732-1741 (1996).

[3] K. Rottner, M. Frischholz, T. Myrtveit, D. Mou, K. Nordgren, A. Henry, C. Hallin, U. Gustafsson, A. Schoner, SiC power devices for high voltage applications, Mat. Sci. Eng. B 61-61, 330-338 (1999).

[4] R.C. Clarke, J.W. Palmour, SiC microwave power technology, Procedeeings of the IEEE 90, 987992 (2002).

[5] J.A. Cooper, M.R. Melloch, J.M. Woodall, J. Spitz, K.J. Schoen J.P. Henning, Recent advances in SiC power devices, Mat. Sci. Forum 264-268, 895-900 (1998).

[6] S. Tanimoto, H. Okushi, K. Arai, Ohmic contacts for power devices on SiC, in Silicon Carbide: Recent Major Advances, W.J. Choyke, H. Matsunami, G. Pensl eds., Springer Verlag, BerlinHeidelberg, 2004.

[7] R. Konishi, R. Yasukochi, O. Nakatsuka, Y. Koide, M. Moriyama M. Murakami, Development of Ni/Al and Ni/Ti/Al ohmic contact materials for p-type 4H-SiC, Mat. Sci. Eng. B 98, 286-293 (2003).

[8] Ts. Marinova, A. Kakanakova-Gerogieva, V. Krastev, R. Kakanakov, M. Neshev, L. Kassamakova, O. Noblanc, C. Arnodo, S. Cassette, C. Brylinski, B. Pecz, G. Radnoczi, Gy. Vincze, Nickel based ohmic contacts on SiC, Mat. Sci. Eng. B 46, 223-226 (1997).

[9] F. Roccaforte, F. La Via, V. Raineri, L. Calcagno, P. Musumeci, Improvement of high temperature stability of nickel contacts on n-type 6H-SiC, Appl. Surf. Sci. 184, 295-298 (2001).

[10] R.S. Okojie, D. Lucko, Y. L. Chen, D.J. Spray, Reliability assessment of Ti/$TaSi_2$/Pt ohmic contacts on SiC after 1000 h at 600°C, J. Appl. Phys. 91, 6553-6559 (2002).

[11] E.H. Rhoderick, R.H. Williams, Metal-Semiconductor contacts, Oxford Science Publications, Oxford, 1988.

[12] D. K. Schroder, Semiconductor material and device characterization, John Wiley and Sons, New York, 1998

[13] F.A. Padovani, R. Stratton, Field and thermoionic-field emission in Schottky barriers, Solid- State Electron. 9, 695-707 (1966).

[14] H.H. Berger, Contact resistance and contact resistivity, J. Electrochem. Soc. 119, 507-514 (1972).

[15] H.H. Berger, Model for contacts to planar devices, Solid-State Electron. 15,

[16] G.K. Reeves, H.B. Harrison, Obtaining the specific contact resistance from transmission line model measurements, IEEE Electron Device Lett. 3, 111-113 (1982)

[17] M. Finetti M, A. Scorzoni, G. Soncini, Lateral current crowding effects on contact resistance: Measurements in four terminal resistor test patterns, IEEE Electron Device Lett. 5, 524-526 (1984).

[18] G. K. Reeves, Specific contact resistance using a circular transmission line model, Solid-State Electron. 23, 487-490 (1980).

[19] A.J. Willis, A.P. Botha, Investigation of ring structures for metal-semiconductor contact resistance determination, Thin Solid Films 146, 15-20 (1987).

[20] S.J. Proctor, L.W. Linholm, A direct measurement of interfacial contact resistance, IEEE Electron Device Lett. 3, 294-296 (1982).

[21] F. Roccaforte, F. La Via, V. Raineri, L. Calcagno, P. Musumeci, G.G. Condorelli, Highly reproducible ideal SiC Schottky rectifiers: effects of surface preparation and Thermal annealing on the Ni/6H-SiC barrier height, Appl. Phys. A 77, 827-833 (2003).

[22] F. Roccaforte, F. La Via, V. Raineri, F. Mangano, L. Calcagno, Temperature dependence of the c-axis mobility in 6H-SiC Schottky diodes, Appl. Phys. Lett. 83, 4181-4183 (2003).

[23] M. Treu, R. Rupp, H. Kapels, W. Bartsch, Temperature dependence of forward and reverse characteristics of Ti, W, Ta and Ni Schottky diodes on 4H-SiC, Mat. Sci.Forum 353-356, 679-682(2001).

[24] F. Roccaforte, F. La Via, V. Raineri, L. Calcagno, P. Musumeci, Improvement of High temperature stability of nickel contacts on n-type 6H-SiC, Appl. Surf. Sci. 184, 295-298 (2001).

[25] S.P. Muraka, Self-aligned silicides or metals for very large scale integrated circuit applications, J. Vac. Sci. Technol. B 4, 1325-1331 (1986).

[26] C.S. Pai, CM. Hanson, S.S. Lau, X-ray diffraction and ion backscattering study of Thermally annealed Pd/SiC and Ni/SiC, J.App. Phys. 75, 618-619 (1985).

[27] F. Roccaforte, F. La Via, A. Baeri, V. Raineri, L. Calcagno, F. Mangano, Structural And electrical properties of Ni/Ti Schottky contacts on silicon carbide upon thermal annealing, J. Appl. Phys. 96,4313-4318 (2004).

[28] Ohdomari, S. Sha, H. Aochi, T. Chikyow, S. Suzuki, Investigation of thin Ni/single-crystal SiC interface reaction, J. Appl. Phys. 62, 3747-3750 (1987).

[29] H. Hochst, D.W. Niles, G.W. Zajac, T.H. Fleisch, B.C. Johnson, J.M. Meese, Electronic structure and thermal stability of Ni/SiC (100) interfaces, J. Vac. Sci.Technol. B 6,1320-1325 (1988).

[30] M. Levit, I. Grimberg, B.Z. Weiss, Interaction of Ni90Tiio alloy thin film with 6H-SiC single crystal, J. Appl Phys. 80,167-173 (1996).

[31] W.F. Slijkerman, A.E.M.J. Fischer, J.F. van der Veen, I. Ohdomari, S. Yoshida, S. Misawa, Formation of the Ni-SiC (001) interface studied by high-resolution ion backscattering, J. Appl. Phys. 66, 666-673 (1989).

[32] M. Nathan, J.S. Ahearn, On the nanometer-scale solid-state reactions at thin-film Ni/amorphous SiC and Co/amorphous SiC interfaces, J. Appl. Phys. 70, 811-820 (1991).

[33] A.S. Edelstein, D.J. Gillespie, S.F. Cheng, J.H. Perepezko, K. Landry, Reactions at amorphous SiC/Ni interfaces, J. Appl. Phys. 85, 2636-2641 (1999).

[34] J. Crofton, P.G. McMullin, J.R. Williams, M.J. Bozack, High-temperature ohmic contact to n-type 6H-SiC using nickel, Appl. Phys. Lett. 77, 1317-1319 (1995).

[35] S.Y. Han, J.L. Lee, Effect of Interfacial Reactions on Electrical Properties of Ni Contacts on Lightly Doped n-Type 4H-SiC, J. Electrochem. Soc.149, G189-G193 (2002).

[36] L. Calcagno, E. Zanetti, F. La Via, F. Roccaforte, V. Raineri, S. Libertino, F. Giannazzo, M. Mauceri, P. Musumeci, Schottky-Ohmic transition in nickel silicide/SiC system: is it really a solved problem?, Mat. Sci. Forum 433-436, 721-724 (2003).

[37] F. La Via, F. Roccaforte, V. Raineri, M. Mauceri, A. Ruggiero, P. Musumeci, L. Calcagno, Schottky-Ohmic transition in nickel silicide/SiC 4H system: the effect of non uniform Schottky barrier, Mat. Sci. Forum 457-460, 861-864 (2004).

[38] R.T. Tung, Recent advances in Schottky barrier concepts, Mat. Sci.Eng,.R 35, 1-138 (2001).

[39] F. Roccaforte, F. La Via, V. Raineri, R. Pierobon, E. Zanoni, “Richardson's constant in inhomogeneous silicon carbide Schottky contacts” J. Appl. Phys. 93, 9137-9144 (2003).

Chapter 3

Ohmic contact on SiC by laser processes

3.1 Introduction

As mentioned in chapter 1, thinning the substrate allows reducing the resistive contribution down and therefore the wafer grinding step has become mandatory in SiC technology to minimize the total device R_{ON}.

From this point of view, laser annealing represents an alternative valid solution for achieving the silicidation with a limited heat transfer. Moreover, the use of laser annealing in back Ohmic contact formation enables the possibility to complete the device front side first, and then to process the back-side contact without detrimental effects for the Schottky barrier and without limitation on the thinning of the wafers.

In this chapter, one recalls some aspects on the formation of Ohmic contacts to SiC thinned substrate using laser annealing (LA) processes, suitable both for diode and MOSFET technology [1]. Moreover, the specific code used for the simulation of crystal phase and thermal budget will be introduced [2].

3.2 Laser annealing and SiC: a brief review

Laser annealing (LA), with highly uniform beams in space (over ~cm^2 areas) and nanosecond range pulses, is the reference annealing technique in micro- and nano-electronics when strongly confined heating is needed in the processes flow [3-9]. The key-features of this process are:

(a) the low in-depth thermal diffusion;
(b) the huge temperature gradient and rate;
(c) the possibility to melt localized zones with a nanometer resolution.

Thanks to these particular characteristics, laser annealing is nowadays widely applied as a post-fabrication annealing step to activate isolated doped regions (e.g. back junctions) with a null or strongly reduced heating of the other zones of the devices [10, 11].

Table I summarizes the laser types and their applications for SiC processing.

Application	Laser	λ	Material	Comment
Annealing				Ion implanted zones recover
	Excimer	193 nm, 248 nm, 308 nm	Ion implanted damage zones (amorphous)	from amorphous to polycrystalline up to 500 nm deep
	Nd:YAG	355 nm	Amorphous film on dielectric	Direct write of a-SiC converted to poly-SiC ~50 nm thick
	Argon (CW)	514.5 nm	Amorphous film	Direct write of recrystallized zones of a-SiC to poly-SiC
Via hole drilling				High ablation rate
	CO_2, 30 ns *Q*-switched	10.6 μm	4H-SiC	0.47–1.8 μm pulse^{-1}
	Excimer	248 nm	4H-SiC	Ablation rate ~0.23 μm pulse^{-1}
	Ti:sapphire (femtosecond pulses)	800 nm	4H-SiC	Ablation rate ~0.25 μm pulse^{-1}
In situ doping				*n*-type (nitrogen) doping, 600 nm
	Nd:YAG	1064 nm	4H-SiC, 6H-SiC	deep junction
				p-type (Al^+) doping, 4.3 μm deep junction
	Excimer	193 nm	4H-SiC, 6H-SiC	*n*-type (nitrogen) doping, 50 nm deep junction
				p-type (Al^+) doping, 150 nm deep junction
Electroless metallization	Excimer	193 nm, 308 nm	Single crystal (hexagonal)	Catalytic sites of Si nanoclusters and thermal stress facilitate
	Cu vapor	510 nm		electroles s Cu and Ni contacts
Nanostructuring	Ti:sapphire (femtosecond pulses)	800 nm	3C-SiC, 4H-SiC, 6H-SiC	Circular polarization: Spherica l nanoparticles, Linear polarization: nanoripples

Table I: Laser processing applications of SiC.

Before discussing in more details the previous points (a,b), it is useful to recall the structure of the contact formed by laser annealing compared to RTA annealed contacts [12].

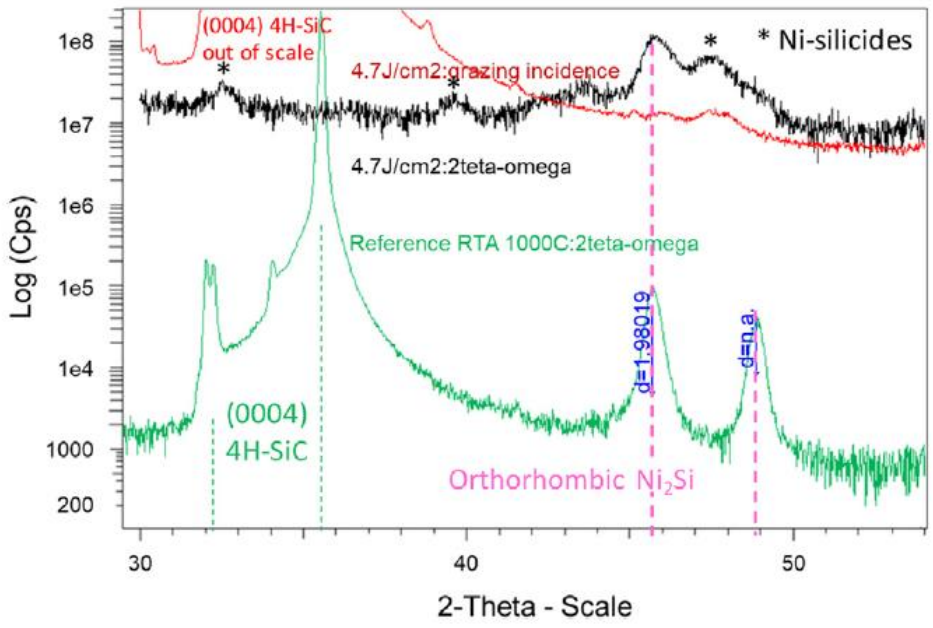

Fig.3.1: XRD pattern of the back-side layer after laser treatment (black line): Ni 100 nm after 4.7 J/cm^{2}compared with a reference sample (RTA): (green line) grazing incidence profile;(red line) 2theta-omega profile. The labelled peak positions in blue identify the orthorhombic Ni_2Si phase [12].

The XRD pattern (see Fig 3.1) shows the formation of Ni_2Si for both samples (LA and RTA treatments) and the large full width at half maximum of the peaks (compared to the reference case-RTA sample), produces the peaks overlap and marks the presence of a fine-grained material as reaction product.

From the morphological point of view, SEM and TEM have been perfomed for LA sample, see Figs 3.2-3.3.

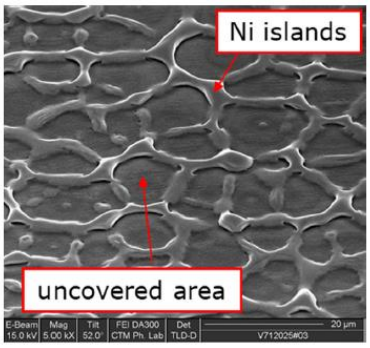

Fig.3.2: SEM in plan view of the back-side layer after 100 nm Ni sputtering and 310 nm laser treatment at an energy density of 4.7 J/cm^2.

SEM in plan view (Fig.3.2) shows the covered and uncovered Ni regions. The Ni islands observed, composed of nickel silicide in a Ni_2Si crystal phases, are mixed with random distributed spherical carbon clusters. Moreover, a continuous layer of C cluster has also been detected at the interface with SiC, as typically seen in standard RTA Ni-based contacts. On the other side, structure and chemical distribution of the uncovered areas turn out to be more complex and unexpected.

By TEM investigation, Fig 3.3, one observes a 350 nm thick defective region, composed of three different layer: a 10 nm continuous layer on the surface: (1), an intricate network of crystal grains and spherical clusters in the middle (2) and a (3) crystalline SiC layer with a high density of fault in the stacking sequence.

The composition of the first two layers in the uncovered area were detected by using scanning TEM configuration and electron energy loss (EEL) spectrum image acquisition. Thanks to the parallel acquisition, point by point, of the high angle annular dark field image (HAADF) and EEL spectrum, the two dimension chemical maps of the elements present in the marked area have been obtained, see Fig.3.3b. Three different elemental maps (carbon, silicon and nickel) have been extracted and over imposed in the RGB image showed in Fig. 3.3d to recognize carbon accumulation on the surface (green continuous layer), pure silicon grains (blue) and pure carbon sphere (green) enveloped by a network containing nickel (violet).

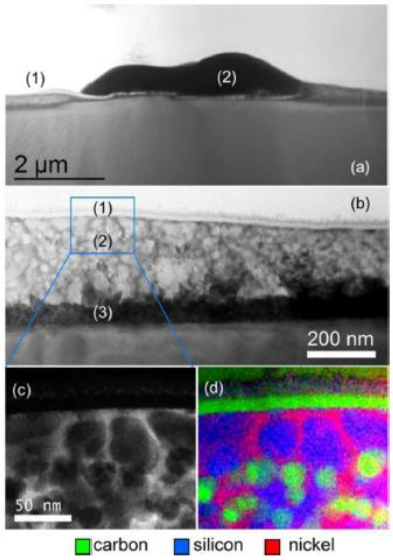

Fig. 3.3: TEM images of the laser treated Ni/SiC interface, which leads to uncovered area (a-1) and Ni agglomeration (a-2). Three different layers in the uncovered regions are identified (b-1, b-2, b-3). HAADF STEM image (c) together with map of elements (d), of the marked area in fig b.

Fig. 3.4 shows a schematic of the C-AFM experimental setup employed for high resolution mapping of current injection through the LA Ni back-contact. A representative morphology and the corresponding current map acquired on a large scan area (50 µm × 50 µm) are reported in Fig. 3.4b and 3.4c, respectively.

By comparing the morphological and electrical maps, one notes that the injected current levels in the uncovered regions are similar to those measured on the Ni covered islands and this interesting observation clarifies that the total current density flows through the device, independently on the elemental distribution.

Furthermore, it indicates that the Ohmic behavior of the LA back contact is guaranteed by the thermal reaction needed to form the Nickel Silicide rather than the Ni_2Si itself.

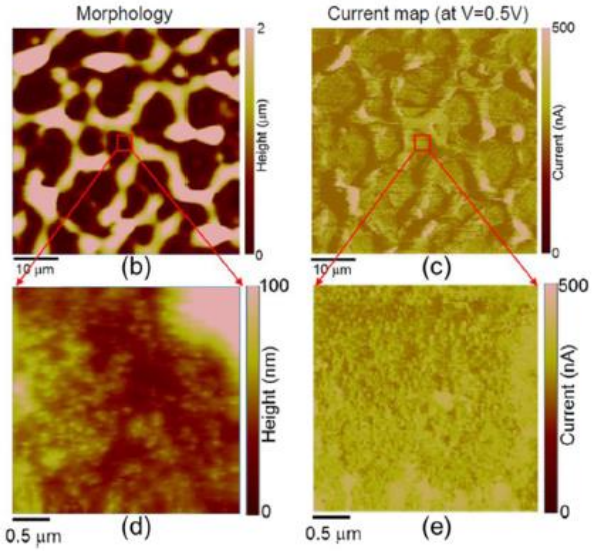

Fig.3.4: Schematic of C-AFM probe (a). Morphology map (b, d) and current map (c, e).

Finally, Fig.3.5 shows the I-V characteristic at 175 °C of the SiC JBS diodes processed with laser annealing (110 µm thick) in comparison with that ones obtained by standard RTA process (180 µm thick). Despite of the better electrical behavior observed in the case of contacts processed by standard RTA treatments (see Fig. 3.6) the benefit on the reduction of the substrate resistive contribution is clearly visible. Then, the gain in the forward voltage drop V_F at high current level represents indirectly the benefit in terms of surge current ruggedness of diodes on thinned substrate.

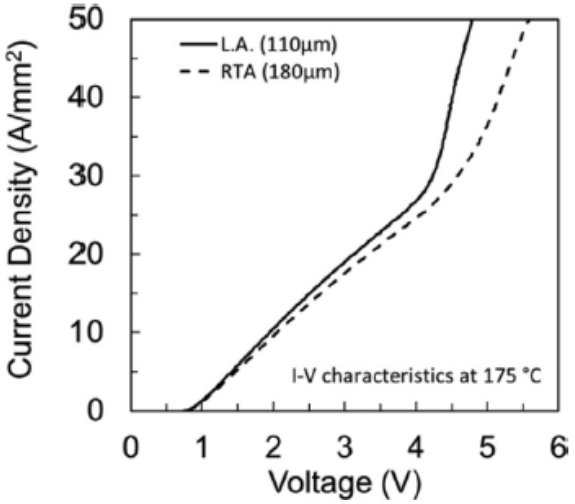

Fig.3.5: Forward I-V characteristic at 175 °C of 650 V SiC JBS diodes with different substrate thickness (110 µm vs 180 µm) and back-side contact process (Laser annealing vs RTA).

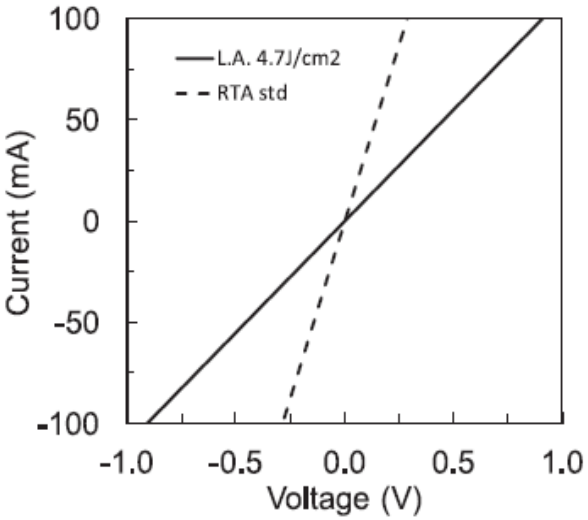

Fig.3.6:I-V curves acquired on adjacent TLM patterns of Ni-based Ohmic contacts formed by standard RTA (1000 °C) and Laser annealing processes (at an energy density of 4.7 J/cm^2).

The formation of ohmic contact can be performed by NiSi deposition on 4H-SiC also. In this contest, a main difference is the size of the carbon clusters, which are formed as a consequence of the SiC consumption during the reaction with the excess Ni in the deposited NiSi layer. In case of laser annealing the carbon is very fine dispersed in the resulting NiSi matrix (Fig.3.7a), whereas the traditional annealing process causes quite large C clusters to be formed (Fig. 3.7b).

As large carbon clusters always bear the risk of contact metal delamination (peeling) due to weak adhesion within the graphitic structure of the carbon clusters, the finer grained structure leads to a better integrity of the contact metal stack.

As on the other hand the C clusters are also needed for the formation of a low ohmic contact to n-SiC [13] a well distributed network of very small clusters is a good precondition for a homogenous current flow through the contact area.

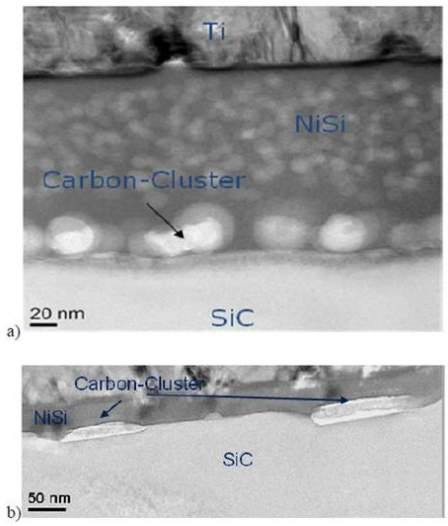

Fig 3.7*:* a) TEM picture of the backside metal stack with laser annealed NiSi layer (150 ns, 3.8 J/cm²). Spherical C-Clusters with a typical diameter of 20-40 nm are visible at the SiC interface.
b) TEM picture of a backside metal stack with RTP annealed NiSi layer (90s, 980°C). Large longitudinal C-clusters are visible at the SiC interface.

Coming back to the initial aspects (a-b), the heat flow into the material is determined by the thermal penetration length L_e, which is defined by

$$L_e = 2\sqrt{D\tau_p}, \qquad (1)$$

where D is the material thermal diffusivity and τ_ρ is the laser pulse width.
From this it is evident that the thermal penetration length of nanosecond lasers should be orders of magnitude higher than that of the femtosecond and even picoseconds lasers.
Detailed modeling has been employed using a modified heat diffusion equation 2 and the Beer–Lambert equation

$$\frac{\partial T}{\partial t} = \frac{\alpha}{\rho C_p} I(z,t) + \frac{1}{\rho C_p}\frac{\partial}{\partial z}\left(\kappa\frac{\partial T}{\partial z}\right), \qquad (2)$$

$$I(z,t) = I_o(t)(1-R)\exp(-\alpha z), \qquad (3)$$

where T is the absolute temperature, t is the time, ρ is the density, C_p is the specific heat, k is the thermal conductivity, I_o is the laser intensity at the surface, R is the surface reflectivity, α is the optical absorption, z is the depth below surface, and $I_{z,t}$ is the laser intensity at a depth z below the surface. Equations 2 and 3 are commonly used for pulsed excimer laser annealing, [14-16] but have also been used to model heating during dopant incorporation [17]. Ultraviolet (UV) excimer lasers are useful for annealing SiC surfaces disordered by ion implantation since the optical absorption of amorphous SiC and crystalline SiC is on the same order of magnitude. Table II summarizes the optical absorption of crystalline and amorphous SiC for the excimer laser family.

	ArF		KrF		XeCl	
	Crystalline	Amorphous	Crystalline	Amorphous	Crystalline	Amorphous
Reflectivity ($R\%$)	40	34.6	28.6	33.6	24.3	32.4
Optical absorption (cm^{-1})	1.50×10^{6}	1.10×10^{6}	1.40×10^{5}	8.70×10^{5}	4.50×10^{4}	6.00×10^{5}

Table II: Optical absorption for excimer laser wavelengths.

The laser irradiation model and heating have been used to optimize laser parameters that reach the melting temperature of 4H-SiC and 6H-SiC [14] substrates for annealing.
In this respect, the energy absorbed by a contact depends mostly on the thickness and the optical properties of the deposited metal layers. In some cases, the top metal layer highly reflects the laser beam. Then, finding an optimal top layer can be crucial in order to maximize absorption and reach a sufficient interface temperature to form the expected ohmic Metal(M)/Si/C phases. As a result, the temperature reached at the M/SiC interface might not be sufficient to form these phases mandatory to achieve a good ohmic behaviour. For this reason, finding a top layer, with good laser light absorption, is crucial. In these conditions, by UV wavelength and the very short pulse laser, the heat is localized at the wafer top surface reaching very high surface temperature, for ultra-thin wafers also, thus for a short timing and keeping the opposite surface close to room temperature.
The surface temperature is indirectly controlled by the laser energy density (ED) per pulse. In Figure 3.8a the simulated temperature profile as a function of the wafer depth (at the end of the laser pulse) and the corresponding time evolution (Figure 3.8b) is presented for different laser annealing conditions.

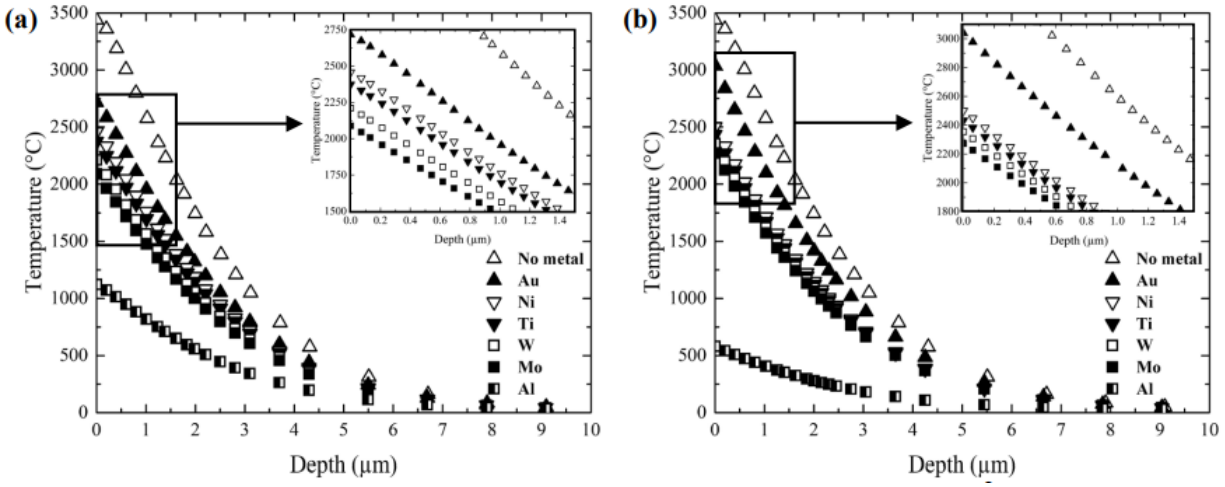

Fig. 3.8: Temperature profile in 4H-SiC, just after the laser pulse (2.5 J.cm-2) as a function of the metallization layer. Metal thicknesses are 20 nm (a) and 100 nm (b).

3.3 Laser annealing and SiC: simulations

The application of LA in electronic devices is hindered by the difficulties in the process control. Indeed, pulsed laser processes activate a complex ultrafast material evolution characterized by different stages and kinetic pathways when process parameters vary. As a consequence, the final result of this evolution can be experimentally studied, whereas the time dependent details are beyond the experimental analysis.

In order to gain a complete scenario, software packages of the LA process able to effectively simulate the process effects in complex 2D and 3D electronic device geometries have been proposed [2].

In particular, the simulations reported in chapter 4 are based on the LIAB (LASSE Innovation Application Booster) package, which is implemented by Finite Element Method solution of partial differential equations and unifies in a single framework several literature models and some original formulations. The main features of the LIAB package, with a large range of possible applications, are:

• Versatile Graphical User Interface for the structure design, the material assignment and the simulation analysis;

• Multiple materials calibration (optical and thermal properties, mass transport) as a function of T and phases [18];

• Efficient coupling with Electromagnetic Simulations for the self-consistent source estimate (i.e. power dissipation) in nano-structured topographies;

• Experimental validation in nano-structured samples;

• Multiple-dopant models simulating dopant redistribution, including dif fusion solubility and segregation [19];

• Alloy model e.g. SiGe (where the melting point depends on the alloy fraction) [20];

• multiple phase models (e.g. amorphous, liquid, crystal) [21].

In this thesis (Chapter 4) the LIAB package will be applied to wafers sample of Ni on SiC to study the time dependent phase evolution and temperature profile.

More precisely, the evolution framework derived from the simulations can be qualitatively separated in three main regimes: sub-melting, partial- melting, full-melting characterized by the following different features [22]:

a) a sub-melting regime, i.e. the low fluence range, where the systems remain solid during the whole heating/cooling cycle and the main phenomena (both boosted by the temperature increase) are the intermixing, which starts at the Ni/4H-SiC interface, and the subsequent early and limited silicide formations, if the Si density is above solid solubility threshold [22],

b) a partial melting regime where a limited region of the Ni-rich layer melts, whilst the rest of the layer remains solid, after an initial intermixing and silicide formation due to the temperature increases. During the processes, the solid portion follows an evolution similar to the sub-melting case whereas the molten region deviates from that evolution in the melting transient stage, as discussed later on. In all the investigated cases, the molten phase is almost ideal liquid Ni-Si-C alloy with the eventual co-presence of solid carbon (C-cluster). Consequently, during the melting stage silicide compounds, formed during the heating (see case a), locally release Si and Ni in the monomer forms. The intermixing of the molten region is very strong due to the high diffusivity of the monomer species in the liquid. After solidification, while the temperature is still high, the formation of silicide

restarts, but the intermixed state is completely different from the one achieved in the solid portion.

c) In the full melting regime (higher fluences) the whole Ni-rich layer melts (from the surface to the 4H-SiC substrate). The evolution in the previous item for the molten region extends with similar characteristics to the whole Ni-rich film.

References

[1] R. Rupp, R. Kern, R. Gerlach, Laser backside contact annealing of SiC Power devices: a prerequisite for SiC thin wafer technology, Proc ISPSD 2013 (2013) 5 54.

[2] S.F. Lombardo, G. Fisicaro, I. Deretzis, A. La Magna, B. Curver, B. Laspinasse, K. Huet, Theoretical study of the laser annealing process in FinFET structures, Appl.Surf. Sci. 467–468 (2019) 666–672.

[3] K. Huet, G. Fisicaro, J. Venturini, H. Besauc`ele, A. La Magna, Defect kinetics and dopant activation in submicrosecond laser thermal processes, Applied Physics Letters 95 (23). 324

[4] F. Ruffino, A. Pugliara, E. Carria, L. Romano, C. Bongiorno, G. Fisicaro, A. L. Magna, C. Spinella, M. Grimaldi, Towards a laser fluence dependent nanostructuring of thin au films on si by nanosecond laser irradiation, Applied Surface Science 258 (23) (2012) 9128 – 9137, eMRS 330 2011 Spring Symp J: Laser Materials Processing for Micro and Nano 331 Applications.

[5] G. Fisicaro, A. La Magna, Modeling of laser annealing, Journal of Computational Electronics 13 (1) (2014) 70–94. doi:10.1007/s10825-013- 335 0545-9. 336 URL

[6] G. Fisicaro, K. Huet, R. Negru, M. Hackenberg, P. Pichler, N. Taleb, A. La Magna, Anomalous impurity segregation and local bonding fluctuation in l-si, Phys. Rev. Lett.110 (2013) 117801. 340 doi:10.1103/PhysRevLett.110.117801. 341

[7] Y. Qiu, F. Cristiano, K. Huet, F. Mazzamuto, G. Fisicaro, A. L. Magna, M. Quillec, N. Cherkashin, H. Wang, S. Duguay, D. Blavette, Extended Defects formation in nanosecond laser-annealed ion implanted silicon, Nano Letters doi:10.1021/nl4042438.

[8] G. Impellizzeri, E. Napolitani, R. Milazzo, S. Boninelli, M. Cuscuna, G. Fisicaro, A. La Magna, G. Fortunato, F. Priolo, V. Privitera, Role of oxygen on the electrical activation of B in Ge by excimer laser annealing, physica status solidi doi:10.1002/pssa.201300308.

[9] S. Lombardo, S. Boninelli, F. Cristiano, G. Fisicaro, G. Fortunato, M. Grimaldi, G. Impellizzeri, M. Italia, A. Marino, R. Milazzo, 357 E. Napolitani, V. Privitera, A.L. Magna, Laser annealing in Si and Ge: Anomalous physical aspects and modeling approaches, Materials Science In Semiconductor Processing 62 (2017) 80 – 91, advanced doping methods in semiconductor devices and nanostructures.
doi: http://dx.doi.org/10.1016/j.mssp.2016.10.047.

[10] G. Fisicaro, M. Italia, V. Privitera, G. Piccitto, K. Huet, 364 J. Venturini, A. La Magna, Dopant activation and damage evolution in implanted silicon after excimer laser annealing, physica status solidi 8 (3) (2011) 940–943. 367

[11] G. Fisicaro, M. Italia, V. Privitera, G. Piccitto, K. Huet, J. Venturini, A. La Magna, Solid phase phosphorous activation in implanted silicon by excimer laser irradiation, Journal of Applied Physics.doi:10.1063/1.3592262. 374

[12] S. Rascunà, P. Badalà, C. Tringali, C. Bongiorno, E. Smecca, A. Alberti, S. Di Franco, F. Giannazzo, G. Greco, F. Roccaforteb M. Saggio "Morphological and electrical properties of Nickel based Ohmic contacts formed by laser annealing process on n-type 4H-SiC" Materials Science in Semiconductor Processing 97 (2019) 62–66

[13] Seyller, T; Emtsev, KV; Speck, F; Gao, KY; Ley, L: "Electronic structure of graphite/6H-SiC interfaces", Silicon Carbide and Related Materials 556-557 (2007) pp.701-704.

[14] R. Reitano, P. Baeri, and N. Marino, "Excimer laser induced thermal evaporation and ablation of silicon carbide," Appl. Surf. Sci. 96– 98, 302–308(1996).

[15] Dutto, E. Foggarassy, and D. Mathiot, "Numerical and experimental analysis of pulsed excimer laser processing of silicon carbide," Appl. Surf. Sci. 184, 362–366.

[16] A. Hedler, S. Urban, F. Falk, H. Hobert, and W. Wesch, "Excimer laser crystallization of amorphous silicon carbide produced by ion implantation," Appl. Surf. Sci. 205, 240–248,2003.

[17] Z. Tian, I. A. Salama, N. R. Quick, and A. Kar, "Doping Methods Used to Dope Silicon Carbide," Acta Mater. 53, 2835–2844 _2005_.

[18] A. La Magna, P. Alippi, V. Privitera, G. Fortunato, M. Camalleri, B. Svensson, A phase-field approach to the simulation of the excimer laser annealing process in Si, Journal of Applied Physics (9) (2004) 395 4806–48 doi:10.1063/1.1690861

[19] R. Milazzo, E. Napolitani, G. Impellizzeri, G. Fisicaro, S. Boninelli, M. Cuscuna, D. De Salvador, M. Mastromatteo, M. Italia, A. La Magna, G. Fortunato, F. Priolo, V. Privitera, A. Carnera, N-type doping of Ge by As implantation and excimer laser annealing, Journal of Applied Physics.

[20] G. Fisicaro, A. L. Magna, G. Piccitto, V. Privitera, Laser annealing of Si and Ge based devices, Microelectronic Engineering 88 (4) (2011) 387 488 – 491, post-SiCMOS electronic devices: the role of Ge and III-V materials.

[21] S. F. Lombardo, S. Boninelli, F. Cristiano, I. Deretzis, M. G. Grimaldi, K. Huet, E. Napolitani, A. La Magna, Phase field.

[22] S. Sanzaro, C. Bongiorno, P. Badalà, A. Bassi, I. Deretzis, G. Franco, G. Fisicaro, P. Vasquez, A., A. La Magna, Simulations of the ultra-fast kinetics in Ni-Si-C ternary systems under laser irradiation, Materials, submitted.

Chapter 4

Silicidation with pulsed-laser annealing: experimental results

As mentioned in chapter 2, for the n-type SiC, annealed Ni-films are commonly used to form nickel silicide. The standard silicidation process (RTA) represents today a technological bottleneck, due to the complexity of the process flow integration that requires multiple flip over of the wafers and to the reliability of back-side layer due to the exposition to the remaining steps in the flow.

In this context, the introduction of wafer grinding, to reduce the resistive contribution of the substrate, brings great advantage in terms of device power dissipation.

Laser annealing represents a valid technological solution for the formation of Ohmic contacts based on Ni on SiC for its suitable depth of penetration and the consequent localized annealing.

For the analyses included in this thesis, Nickel films, 100 nm thick, have been sputtered on the back-side of heavily doped 110 μm 4H-SiC thinned substrates after mechanical grinding.

Then, to achieve Ohmic behavior, the metal films have been irradiated with an UV excimer laser with a wavelength of 310 nm, with different energies per pulse and with multiple pulses.

Morphological and structural properties of the reaction products have been characterized by means of SEM (Scanning Electron Microscopy), XRD (X-ray Diffraction), TEM (Transmission Electron Microscopy) and RBS (Rutherford Backscattering Spectroscopy) which has low sensitivity but turns out to be useful to determine the thickness and the stoichiometry of the reacted Ni layer.

Finally, RBS and laser process simulations have been performed in order to predict respectively the stoichiometry of the reacted layer and the temperature evolution and the material modifications during irradiation.

4.1 Experimental methods

The backside contacts have been made on highly doped *n* -type 4H-SiC substrates, thinned down to 110 μm by mechanical grinding. Ni layers 100 nm-thick have been deposited on grinded SiC surface by DC sputtering in Ar ambient at a base pressure of 1×10^{-3} mbar. Since the silicide reaction can be very sensitive to impurities at the interface between Ni and substrate [1,2,3], an *in-situ* sputter etching step preceded Ni deposition in order to ensure a proper interface cleaning.

The Ni surfaces have been then irradiated under nitrogen atmosphere by an excimer laser at single, double and triple pulse with a duration of 160 ns, wavelength of 308 nm and using several energy densities (fluences φ) in the range between 1.8 and 3.8 J/cm^2. The spot size is 10 mm x 10 mm.

Structure and composition of the silicide contacts have been studied by XRD analysis, by a Bruker AXS D8 DISCOVER diffractometer working with a Cu-K source and a thin attachment; by TEM coupled with EDX, using a JEOL-JEM microscope working at 200 keV; by RBS with He^{2+} source and energy of 2 MeV.

The LIAB computation tool (see [2] Chap.3 for the detailed presentation of the approach) has been used for the laser annealing simulation.

The electrical characterization has been performed by using a KLA-Tencor OmniMap RS75 for Four Point Probe measurements, a semiconductor device parameter analyzer (Agilent B1500A) and a high-power curve tracer (Sony Tektronix 371A).

In the following paragraphs the results obtained for the different laser characteristics (see table I) will be discussed, starting from the deposited sample and then proceeding with Ni/SiC annealed samples.

Pulse	Energy densities (J/cm^2)
1X-2X-3X	**1.8**
1X-2X-3X	**2.4**
1X	**3.2**
1X-2X-3X	**3.8**

Table 1: Different laser conditions for Ni/SiC samples.

4.2 Results

4.2.1 Compositional and structural characterization

- ***As deposited Ni/SiC: RBS analysis***

RBS characterization of Ni/SiC deposited was perfomed in order to controll the thickness of Ni deposited on SiC surface.

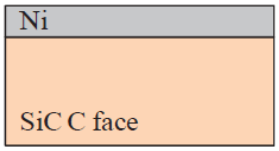

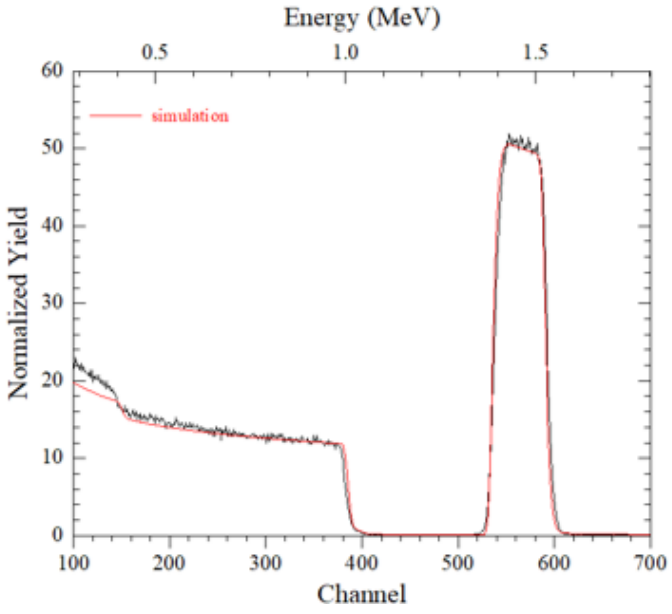

Layer	*Composition (%)*	*Thickness (10^{15})*
1	*Ni 100*	*1066 at/ cm^2*
2	***Si 50.0 C 50.0***	***20000 A***

Fig 1: RBS spectrum (black line) combined with RUMP simulation (red-line) for Ni/SiC as deposited.

The RBS simulation of the experimental data (see Fig.1) shows a Ni thickness deposited on back-side SiC about 120 nm, evaluated by considering the density of Ni of $0.91x10^{23}$ at/cm^3 (calculated by structural considerations).

- ***Ni/SiC after 1X 1.8 J/cm^2***

I) Compositional characterization: RBS analysis

RBS characterization of the LA treated Ni films have been performed (red line) and in Fig.2 is reported the comparison with previous Ni/SiC-as deposited sample (black line), showing no difference. This result is in agreement with the RBS spectrum obtained by simulations (see Fig. 2 green line and table) where there is no difference in thickness of the reacted layer and silicides stoichiometry: the spectra Ni/Si as-deposited and Ni/SiC after treatment are perfectly superimposable, as expected due to low energy to activate the reaction.

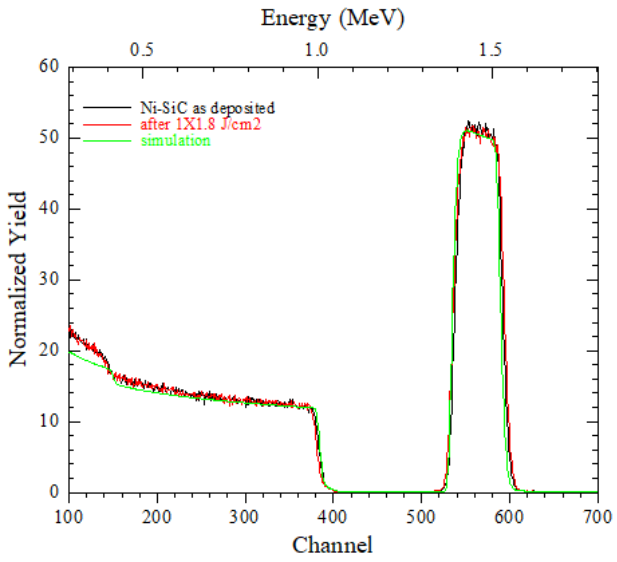

Layer	*Composition (%)*	*Thickness (10^{15})*
1	*Ni 100*	*1066 at/ cm^2*
2	***Si 50.0 C 50.0***	***20000 A***

Fig.2: RBS spectra for Ni/SiC as-deposited (black line), Ni/SiC after 1X1.8J/cm^2 (red line) and Rump simulation (green line).

Similar results are obtained for 2X and 3X 1.8 J/cm^2 samples as reported in Fig.3, where the various spectra are shown. As sake of completeness, the simulation of the temperature on depth is depicted in Fig.4, in which the maximum temperature on surface turns out to be ≈1200 K(see Fig.4a) and it reaches room temperature at a depth of about 10 μm (Fig.4b).

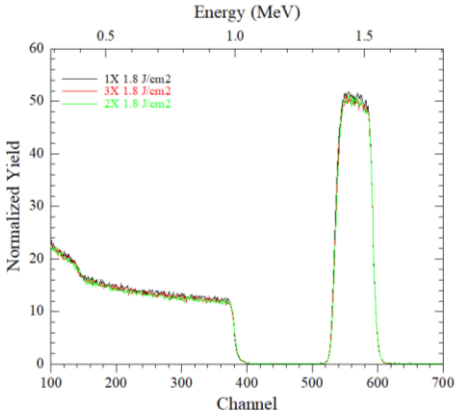

Fig 3: RBS spectra for Ni/SiC samples after 1X-2X-3X at 1.8 J/cm^2 .

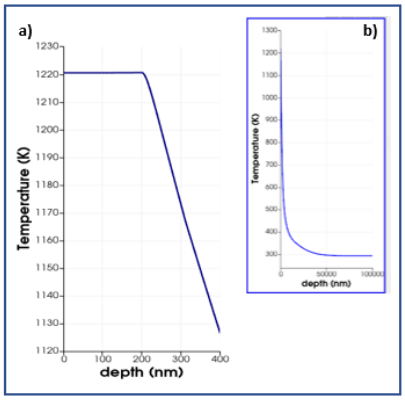

Fig.4: a) Temperature as a function of depth, b) temperature profile considering a depth of 100 μm.

Based on the RBS results and T simulations, one expects no activation of the reaction between Ni and Si at multiple pulses also. For this reason the other characterizations have not been applied.

- ***Ni/SiC after 1X 2.4 J/cm^2***

I) Morphological and compositional characterization: TEM and EDX analysis

The morphology and the local structure of the Ni/SiC after irradiation with 1 shot laser at 2.4 J/cm^2 is performed by TEM analyses.

After LA process an increase of 22 nm in the layer thickness is observed by TEM. This layer is made of big grains and defects such as inclusions and twins. The reacted layer is shown in Fig 5a-b.

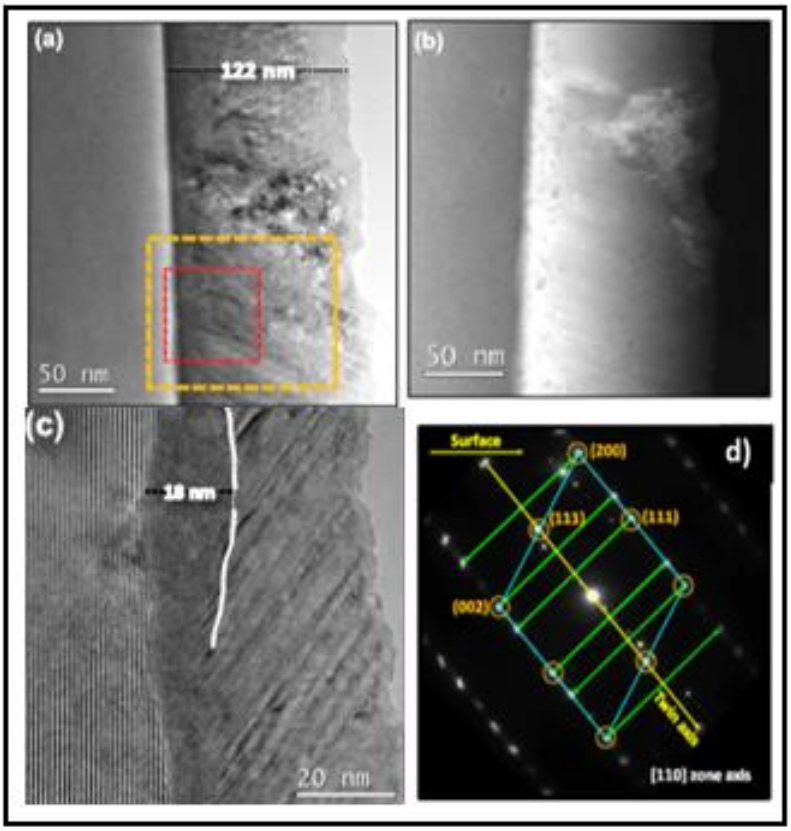

Fig.5: Cross-sectional TEM imagines (a)in bright field and (b) dark field of the Ni/SiC annealed 1 shot at 2.4 J/cm^2 c) Magnification of the red panel in Fig.5a d) SAED image take on the topmost cubic layer having [111] twins rotation (rotation by 180 ° around the twin axis).

The TEM imagine in dark field (see Fig. 5b), shows the presence of C-clusters at 5-7 nm away from the 4H-SiC substrate and a few small C-clusters can be rarely found up to 20 nm. The magnification of the red panel of Fig.5a, in Fig.5c, detects a difference of the morphology between the layer at the interface with 4H-SiC (10-20nm-thick) and the remaining Ni layer. In particular, the presence of twinned defects extending up to the interfacial layer is clearly visible and tipical diffraction patterns with spots arranged in a cubic structure as in the Ni lattice, see Fig.5d, in which is reported Selected Area Electron Diffraction (SAED).

STEM assisted by EDX analyses is applied in order to obtain the local chemical spatial distribution for each species of interest, i.e. Ni, Si, and C.

The Fig.6 shows EDX spectrum of the light blue panel in the STEM image in inset.

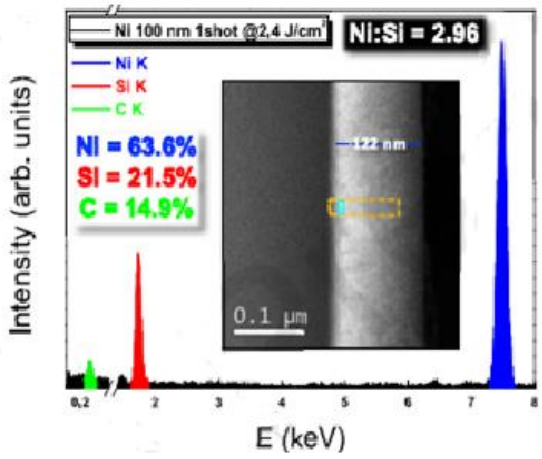

Fig.6: EDX spectrum of the light blue panel in the STEM image in inset.

The quantitative analysis gives a ratio Ni:Si ≈3:1 and then the silicides phase formed in the interfacial layer with 4H-SiC substrate is Ni_3Si, that is a cubic phase.

Fig.7 shows more details related to chemical composition in the remnant of the Ni layer.

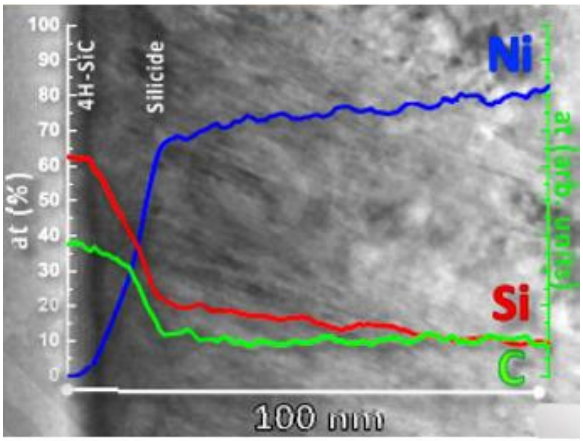

Fig7: EDX atomin distribution profile in the region inside the yellow panel in Fig.5a and inset of Fig.6.

In order to obtain the atomic distribution profile of the species of interest (Ni, Si, C), STEM analysis probed a region 100 nm thick, as indicated in the selected yellow area in Fig 5.a and insert Fig.6. Thus, a first layer (10-20 nm) has been found with composition in agreement with what observed in the Fig.6 and moreover, the atomic concentration of Si gradually decreases while approaching the sample surface.

Fig.8 shows the trend of the Ni:Si ratio on along the layer thickness: a growing pattern of the Ni:Si is presented with a value 3:1 in proximity of the interface, whilst the Ni:Si ratio progressively increases in going toward the surface, describing a Ni matrix with Si diffused inside.

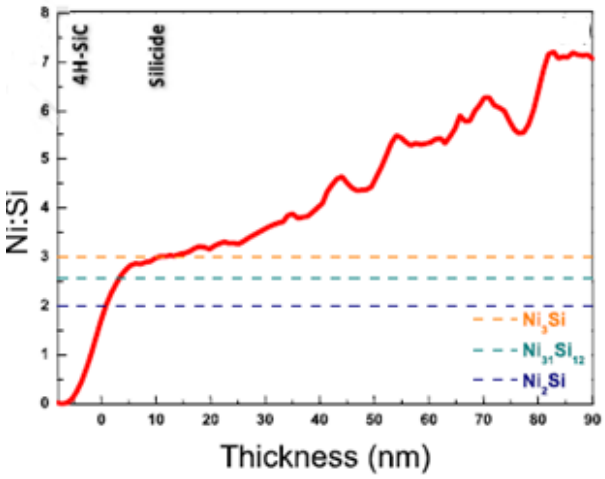

Fig.8: Ni:Si ratio profile from the interface with 4H-SiC through entire layer

II) ***Structural characterization: XRD analyses***

XRD analyses are perfomed in different scan configurations, symmetric and grazing incidence, in order to get structural information before (black line) and after (red line) LA.

Figs.9a-b show the acquisition in symmetric configuration and related rocking curve and indicate that the reference sample is highly textured along the [111] direction of the face-centered-cubic Ni structure.

After one pulse of laser at 2.4 J/cm^2, the material maintains the same preferential orientation along the [111] direction even if the main (111) peak is larger than in the reference sample (see Fig.10).

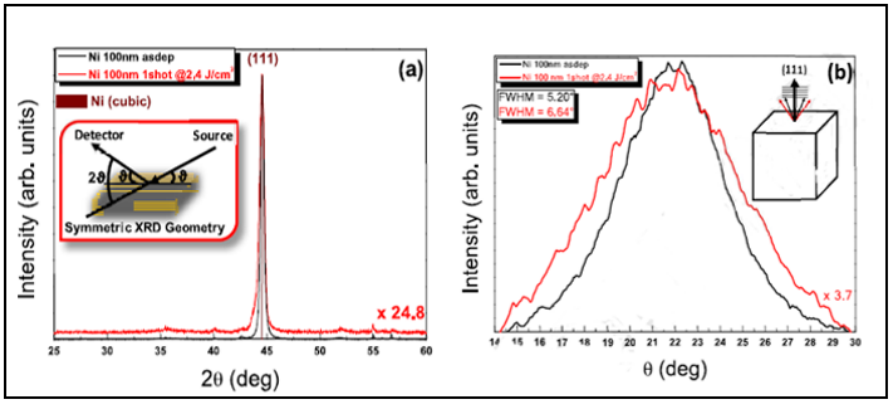

Fig. 9: (a) Normalized XRD patterns in symmetric configuration of the Ni sample laser annealed with one pulse at 2.4 J/cm^2 for 160 ns (black line) and in as deposited condition (red line). (b) normalized Rocking curves of the treated vs the untreated sample.

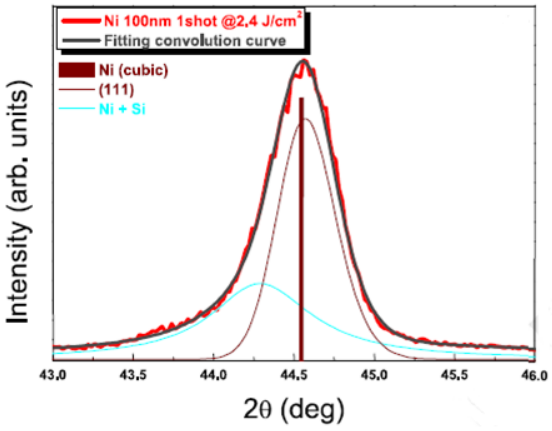

Fig.10: Magnification and deconvolution contributions in the range around the main (111) peak.

As shown in Fig.10, this broadening is asymmetric toward lower 2θ values, and this is accounted by the presence of a second peak at 2θ=44.266°.

The extra peak in Fig. 10 is attributed to Si diffusion into Ni matrix that increases the d-spacing (d= interplanar distance). Moreover, the size of domains with high crystallographic order (crystallite size) associated to this Ni-Si alloy is smaller than that one extracted by the Ni peak (21nm), showing a structural change of the starting metalization layer. The ratio between the areas under the Ni and Ni + Si peaks depicted, provided a qualitative comparison between the two materials, although the difference arising from the scattering factors (likely lower in the mixed phase) was not considered.

Rockin curve, see Fig.9-b gives information on the spread of the main growth axis. It is possible to estimate a higher Full Width at Half Maximum (FWHM) for sample annealed with respect to the reference one (the peak is also less intense) to verify if the sample has partially lost its starting structural order.

XRD analysis in grazing incident configuration, see Fig.11, shows two main peaks (111) and (200) for annealed sample respect to reference sample, because the reference Ni layer is textured with preferential (111) growth planes.

The magnification of this image in the range 41-53 deg (Fig.12), evidences that those contributions in the laser treated sample are due to the formation of a cubic β-Ni_3Si phase, in full agreement with the previous EDX data.

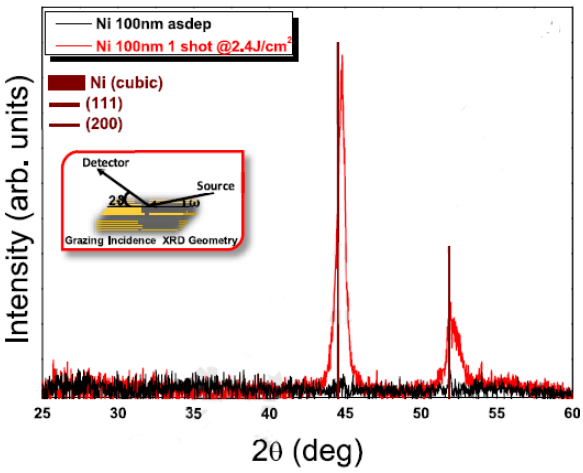

Fig.11: XRD patterns in grazing incidence configuration of the layer annealed at 2.4 J/cm^2 (black line) and in as deposited condition (red line).

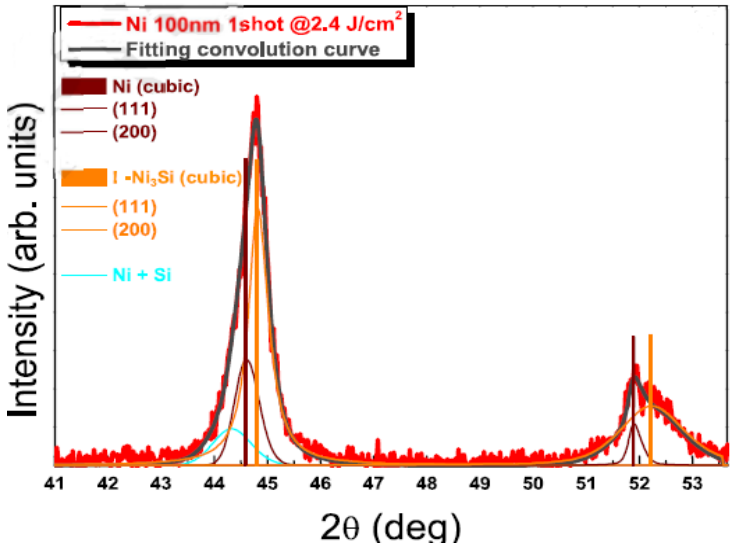

Fig.12: Magnification and deconvoluted contibutions of the treated sample in the range around main (111) and (200) peaks acquired in grazing incidence configuration.

III) Compositional characterization: RBS analysis

According with EDX and XRD data, the RBS spectrum and the corresponding simulation indicate that, at the present energy, a layer, of Ni_3Si stoichiometry at interface Ni/SiC has been formed, followed by a compound of Ni and Si atoms, see Fig. 13 and corresponding table.

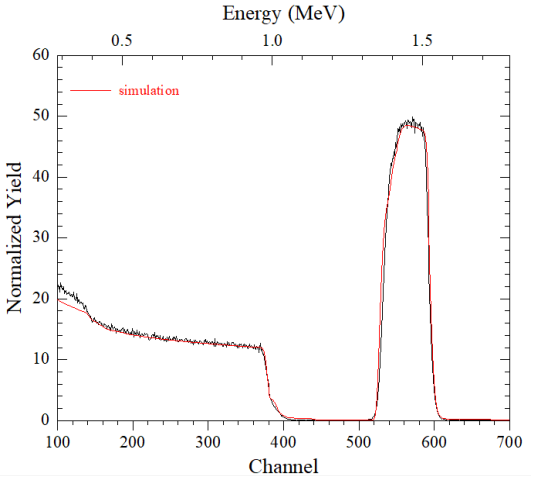

Layer	*Composition (%)*	*Thickness (10^{15})*
1	*Ni 93.26 Si 1.76 C 4.97*	*810 at/ cm²*
2	*Ni 77.44 Si 4.50 C18.05*	*230 at/ cm²*
3	*Ni 55.65 Si 15.65 C 28.69*	*110 at/ cm²*
4	***Si 50.0 C 50.0***	***20000 A***

Fig.13: RBS spectrum of Ni/SiC after 1X2.4J/cm² (black line) and simulation (red-line).

Similar results are obtained by increasing the shot number (2X-3X pulses) at 2.4J/cm^2.

IV) ***Phase field and T simulation***

The T_{max} turns out to be 1628 K, with an increase of about 40% with respect to the previous simulation at 1.8 J/cm^2 and it has an analogous depth dependence.

One observes the formation of different silicides at the interface, with a more Ni-riched phase, Ni_3Si, and minor Ni_2Si and $Ni_{31}Si_{12}$ structures, see Fig 14 a. In Fig.14b the simulation of C-clusters distribution is reported showing the presence of C clusters mainly at the Ni/SiC interfacial with a very low concentration.

The similar behaviour observed for 1X-2X-3X at 2.4 J/cm^2 suggests that the increase of energy density could affects the silicide formation.

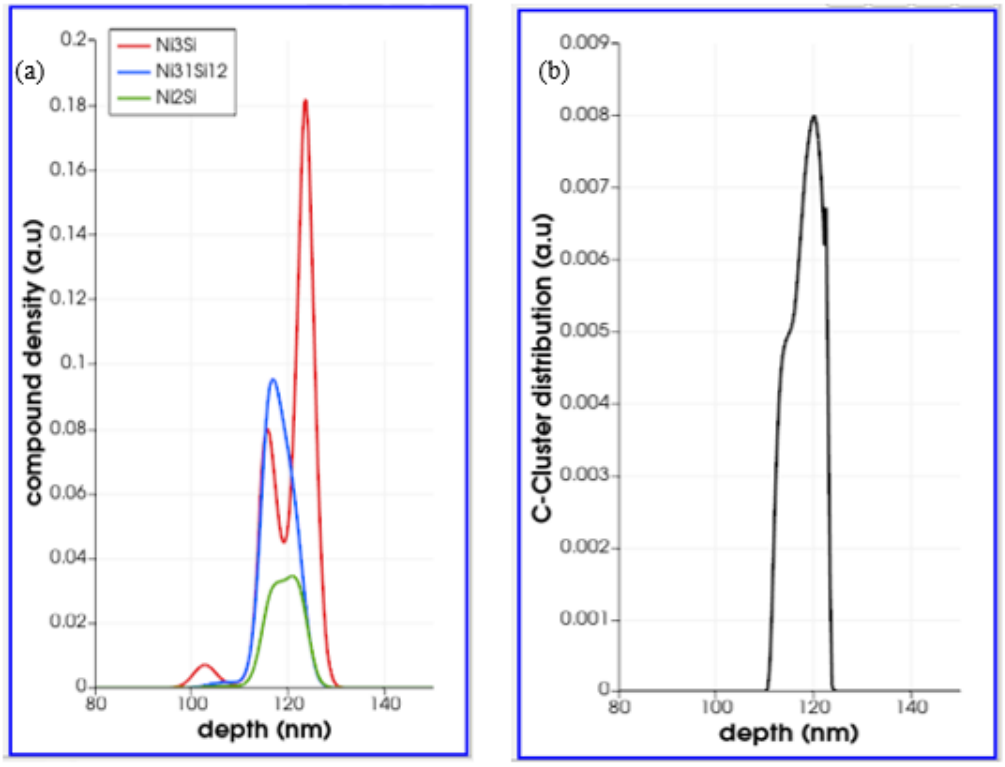

Fig.14: a) simulated phase at interface; b) C cluster distribution simulation as a function of depth.

- ***Ni/SiC after 1X 3.2 J/cm^2***

  I) Morphological and compositional characterization: TEM and EDX analysis

The morphology and the local structure of the Ni/SiC after irradiation with 1 shot laser at 3.2 J/cm^2 (TEM) shows a further increment of the interfacial layer thickness compared with the previous case (22 nm at 2.4 J/cm^2 vs 48 nm at 3.2 J/cm^2) after LA.
However, the uppermost part of the layer maintains the same morphological properties, i.e., big grains with defects such as inclusion and twins (see Fig.15-a).

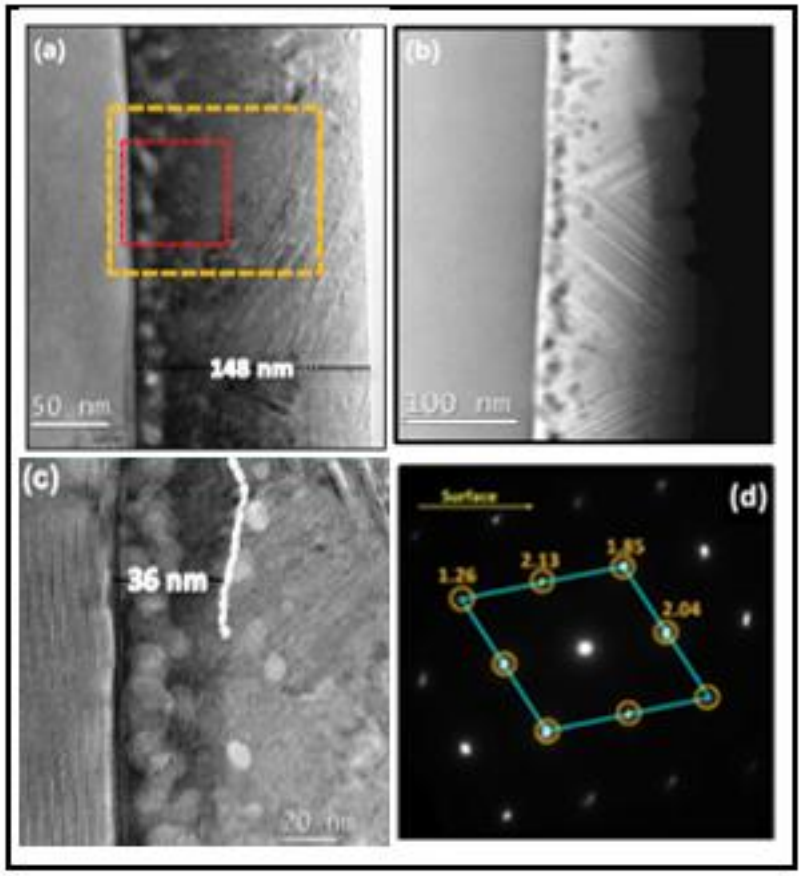

Fig15: Cross-sectional TEM imagines (a)in bright field (b) dark field of the Ni/SiC annealed 1 shot at 3.2 J/cm^2 c) Magnification of the red panel and d) SAED image taken at interfacial layer that testifies silicide in a not cubic phase.

The C- Clusters, increased in number and size, are confined within first 5-7 nm from the substrate even if some C-clusters are found up to 50 nm from the interface.

More details on the morphologicall difference between the layer at the interface and the substrate are reported in Fig.15c. Twin defects extend up to the border on the interfacial layer as shown in Fig.15-c and the diffraction patterns is referable to a cubic and hexagonal lattices, see Fig. 15-d.

Fig.16 gives the EDX spectrum related to the selected light blue area of Fig.15a (7 nm thick at the interface) of the STEM image reported as inset.

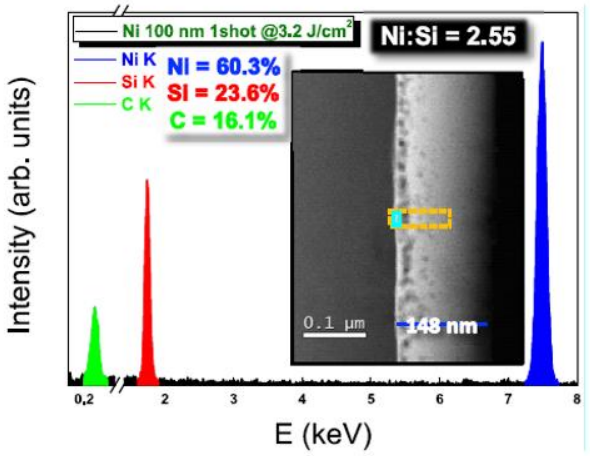

Fig.16: EDX spectrum of the light blue panel in the STEM image in inset.

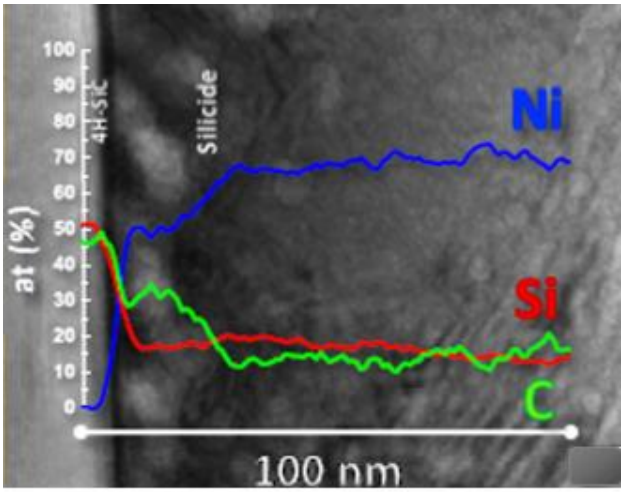

Fig.17: EDX atomin distribution profile in the region inside the yellow panel in Fig.15-a and inset of Fig.16.

The chemical compositions in the Ni layer, Fig.17, indicate a silicide layer at the interface of about 30-40 nm, in agreement with the thickness observed in Fig.15c. Also in this setting the atomic concentration of Si gradually decreases toward the surface with a Ni:Si trend that is shown in Fig.18 but with a reduces slope with respect to the energy shot at 2.4 J/cm^2, implying a more diffused Si in the pristine nickel layer.

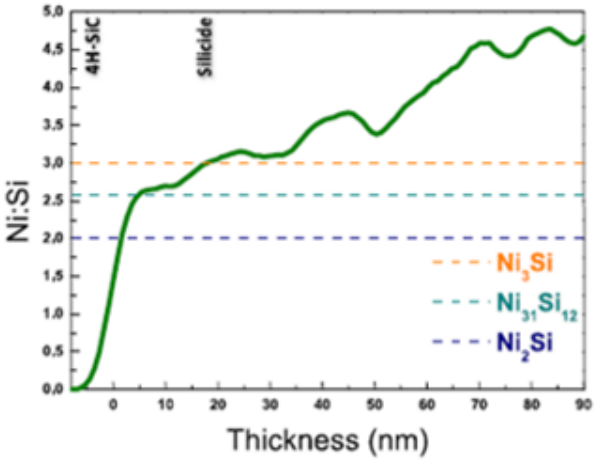

Fig.18: Ni:Si ratio profile from the interface with 4H-SiC through entire layer

I) ***Structural characterization: XRD analyses***

XRD data are reported in Figs.19 a-b where the green line is referred to sample after one pulse at 3.2 J/cm^2 while black line is the reference sample.

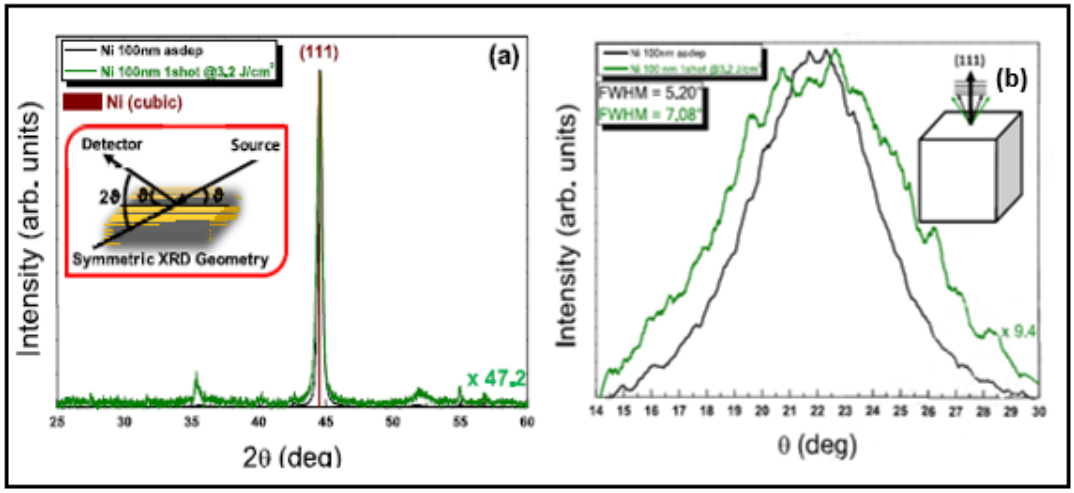

Fig.19: a) Normalized XRD patterns in symmetric configuration of the Ni sample laser annealed with one pulse at 3.2 J/cm^2 for 160 ns (green line) and in as deposited condition. (black line). b) Normalized Rocking curves of the treated vs the untreated sample.

The annealed sample maintains the texturing along the [111] direction (see Fig.19a-b) and the main (111) peak associated to nickel is also broader (and less intense) compared to the reference case and narrower than the sample treated at 2.4 J/cm^2, as described by the corresponding FWHM values: FWHM $_{(ref)}$= 0.325, FWHM $_{(2.4\text{J/cm}^2)}$ = 0.385 and FWHM $_{(3.2\ \text{J/cm}^2)}$ = 0.332 (see Fig.20). The reduction of this parameter for the sample annealed at 3.2 J/cm^2 represents an improvement of the lattice order that could be due to the increased temperature during laser treatment.

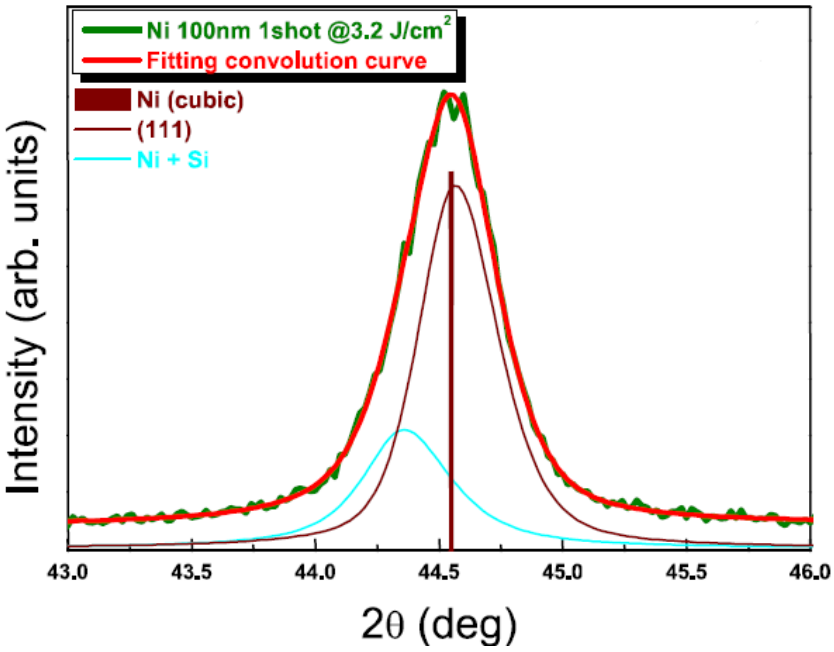

Fig.20: Magnification and deconvolution contributions in the range around the main (111) peak.

Also in this case, the peak is asymmetric with a second left-side component due to Ni+Si alloy. The relative area of this additional component with respect to the nickel peak is less than in the sample at 2.4 J/cm^2.

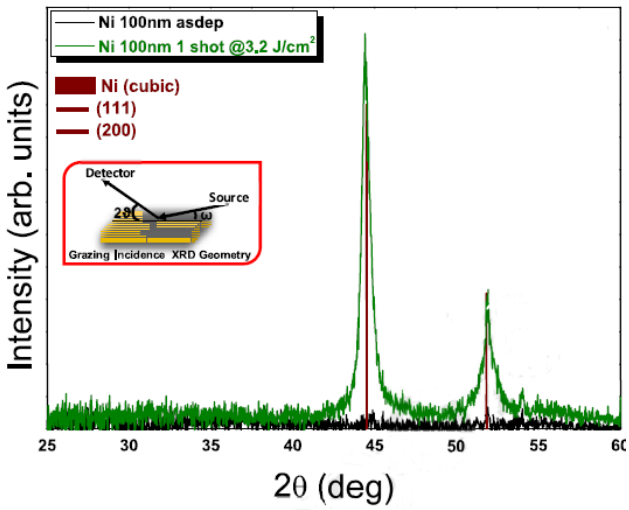

Fig.21: XRD patterns in grazing incidence configuration of the layer annealed at 3.2 J/cm^2 (green line) and in as deposited condition (black line).

The grazing incidence configuration by XRD analysis are reported in Fig.21 where two main peaks are slightly left shifted with respect to the reference sample, (see Fig.22) and this signature is associated to the formation of the silicide phase such as the hexagonal β-$Ni_{31}Si_{12}$.

The main component under the peak at 2θ=44.55° is due to a Ni+ Si alloy, other main deconvolution results are attribuited to γ $Ni_{31}Si_{12}$ at 2θ=43.984°, pure nichel at 2θ=44.588° and β-Ni_3Si at 2θ= 44.802°. It has to be further noticed that the peak at 2θ 51.8° is also a convolution of different contributions, including two of the more Si-rich γ-$Ni_{31}Si_{12}$ phases.

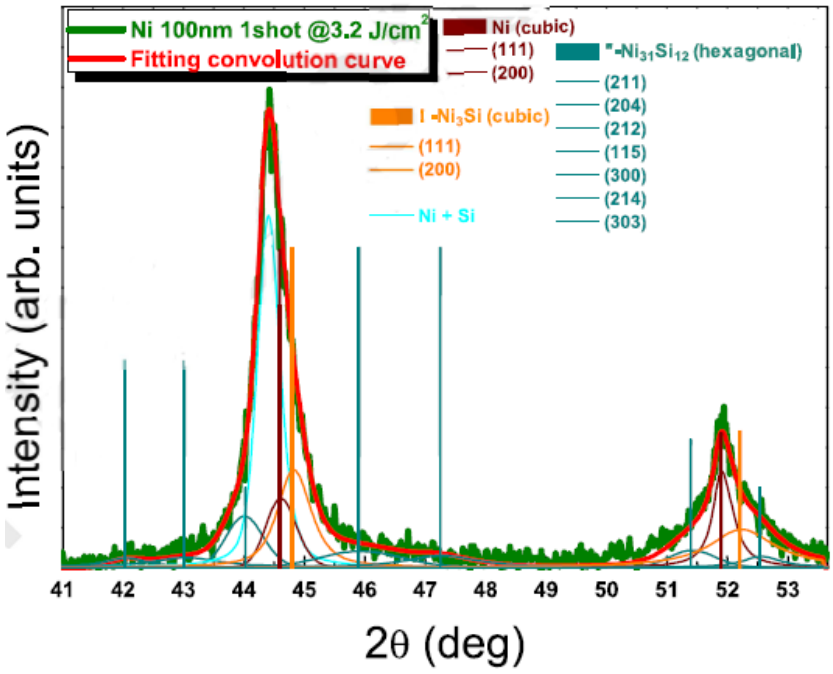

Fig.22: Magnification and deconvoluted contibutions of the treated sample in the range around main (111) and (200) peaks acquired in grazing incidence configuration.

Comparison with 2.4 J/cm^2 case implies that the raising of fluence moves the reacted phases towards more Si-rich-silicides.

II) Compositional characterization: RBS analysis

RBS data and the numerical simulation detect a Ni-riched interfacial layer in agreement with EDX and XRD observations, with a stoichiometry ≈ Ni_3Si, (see Fig.23 and related table).

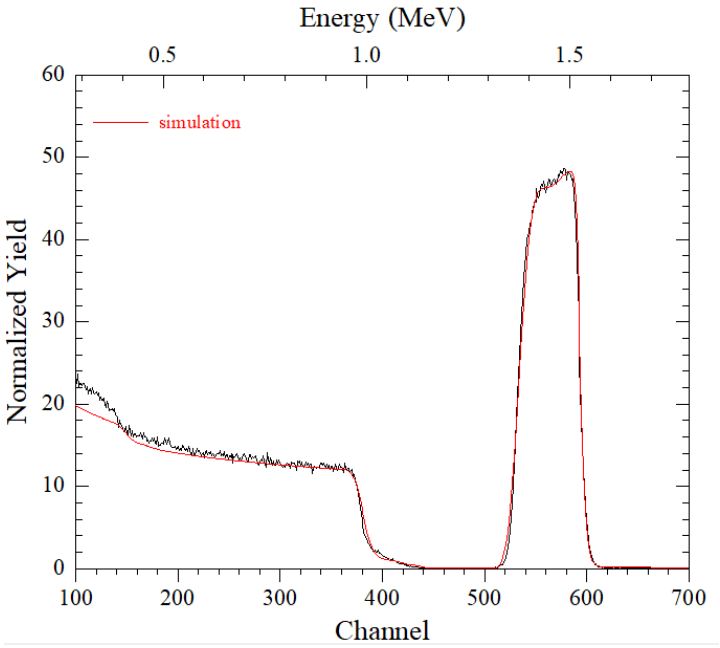

Layer	*Composition (%)*	*Thickness (10^{15})*
1	*Ni 93.63 Si 1.92 C 5.45*	*410 at/ cm^2*
2	*Ni 84.09 Si 4.62 C11.28*	*668 at/ cm^2*
3	*Ni 46.01 Si 14.41 C 39.57*	*180 at/ cm^2*
4	***Si 50.0 C 50.0***	***20000 A***

Fig.23: RBS anlysis for annealed sample at 3.2 J/cm^2

III) ***Phase field and T simulation***

The Tmax is about 1990 K and the phase structures consist mainly of Ni_3Si with minor contributions of $Ni_{31}Si_{12}$ and other less relevant phases, as reported in Fig24-a. The C cluster density observed at interface is about 6 times larger than the corresponding result at 1X2.4 J/cm^2 (Fig.24-b).

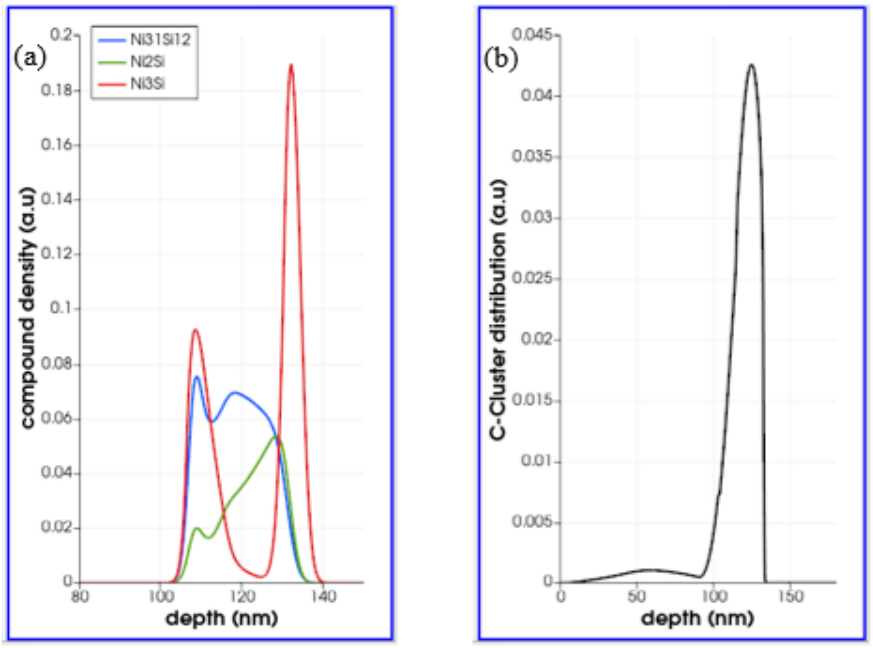

Fig.24: a) simulated phase at interface; b) C cluster density simultion as a function of depth.

The experimental results for the samples at 2X and 3X are expected to be intermediate between 1X and 1X 3.8 J/cm^2, which is the more interesting energy density to be analyzed.

- ***Ni/SiC after 1X 3.8 J/cm²***

I) Morphological and compositional characterization: TEM and EDX analysis

An increment of reacted layer thickness of 67 nm is observed for a 1X 3.8 J/cm² pulse, with big grains and defects (inclusions and twins (Fig.25a)) with a continuous layer of C-Clusters, about 20 nm-thick, that is 10-15 nm away from the 4H-SiC substrate even if some of them are visible up to 30 nm from the interface (Fig.25b)

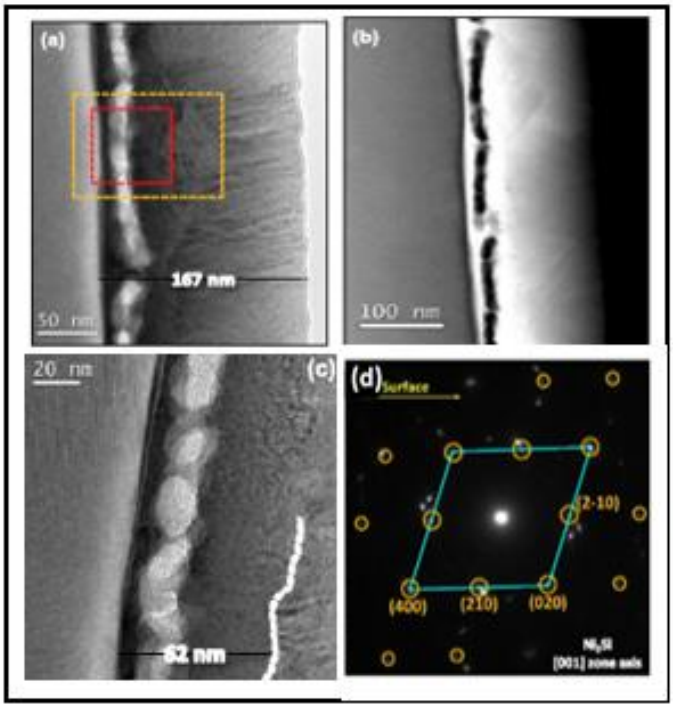

Fig.25: Cross-sectional TEM imagines (a)in bright field and (b) dark field of the Ni/SiC annealed 1 shot at 3.8 J/cm² (c): Magnification of the red panel, (d) SAED image taken at interfacial layer that testifies local silicide reaction in the δ-Ni_2Si phase.

The standard magnification (see Fig25-c), correponding to red panel selected in Fig.25-a, shows a difference in morphology between the interfacial layer with 4H-SiC, 60 nm thick, and residual Ni layer.

From the structural point of view, Fig.25-d shows the typical diffraction patterns of the orthorhombic δ-Ni_2Si phase together with a cubic and hexagonal phase already formed at lower energy density.

The ratio between Ni and Si is about 2:1, i.e. the silicide phase formed in the interfacial layer with 4H-SiC is ascribable to Ni_2Si, an orthorombic phase (see Fig.26).

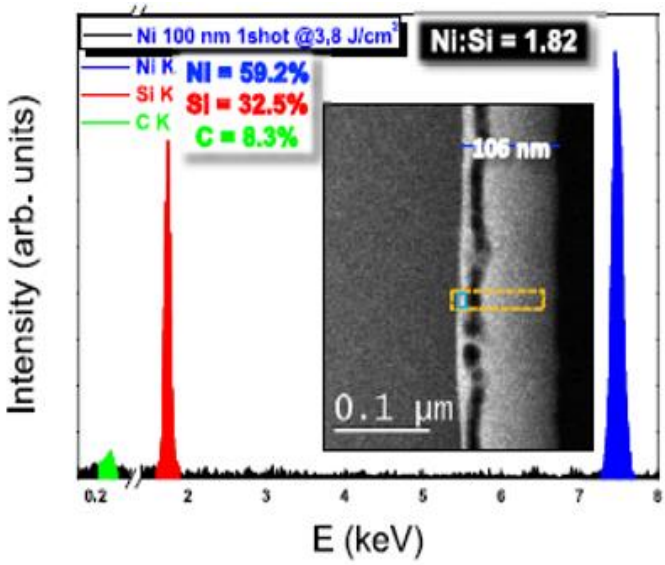

Fig.26: EDX spectrum of the light blue panel in the STEM image in inset.

Mixed composition in the silicide layer is confirmed by EDX analysis and related profile (see Fig. 27).

The silicides layer thickness, 50-60 nm, agree with what observed in the Fig.23-c and in the remnant Ni layer and Si atoms have diffused into the nickel matrix gradually decresing toward the surface (see Fig.28).

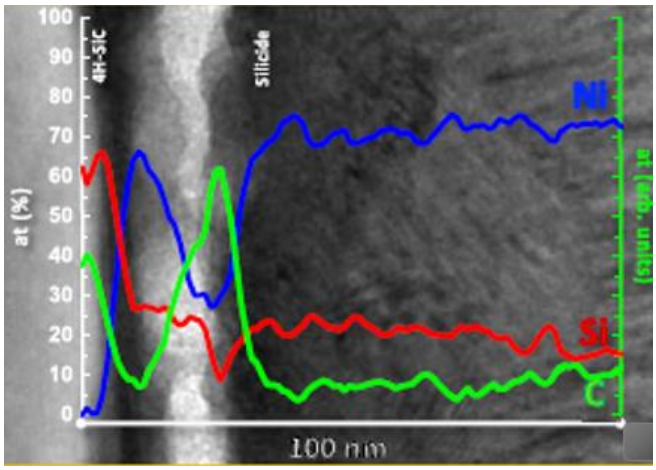

Fig.27: EDX atomin distribution profile in the region inside the yellow panel in Fig.25a and inset of Fig.26.

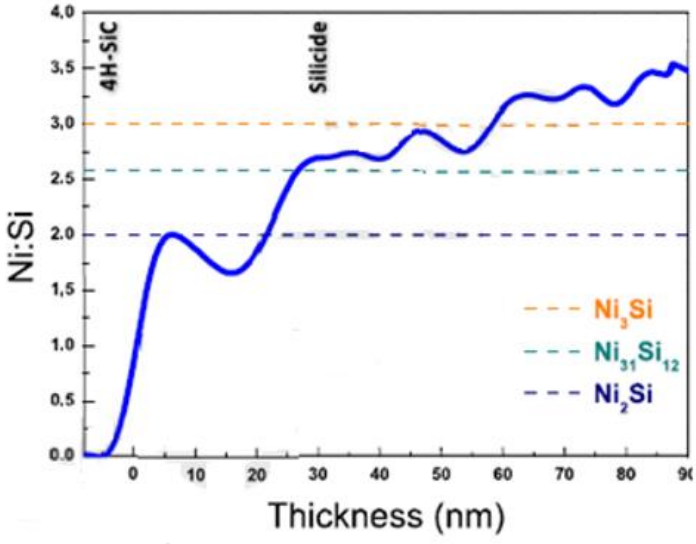

Fig.28: Ni:Si ratio profile from the interface with 4H-SiC through entire layer.

II) Structural characterization: XRD analyses

XRD analyses (blue line) are compared with refererence sample (black line) in Fig.29 and even in this case the residual part of nickel maintains the texturing along the [111].

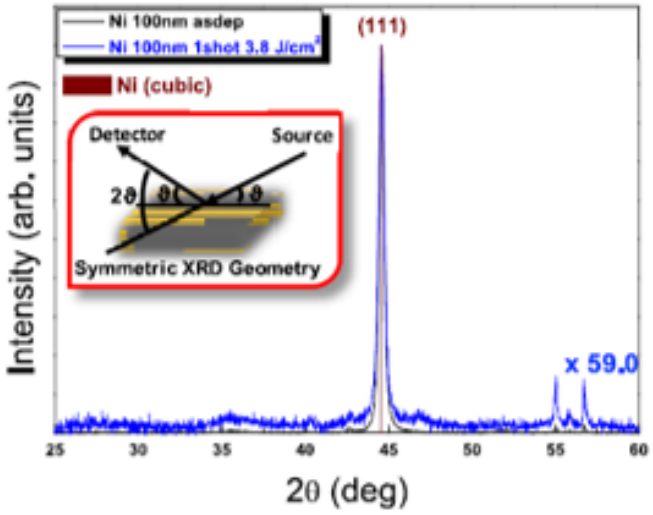

Fig.29: Normalized XRD patterns in symmetric configuration of the Ni sample laser annealed with one pulse at 3.8 J/cm^2 for 160 ns (blue line) and in as deposited condition.

As is shown in Fig.30 the main (111) peak is similar to the reference case but less intense and narrower than the corresponding peaks in the samples treated at lower fluences (see Fig.10 and Fig.20). The FWHM in the reference and in this treated sample are indeed comparable, being $FWHM_{(ref)} = 0.325^{\circ}$ and $FWHM_{(@3.8\ J/cm)} = 0.328^{\circ}$. Instead, the reduction of the FWHM compared to the rest of annealed samples is symptomatic of an improvement of the crystallographic quality in the residual topmost Ni layer.

Moreover, this testifies a progressive increment of the crystallite size, being 25 nm against 24 nm and 21 nm estimated in the samples annealed at 3.2 and 2.4 J/cm^2 respectively. The process of symmetrization of the (111) nickel peak, that is systematic while increasing the fluence (see Figs.10,20 and 30), is ascribed to a progressive consumption of the nickel layer from interfacial reactions that removes a portion of the nickel layer that has been primarily affected by the thermal field and likely by Si diffusion. This explains why, only at the highest fluence, the residual nickel peak (we recall that it is less intense than the one in the reference) approaches the one before annealing although the Ni+Si peak is not any more visible under the (111) Ni peak, a contribution from the alloy can be identified in grazing incidence pattern.

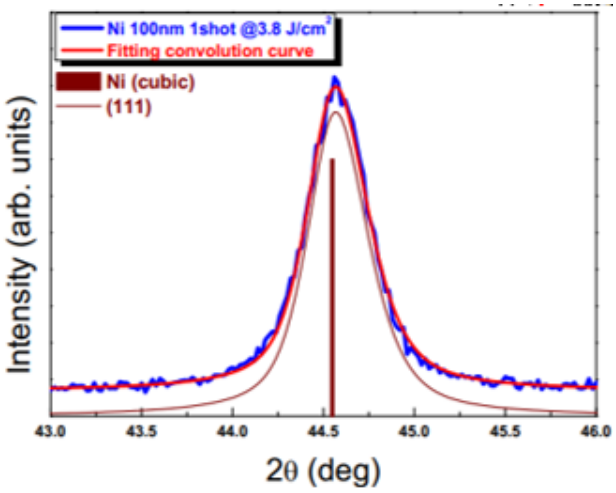

Fig.30: Magnification and deconvolution contributions in the range around the main (111) peak.

The rocking curve on the (111) peak is shown in Fig.31. Differently from the other cases, the peak is left shifted by ~2° and this demonstrates that the preferential growth axis for those grains is twisted. In addition, we found a reduction of the $FWHM_{(rc)}$ (0.566˚) for this sample against the other treated samples and this means that at high fluence the structural order is increased.

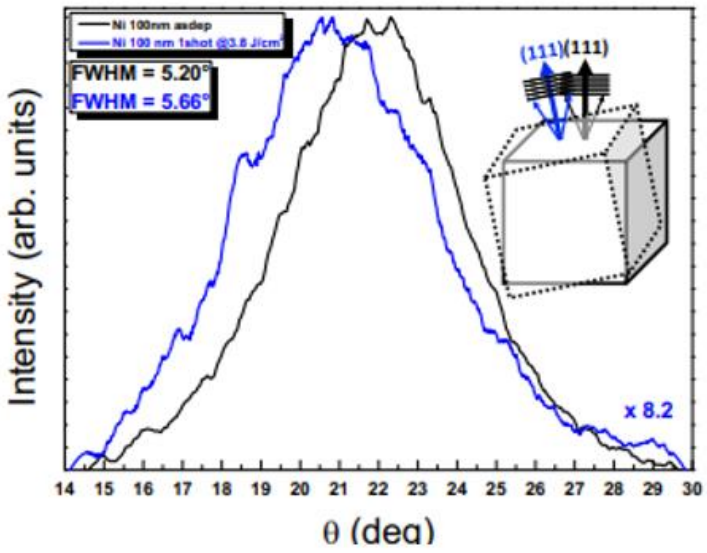

Fig.31: Normalized Rocking curves of the treated vs the untreated sample.

In grazing incidence configuration (see Fig.32) we found an intriguing scenario with several contributions in the pattern that denote the formation of multiple silicide phases. In particular, the 2ϑ range between 41° and 48° can be deconvoluted into different component as shown in Fig.33.

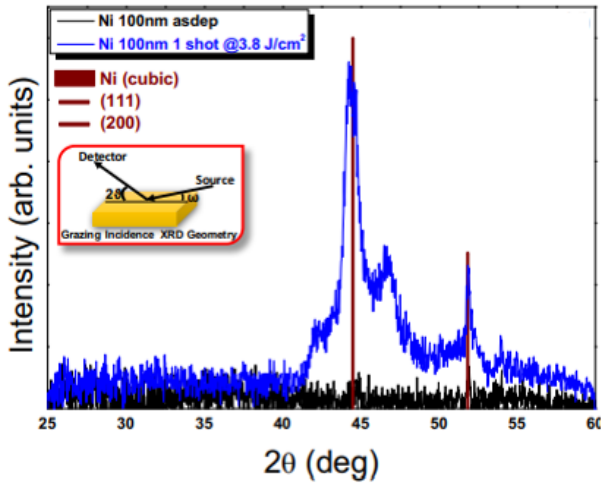

Fig.32: XRD patterns in grazing incidence configuration of the layer annealed a 1X 3.8 J/cm^2 (green line) and in as deposited condition (black line).

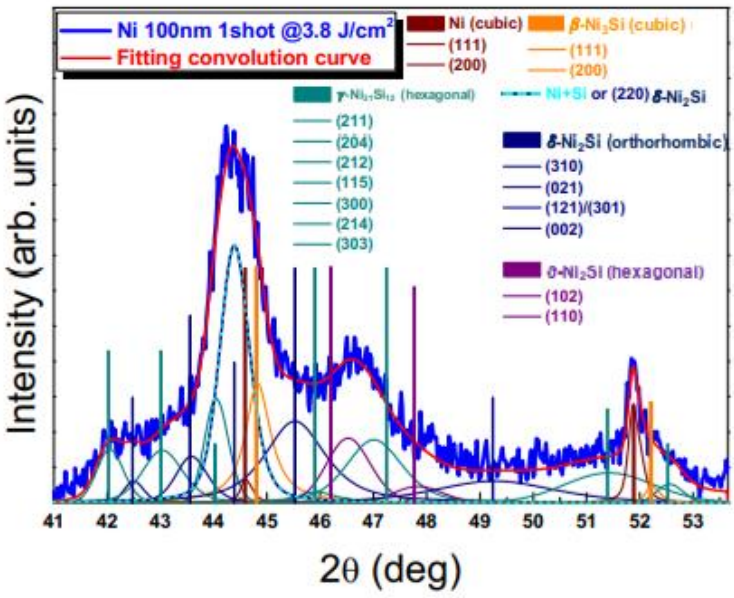

Fig.33: Magnification and deconvoluted contibutions of the treated sample in the range around main (111) and (200) peaks acquired in grazing incidence configuration.

The following information can be extracted:

1)the new evidence on the formation of the orthorhombic Ni_2Si, and of the hexagonal ϑ-Ni_2Si phases with respect to the other analyzed cases;

2) a peak of the Ni+Si alloy can be found at $2\vartheta = 44.365°$, even though this could be equally attributed to slightly strained (by 0.04%) (220) planes of the δ-Ni_2Si phase (both attributions are labelled in Fig.25-d);

3) hexagonal phases such as γ-$Ni_{31}Si_{12}$ are found similarly to what found in the 3.2 J/cm^2 treated samples;

4) the broad peak in the range 46-47.5° has been represented by a double peak deconvolution using two strained (102) ϑ-Ni_2Si and (300) γ-$Ni_{31}Si_{12}$ peaks; it could be equivalently interpreted by unstrained (1,1,12) and (0,3,0) peaks of the hexagonal $Ni_{74}Si_{26}$ (or $Ni_{25}Si_9$) phase, that is given in the literature as a metastable phase observed after fast cooling from a Ni:Si ~ 2.9 melted alloy [4,5];

5) β-Ni_3Si contributions are also found. Another main feature in the diffraction pattern is found in the range 2ϑ ~ 48-53.5˚ in which main contributors are γ-$Ni_{31}Si_{12}$, δ-Ni_2Si, pure Ni and β-Ni_3Si.

Most importantly, the δ-Ni_2Si phase can be localized at the interface with the 4H-SiC substrate on the basis of TEM results such as the one shown in Fig. 25c/d and also in agreement with the Ni/Si chemical profile in Fig.28.

III) Compositional characterization: RBS analysis

The RBS analysis for treated sample with one pulse at 3.8 J/cm^2 is reported in Fig.34 and detects an interfacial layer with a Ni:Si ratio of 2.5.

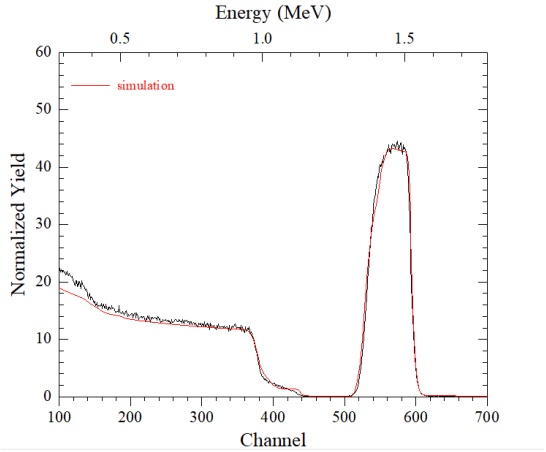

Layer	*Composition (%)*	*Thickness (10^{15})*
1	*Ni 80.4 Si 8.70 C 10.9*	*930 at/ cm^2*
2	*Ni 47.7 Si 19.8 C 33.2*	*250 at/ cm^2*
3	***Si 50.0 C 50.0***	***20000 A***

Fig.34: RBS spectrum and simulation for Ni/SiC after 1X3.8 J/cm^2.

IV) ***Phase field and T simulation***

Also for this sample there is a temperature (2200 K) and C cluster density increase, as reported in Fig.35a-b. Moreover, the C cluster density is broder than the previous case.

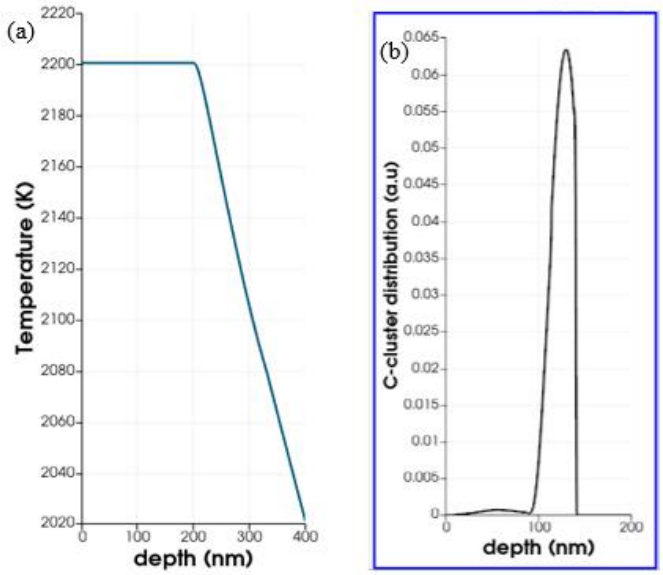

Fig.35: a) T simulation as a function of depth b) C-cluster density simulation of depth.

The different simulated phases are given in Fig.36, which shows a growth of silicides layer and slight increase of the compound densities in comparison with the previous cases. In particular, the Ni_3Si phase is still dominant with respect to the other ones.

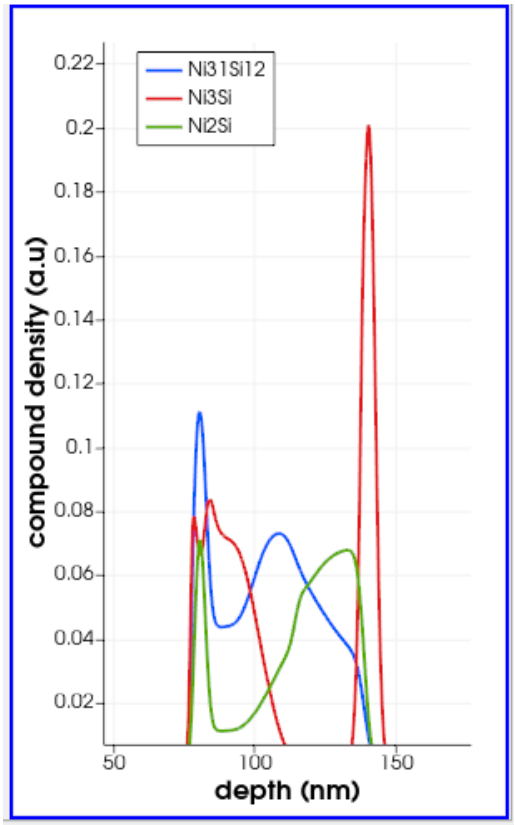

Fig.36: Simulated phase at interface

- ***Ni/SiC after 2X 3.8 J/cm²***

I) Compositional characterization: RBS analysis

RBS data for annealed sample with double pulse at 3.8 J/cm^2 are reported in Fig. 37 and detect an interfacial layer where the ratio between Ni:Si is about 2.

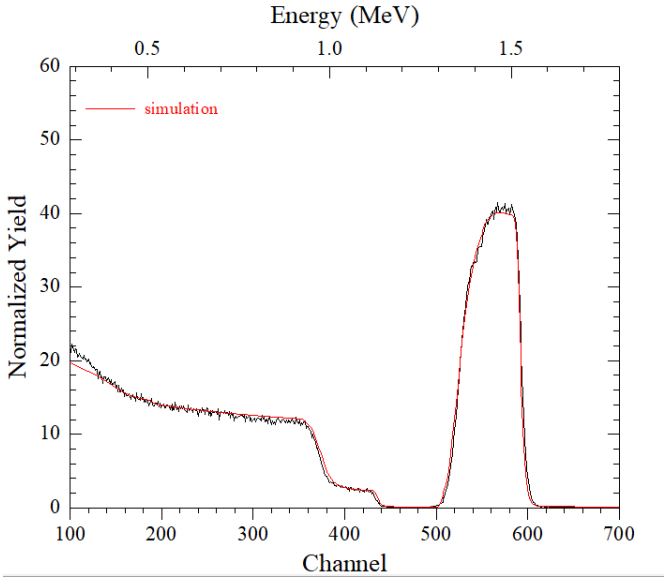

Layer	*Composition (%)*	*Thickness (10^{15})*
1	*Ni 69.6 Si 15.2 C 15.2*	*1000 at/ cm²*
2	*Ni 48.3 Si 17.2 C 34.5*	*430 at/ cm²*
3	*Ni 40.6 Si 18.7 C 40.6*	*420 at/cm²*
4	***Si 50.0 C 50.0***	***20000 A***

Fig.37: RBS spectrum and simulation (red line) for Ni/SiC after 2X3.8 J/cm²

II) ***Phase field and T simulation***

The corresponding phase field simulations are in agreement with previous value of Ni:Si ≈2 (see Fig. 38a), while the C-cluster distribution becomes broader (Fig.38b). The maximum temperature turns out to be 2385 K (see Fig.39).

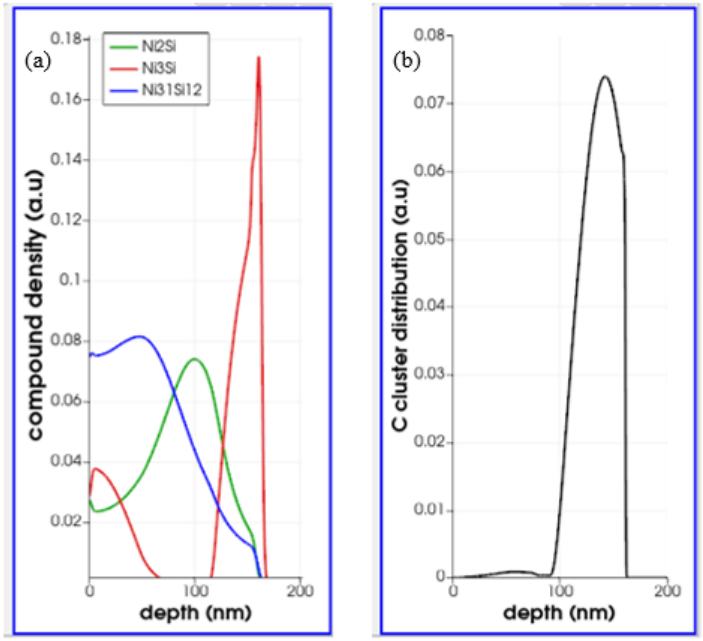

Fig.38: Phase simulation at interface (a) and C cluster distribution (b).

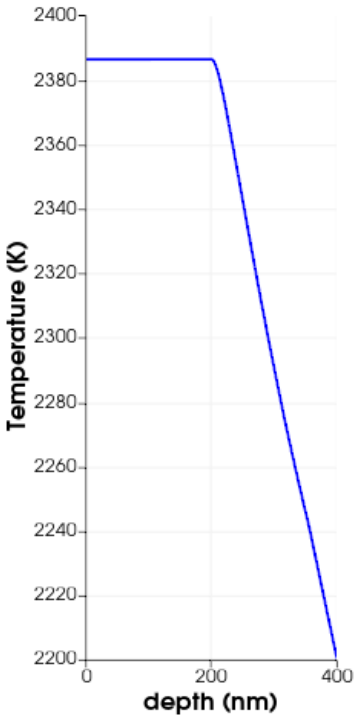

Fig.39: T simulation as a function of depth.

- ***Ni/SiC after 3X 3.8 J/cm^2***

I) Compositional characterization: RBS analysis

RBS data and the numerical simulation detect a Ni-riched interfacial with a stoichiometry ≈ Ni_2Si, (see Fig.40 and related table).

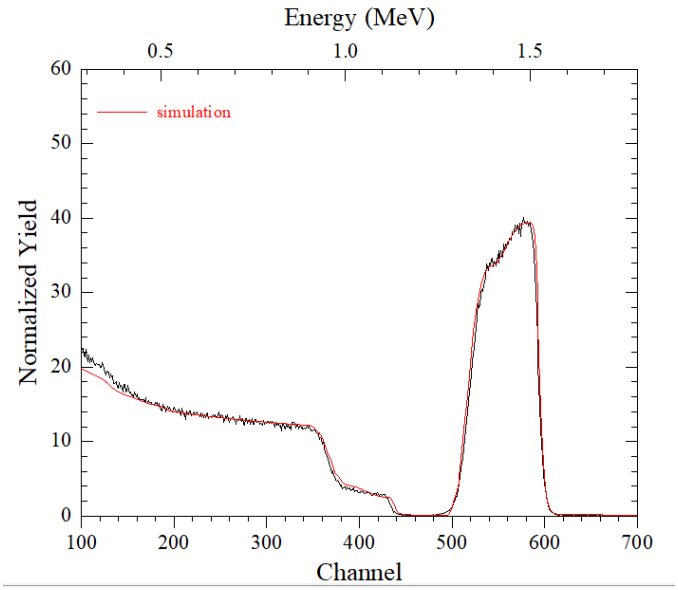

Layer	*Composition (%)*	*Thickness (10^{15})*
1	*Ni 68.6 Si 15.9 C 15.4*	*670 at/ cm^2*
2	*Ni 61.8 Si 19.4 C 19.4*	*180 at/ cm^2*
3	*Ni 50.5 Si 22.6 C 26.9*	*980 at/cm^2*
4	***Si 50.0 C 50.0***	***20000 A***

Fig.40: RBS spectrum and simulation (red line) for treated sample with triple pulses at 3.8J/cm^2.

RBS simulation compared with previous case shows the presence of larger layer of Ni_2Si.

II) *Phase field and T simulation*

The Tmax is about 2403 K (see Fig.41) and the phase structures consist of Ni_2Si layer interfacial that it is expands to the surface with other Ni-riched phases as reported in Fig (see Fig.42a). The C cluster density observed at interface is larger than the corresponding result at 1X and 2X 3.8 J/cm^2 (Fig.42b).

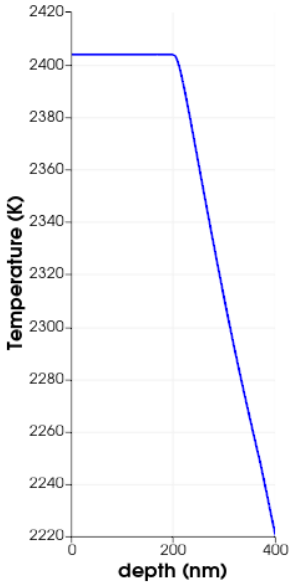

Fig. 41: T simulation as function of depth.

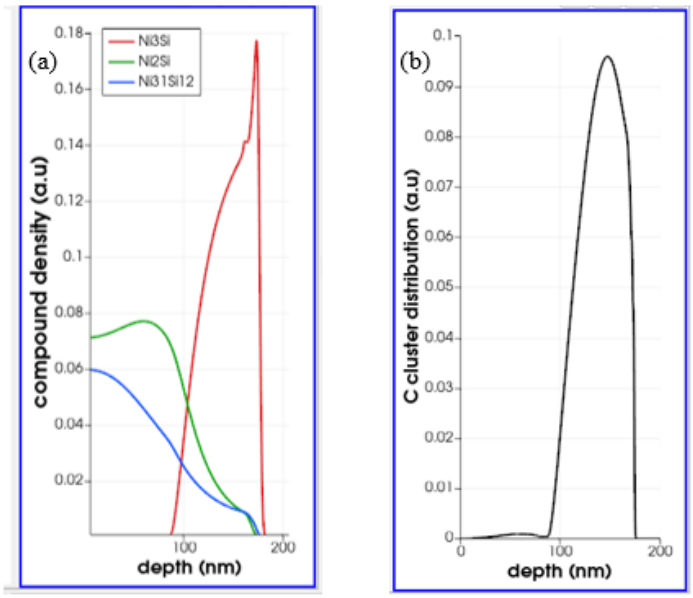

Fig.42: Phase simulation at interface (a) and C cluster distribution (b).

The phase field simulation (see Fig.42a) compared with the previous samples (see Fig.36-38) suggests that the Ni_2Si phase (green line) diffuses toward the surface as the energy increases.

4.2.2 Electrical characterization: sheet resistance measurements

Electrical measurements on dedicated test patterns have been performed on the back side of heavily doped substrate. In particular, sheet resistance, Rs, of the as deposited Ni layer and of laser annealed samples as a function of the energy density has been measured by a Four Point Probe (FPP). This parameter provides a first indication on the layer conductivity that is related to a combination of stoichiometry, morphology and thickness of the reacted contact. Indeed, the lack of a vertical isolation of the TLM patterns, together with the low sheet resistance of the substrate, did not allow a better quantitative determination of the value of the specific contact resistance.

Fig. 43 shows the R_s values normalized to the initial value R_0 (as deposited) for a starting Ni thickness of 100 nm and for different laser settings.

A sharp reduction of Rs is observed for energy density larger than some specific threshold which depends on the total deposited energy.

Indeed, the content of Ni_2Si and its redistribution down to the surface observed by phase simulation and RBS measurements could be considered crucial ingredient to achieve low resistivity in Ni/SiC devices This phase recrystallization requires the fairly large energy density with a threshold that depends on the number of pulses.

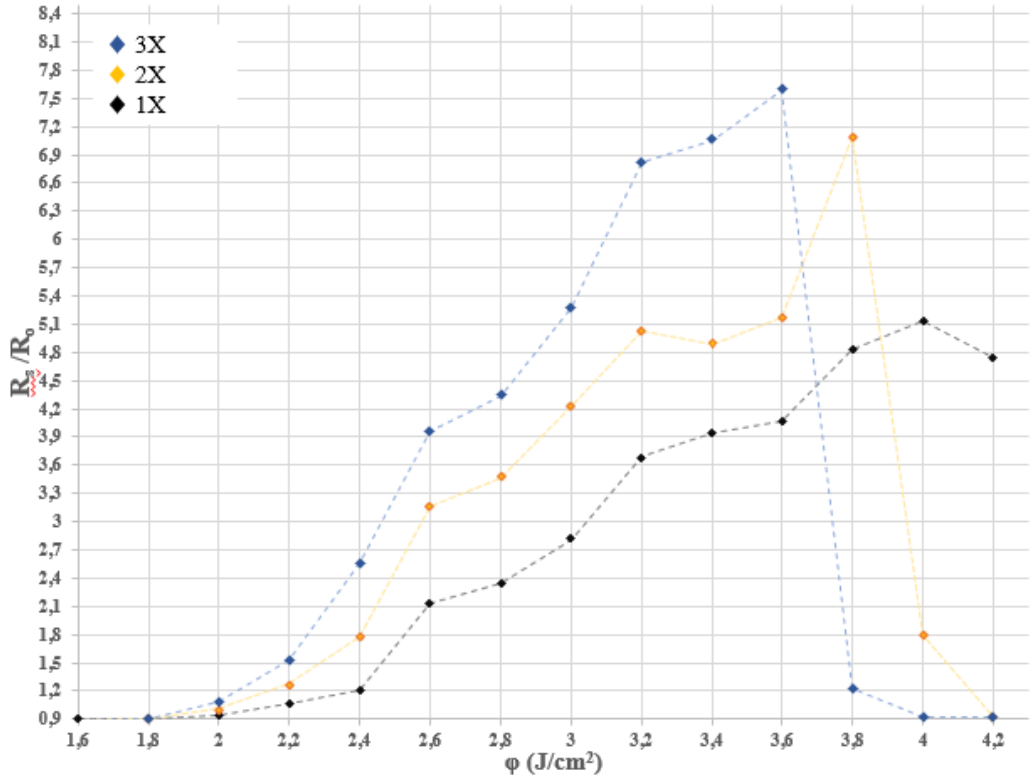

Fig.43: Sheet resistance R_s normalized to the initial value R_0 (as deposited) by Four Point Probe (FPP) measurements as a function of energy density (E.D.)

4.2.3 Discussion

The morphological analysis of Ni/SiC laser annealed samples suggests an almost linear increase of the thickness of the reacted layer, wich starting from deposited 100 nm, turns out to be 122 nm for 1X2.4 J/cm^2, 148 nm for 1X3.2 J/cm^2 and 167 nm for 1X3.8 J/cm^2. Moreover, the simulation of the typical variation of the C cluster distribution with the single pulse fluence, reported in Fig .44 (green line: 3.8 J/cm^2, red line: 3.2 J/cm^2 and orange line:2.4 J/cm^2), shows the dependence on the energy of the C atoms content and localization.

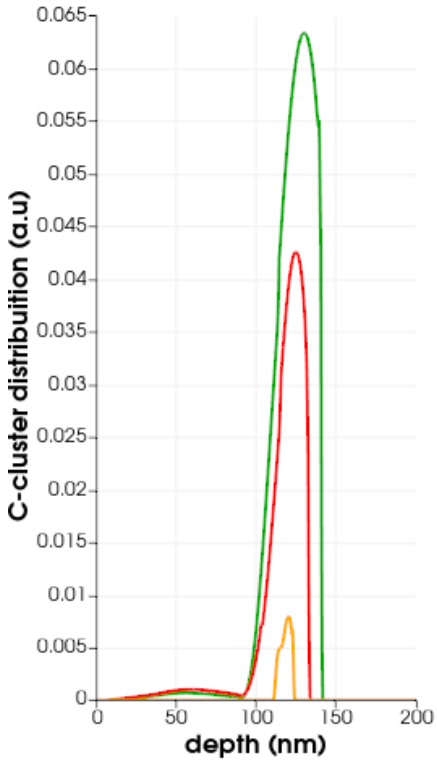

Fig.44: Variation of C-clusters distribution with the single pulse fluence for different values of energy density.

Its dependence on the number of pulses at fixed energy density is given in Fig.45 (1X-2X-3X at 3.8 J/cm^2). The C-cluster distribution becomes broader with increasing the shot number and the energy density, and simultaneously their intensity increases.

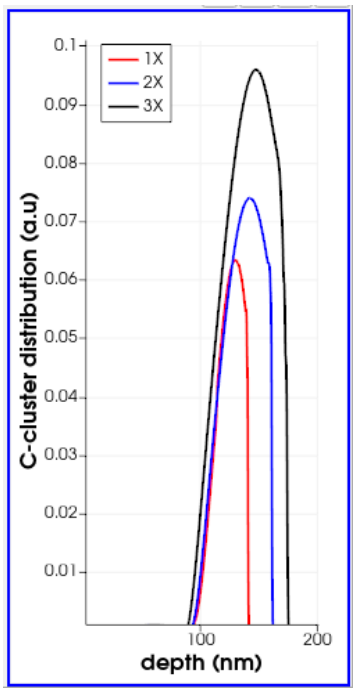

Fig.45: C-cluster distribution as a function of number of pulses at fixed E.D (3.8 J/cm^2)

The simulated temperature for single pulse is depicted in Fig.46 versus the energy density and it shows an almost linear trend. This temperature also increases with increasing the shot number at fixed energy (Fig.47).

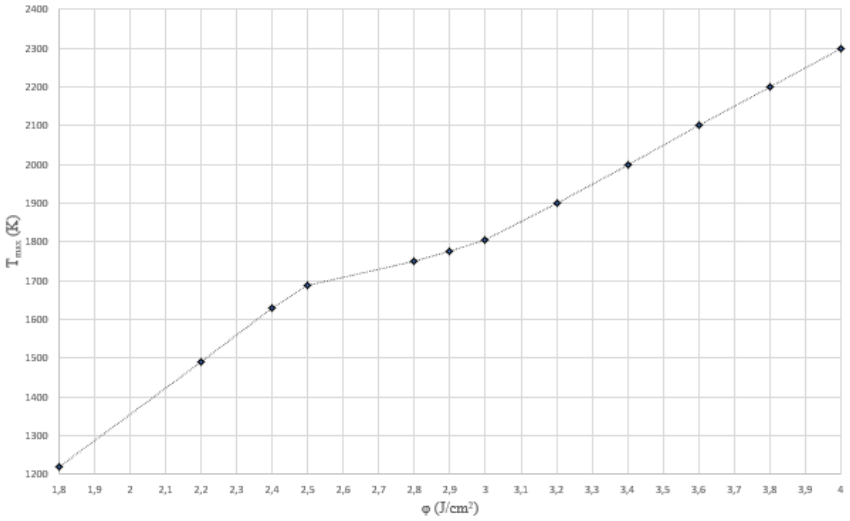

Fig.46: Simulated temperature for single pulse versus energy density.

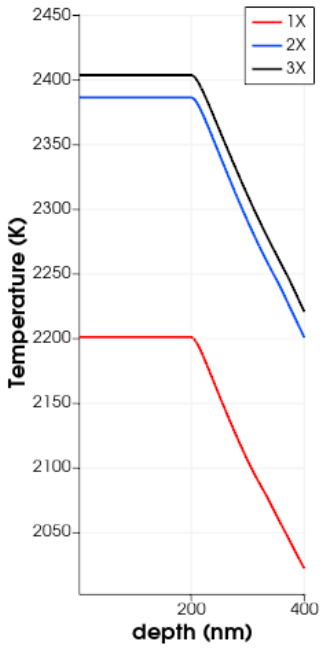

Fig.47: Simulated temperature behaviour as a function of different pulses at fixed E.D (3.8 J/cm^2).

The previous sections give a detailed description of the phase formation during LA with various energies and, therefore, with various temperatures, by applying different techniques and simulations.

The results are summarized in Table 1, with a qualitative agreement between EDX and RBS methods (the latter technique is less accurate).

Energy density (J/cm^2)	EDX Ni:Si	RBS Ni:Si(data/simulation)	XRD	Phase simulation
1X2.4	3	3.47	Ni_3Si; Ni+Si	Ni_3Si; Ni_2Si
1X3.2	2.55	3.28	Ni_3Si; $Ni_{31}Si_{12}$;others	Ni_3Si; Ni_2Si;$Ni_{31}Si_{12}$
1X3.8	1.82	2.50	Ni_3Si; Ni_2Si; $Ni_{31}Si_{12}$;Ni+Si	Ni_3Si; Ni_2Si;$Ni_{31}Si_{12}$
2X3.8	Future work	2.0	Future work	Ni_3Si; Ni_2Si;$Ni_{31}Si_{12}$
3X3.8	Future work	2.0	Future work	Ni_3Si; Ni_2Si;$Ni_{31}Si_{12}$

Table 1: Description of the phase formation after LA process.

The results at 3X3.8 J/cm^2, correspond to the conductive phases, dominated by Ni_2Si, as seen in the R_s/R_o ratio in Fig.43.

Indeed, considering the ohmic contact formation, Fig.43 clearly shows a transition to more conductive phases with a sharp behaviour near a critical enegy threshold, which depends on the number of pulse. In fact, for 3X3.8J/cm^2 the transition occurs at 3.8J/cm^2, whereas it is observed at 4.0 J/cm^2 for 2X3.8 J/cm^2 and expected at an energy larger than 4.2 J/cm^2 for the single pulse.

This conclusion is further confirmed by analizyng the Ni_2Si content in 1X-2X-3X 3.8 J/cm^2 given in Fig.48, where a Ni_2Si layer is redistribute up to to the surface by increasing of number of pulses.

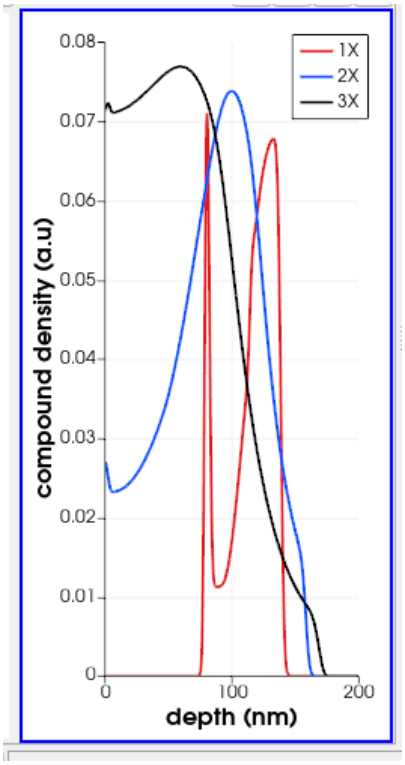

Fig.48: Ni_2Si distribution as a function of number of pulses at fixed E.D (3.8 J/cm^2).

The previous data and simulations on the C-atoms content are useful since an important role in the ohmic contact formation of carbon localization has been propose (see [35]

Chapter2). C-clusters are generally localized on the Ni-silicide/SiC interface, inside silicide layer or on free silicide surface [6].

The results indicate the C-clusters formation at distance larger than 7 nm from the substrate at 1X 2.4 J/cm^2, which reduces at 1X3.2 J/cm^2 but wit larger size C-Clusters. At energy pulse of 1X3.8 J/cm^2 the formation of a C-layer at 10-15 nm from substrate is observed.

Moreover, the simulations suggest a C-Cluster density of $\approx$ 0.008 (a.u.) formed at 1X2.4 J/cm^2 which increases to 0.043 for 1X3.2 J/cm^2 and to 0.065 for 1X3.8 J/cm^2. Therefore, a phase with a growing number of C-Cluster/layer is expected closer to the substrate at larger energy.

A different proposal, still related to C-atoms role, is the structural changes of the SiC substrate in close vicinity of silicide/SiC interface [7], due to the creation of vacancies, which lower the Schottky barrier [8].

The diffusion of carbon atoms towards free silicide surface is the suspected mechanism for the creation of these vacancies [8,9]. However, this proposal can not be completly accepted due to the result by DLTS on the concentration of carbon vacancies for 950 °C annealed contacts. (see [36] Chap. 2].

In general, the contribution of carbon to ohmic contact creation may be very complex although the detection of additional carbon cluster/ layer close to the interface suggests a possible catalytic role of this element.

On the other hand, the phase transition is the dynamical aspect difficult to neglect. The sharp transition of Rs in Fig.43 suggests a conductive phase, which should be related to larger uniform thickness Ni_2Si. Nevertheless, future investigations are needed to accurately determine the nature of the conducting phase.

References

[1] P. Badalà, G. Faro, C. Marcellino, G. Pellegrino, A. Santangelo, A. Alberti, Structural characterization of in situ silicided contacts textured on p type [001] silicon, Phys.Status Solidi C 11 (2014) 160.

[2] J.P. Gambino, E.G. Colgan, Silicides and ohmic contacts, Mater. Chem. Phys. 52 (1998) 99.

[3] A. Alberti, C. Bongiorno, E. Rimini, M.G. Grimaldi, Critical nickel thickness to form silicide transrotational structures on [001] silicon, Appl. Phys. Lett. 89 (2006).

[4] P. Badalà, S. Rascunà, B. Cafra, A. Bassi, E. Smecca, M. Zimbone, C. Bongiorno, C. Calabretta, F. La Via, F. Roccaforte, M. Saggio, G. Franco, A. Messina, A. La Magna, A. Alberti. Ni/4H-SiC interaction and silicide formation under excimer laser annealing for ohmic contact. Materialia 9 (2020) 100528.

[5] L. Cao, R.F. Cochrane, A.M. Mullis, Microstructural Evolution and Phase Formation in Rapidly Solidifies Ni-25.3. At. Pct Si Alloy, Metall. And Mater.Trans. A 46A (2015) 4705.

[6] A. V. Kuchuk, P. Borowicz, M. Wzorek, M. Borysiewicz, R. Ratajczak, K. Golaszewska, E. Kaminska, V. Kladko and A. Piotrowska. Ni-Based Ohmic Contacts to *n*-Type 4H-SiC: The Formation Mechanism and Thermal Stability. Hindawi Publishing CorporationAdvances in Condensed Matter Physics Volume 2016, Article ID 9273702, 26 pages.

[7] S. Cichoˇn, P. Mach´aˇc, B. Barda, and M. Kudrnov´a, “Si ohmic contacts on N-type SiC studied by XPS,” Microelectronic Engineering, vol. 106, pp. 132–138, 2013.

[8] F. A. Mohammad, Y. Cao, and L. M. Porter, “Ohmic contacts to silicon carbide determined by changes in the surface,” Applied Physics Letters, vol. 87, no. 16, Article ID 161908, pp. 1–3, 2005.

[9] S. Y. Man, K. H. Kim, J. K. Kimet al., “Ohmic contact formation mechanism of Ni on n-type 4H–SiC,” Applied Physics Letters, vol. 79, no. 12, pp. 1816–1818, 2001.

[10] P. Badalà, E. Smecca, S. Rascunà, C. Bongiorno, E. Carria, A. Bassi, G. Bellocchi, S. Castorina, C. Tringali, A. La Magna and A. Alberti, Structural and electrical characterization of Ni-based ohmic contacts on 4H-SiC formed by solid-state laser annealing, Materials Science Forum, submitted.

Conclusions

Laser annealing process for ohmic contact formation on 4H-SiC has attracted increasing attention in the last years, because it enables the fabrication of SiC power devices on very thin substrates. Thinning wafers, indeed, can bring great improvement in terms of power dissipation, but it is not compatible with Rapid Thermal Annealing (RTA) process commonly used to form ohmic contact on SiC, due to the high temperature required.

Moreover, the realization of ohmic contacts on the wafers back side requires the Laser Annealing (LA) due to the presence of defined devices on the front of the wafer.

In this thesis, different characteristics of the LA processes have been studied (by changing the number of shots and the laser energy density) in order to evaluate the conditions to obtain the best performance of the device, i.e. the lowest values of sheet resistance.

According to the XRD-TEM-EDX-RBS and the simulation results, the initial formation of Ni_2Si for Ni / SiC after 1X3.8 J / cm^2 and its subsequent enrichment also on the surface for Ni / SiC after 3X3.8 J / cm^2 could lead to a decrease in Rs, as found in Fig. 43.

Furthermore, it has been found that at high energies and number of hits the C-clusters increase and enrich the interface more and more.

The results obtained in this research confirms that the origin of ohmic contact is still an open problem, probably related to a combination of different mechanisms (C-atoms distribution and conductive) synergistically operating to reduce the Scottky barrier.

The obtained results call for further XRD, TEM and EDX characterization of 2X and 3X at 3.8 J/cm^2 in order to confirm the RBS measurements and Phase simulation results and also researches will be aimed at direct deposit Ni_xSi_y on the back -side of SiC substrate, to reduce the silicon consumption of SiC during the silicides reaction.

More generally, alternatives in term of pulse duration and wavelength could offer additional process option and a wider process window (see [10]).